Biomedicine & Pharmacotherapy 203 (2026) 119907

Contents lists available at ScienceDirect

Biomedicine & Pharmacotherapy

journal homepage: www.elsevier.com/locate/biopha

Review

Albumin surface and interface engineering of non-albumin nanoparticles in cancer nanomedicine: A critical review

Hanan Mohammad [a], Maher Darwish [b,c], Gábor Katona [a,*], Ildikó Csóka [a]

[a] Institute of Pharmaceutical Technology and Regulatory Affairs, Faculty of Pharmacy, University of Szeged, Szeged H-6720, Hungary
[b] Department of Optics and Quantum Electronics, University of Szeged, Dóm sq. 9, Szeged 6720, Hungary
[c] Department of Pharmaceutical Chemistry and Drug Control, Faculty of Pharmacy, Wadi International University, Homs, Syria

ARTICLE INFO

Keywords:
Albumin surface engineering
Albumin-coated nanoparticles
Cancer nanomedicine
Controlled drug release
Protein corona
Corona proteomics

ABSTRACT

Engineered albumin interfaces can modify the biological identity and performance of non-albumin nanoparticles in cancer nanomedicine, but their independent contribution is often obscured by multicomponent designs. This critical review evaluates studies in which albumin or an albumin-derived construct was deliberately positioned at the outer interface of a non-albumin nanoparticle or drug nanocrystal before biological exposure. Architectures included adsorbed layers, covalent or crosslinked coatings, albumin-stabilized nanocrystal interfaces, and hybrid or modified constructs. Across 35 primary studies, albumin served mainly as a stabilizing, cargo-binding, release-modulating, ligand-bearing, or biologically active interfacial component. Matched controls supported selected albumin-associated changes in colloidal stability, cellular interaction, tumor drug delivery, macrophage uptake, and secondary-corona composition. By contrast, imaging, photothermal and radiation responses, pharmacokinetics, biodistribution, and antitumor efficacy often depended on the nanoparticle core, payload, targeting ligand, other surface components, or applied energy and therefore generally represent formulation-level outcomes unless albumin was specifically isolated. Secondary-corona studies suggest that engineered albumin interfaces may reshape corona composition rather than suppress protein adsorption, but the biological consequences remain incompletely resolved. The persistence and conformational accessibility of manufactured albumin interfaces during circulation are also poorly defined, and proposed receptor-mediated mechanisms rarely have direct support. Corona-proteomic findings remain hypothesis-generating and have not established clinically validated cancer detection or diagnostic performance. Future translation requires matched albumin-free and protein-replacement controls, independent in vivo tracking of nanoparticle cores and albumin interfaces, standardized secondary-corona characterization, pharmacokinetic and safety evaluation, and validation of promising bovine serum albumin (BSA)-based systems using clinically relevant human serum albumin (HSA) interfaces.

1. Background

The clinical translation of cancer nanomedicines remains constrained by a fundamental biological event: the formation of a protein corona. After exposure to blood or other biological fluids, nanoparticles rapidly acquire a dynamic layer of adsorbed proteins and biomolecules that can overwrite their synthetic surface identity and influence their biological fate [1,2]. This corona affects complement activation, macrophage recognition, biodistribution, cellular uptake pathways, and therapeutic performance. Consequently, discrepancies between predicted nanoparticle behavior in vitro and observed behavior in vivo are often linked to the uncontrolled evolution of this biological interface [3]. In the following sections, we first define the key terminology and structural boundaries used throughout this review and then outline the scope, study-selection criteria, and evidence framework applied to the reviewed literature.

1.1. Terminology, structural boundaries, and in vivo corona formation

Throughout this review, protein corona, preformed albumin corona, albumin-coated nanoparticle, fixed albumin surface layer, modified albumin interface, and albumin nanoparticle refer to structurally and

* Correspondence to: Institute of Pharmaceutical Technology and Regulatory Affairs, Faculty of Pharmacy, University of Szeged, Eötvös Str. 6, Szeged H-6720, Hungary.
E-mail address: katona.gabor@szte.hu (G. Katona).

https://doi.org/10.1016/j.biopha.2026.119907
Received 9 June 2026; Received in revised form 19 August 2026; Accepted 1 September 2026
Available online 3 September 2026

mechanistically distinct systems. A protein corona forms spontaneously when a nanoparticle encounters blood, plasma, serum, or another biological fluid. Its composition evolves through adsorption, desorption, displacement, protein exchange, and protein-protein interactions. More persistent and rapidly exchanging components are commonly described as hard and soft coronas, respectively, although these represent operational points along a continuum of affinities and residence times [4]. Corona composition depends on nanoparticle size, shape, charge, hydrophobicity, curvature, and surface chemistry, together with protein abundance and affinity, exposure time, fluid composition, hydrodynamic conditions, administration route, disease state, and tissue environment. It may therefore change during circulation and passage through biological compartments. Consequently, coronas generated by static serum or plasma incubation should not automatically be assumed to reproduce the composition, exchange behavior, or biological effects of coronas formed in vivo [5].

An albumin-coated nanoparticle is deliberately manufactured by positioning albumin at the surface of a pre-existing non-albumin nanoparticle or drug nanocrystal before biological exposure. The term "preformed albumin corona" is reserved here for a predominantly noncovalent, adsorption-derived albumin-rich layer. Covalently immobilized or crosslinked albumin is classified as a fixed albumin surface layer, whereas biomineralized, nanocluster-bearing, ligand-functionalized, denatured, cationized, polyethylene glycol (PEG)ylated, or otherwise altered albumin constructs are classified as hybrid or modified interfaces. These synthetically controlled interfaces differ from spontaneously acquired coronas in their architecture, exchange potential, and intended functions. Following biological exposure, a preformed, fixed, or modified albumin interface may acquire an additional mixed biomolecular layer. The prebound albumin may persist, reorganize, undergo partial displacement, exchange with endogenous proteins, or become masked by subsequently adsorbed proteins. The terms "acquired corona" and "secondary corona" refer here to this post-exposure layer. The manufactured interface and the subsequently acquired corona therefore represent sequential and interacting levels of nanoparticle identity, not interchangeable concepts.

At nanoparticle interfaces, albumin may contribute to colloidal stabilization, reduced opsonin-dominated recognition, drug loading, release modulation, and tumor-associated transport [6–8]. A preformed albumin layer has also been associated with reduced nonspecific protein adsorption and complement activation, prolonged circulation, and lower nanoparticle-associated toxicity in an experimental model [9]. These effects remain formulation-dependent and cannot be assumed for every albumin-containing interface. Fig. 1 summarizes these structural boundaries and their potential evolution after biological exposure.

1.2. Review scope and evidence framework

Although albumin nanoparticles and the broader protein-corona phenomenon have been extensively reviewed [7,10,11], less attention has been directed toward systems in which albumin is deliberately engineered at the surface of a pre-existing nanoparticle and toward the specific contribution of this interface to colloidal behavior, biological identity, cellular interactions, targeting, controlled release, imaging, therapy, and emerging diagnostic concepts. This review therefore focuses on albumin as an engineered interfacial component positioned on a discrete non-albumin nanoparticle or drug-nanocrystal core before biological exposure (Fig. 1). The analysis is restricted to human serum albumin (HSA) and bovine serum albumin (BSA), the two albumin sources predominantly represented in the eligible literature and sharing substantial structural similarity. Other protein sources, including mouse serum albumin and non-serum albumins, were excluded. Although some experimental studies report acceptable biocompatibility or limited immunological responses for BSA-containing formulations under the specific conditions investigated, these findings should not be interpreted as evidence of general immunological equivalence between BSA and

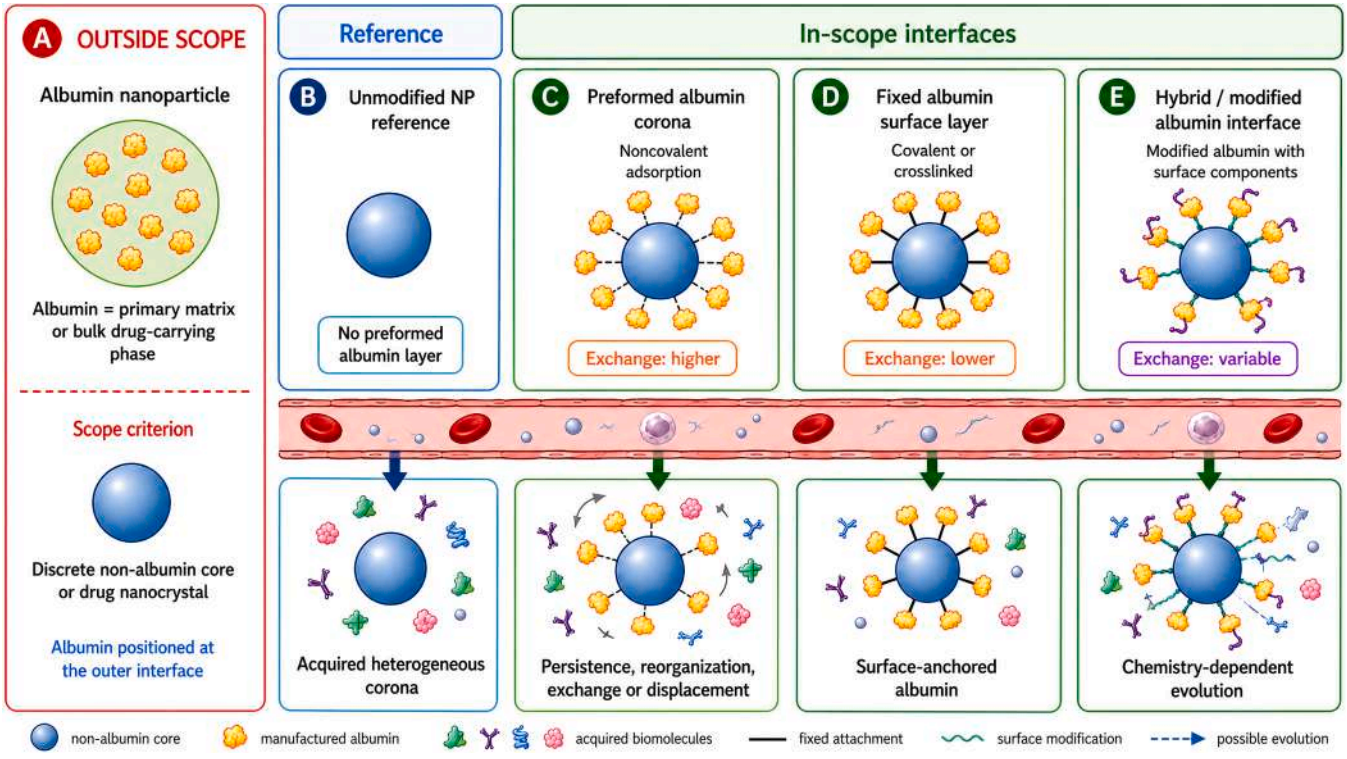

Fig. 1. Structural classification and potential biological evolution of albumin-containing nanoparticle systems. Albumin nanoparticles, in which albumin forms the primary matrix (A), are outside the scope of this review. The figure distinguishes unmodified nanoparticles that may acquire a spontaneous corona (B) from included systems with preformed, noncovalently adsorbed albumin coronas (C), fixed covalent or crosslinked albumin layers (D), and hybrid or modified interfaces (E). Engineered albumin interfaces may undergo exchange, displacement, masking, or secondary-corona formation after biological exposure.

HSA. BSA remains predominantly a preclinical material in this context, and no Food and Drug Administration (FDA)-approved BSA-based cancer nanomedicine was identified at the time of this review. Because BSA is xenogeneic to humans and differs from HSA in sequence, ligand-binding behavior, conformational responses, and species-dependent biological interactions, findings obtained with BSA-engineered interfaces should not be directly extrapolated to HSA-based clinical formulations.

Candidate studies published from January 2020 through August 2026 were identified through targeted searches of PubMed, Scopus, Web of Science, and Google Scholar, supplemented by reference tracking. Artificial intelligence (AI)-assisted scholarly research tools, including Scite, Consensus, Elicit, and SciSpace, were used as supplementary aids for semantic literature discovery, citation-context checking, and cross-checking of potentially relevant records. These tools were not used to make autonomous eligibility decisions. Search terms covered engineered albumin interfaces in cancer nanomedicine, including surface functionalization, imaging, theranostics, controlled drug delivery, targeting, biological identity, barrier transport, and corona proteomics. Thirty-five primary studies met the predefined scope, requiring deliberate placement of HSA, BSA, or their modified constructs at the outer interface of a discrete non-albumin nanoparticle or drug nanocrystal before biological exposure, together with relevant physicochemical or biological evidence. All records, citations, and study details identified or summarized through AI-assisted tools were manually verified against the original full-text publications, and final study selection and scientific interpretation were performed by the authors. The included studies were organized into five thematic areas: diagnostic imaging, integrated theranostic platforms, biological identity and stealth, cancer-specific controlled-release strategies, and secondary-corona proteomics with potential future diagnostic relevance. An overview of study-level evidence coverage across physicochemical characterization, biological testing, corona proteomics, imaging or biodistribution, pharmacokinetics, and in vivo efficacy is provided in Table 1. Effects were attributed specifically to the deliberately engineered albumin interface only when supported by appropriate matched comparisons, particularly with albumin-free formulations. In the absence of such controls, biological, imaging, or therapeutic outcomes were conservatively attributed to the complete multicomponent formulation rather than to albumin alone. This evidence-attribution principle was applied consistently throughout the review. The included systems were operationally classified according to albumin source and form, interface architecture, attachment method, conformational assessment, expected exchange potential, intended interfacial role, and the available biological-medium and interface-stability evidence (Table 2). Experimental context, in vivo sample size, dose and administration route, comparator structure, principal reported outcomes, pharmacokinetic assessment, and safety evaluation are summarized in Table 3.

2. Diagnostic imaging platforms

Pre-engineered albumin-containing interfaces may improve diagnostic nanoparticle systems by enhancing colloidal stability while preserving signal-generating functions. Three studies illustrate this principle through magnetic resonance and magnetic particle imaging (MRI and MPI), fluorescence-based cancer-cell detection, and long-term computed tomography (CT) tracking of HSA-fixed iron oxide nanoparticles. Collectively, these examples support formulation-specific diagnostic roles for engineered albumin interfaces, although their biological validation remains limited.

2.1. Magnetic resonance and magnetic particle imaging

Baki et al. developed BSA-coated single-core iron oxide nanoparticles as candidate dual-modality MRI/MPI contrast agents. BSA deposition increased the hydrodynamic diameter from 26.5 to 42 nm and shifted the zeta potential from approximately −51 to −25 mV. The coated particles remained colloidally stable for one week in saline media, whereas the uncoated particles aggregated or precipitated at higher NaCl concentrations, indicating that the clearest contribution of BSA was improved interfacial stabilization. The formulation exhibited high transverse relaxivity ($r_2 = 600 \pm 10$ L·mol^{-1}·s^{-1} at 1.5 T) and an MPI third-harmonic amplitude exceeding that of Resovist®. However, these imaging properties were attributed primarily to the optimized single-core architecture and particle fractionation. Indeed, BSA coating reduced the specific third-harmonic amplitude from 33.9 to 26 A·m^2·kg^{-1} Fe, probably because the larger hydrodynamic size restricted magnetic relaxation. Thus, BSA mainly improved saline stability while preserving much of the core-dependent MRI and MPI performance. A major limitation of this study was the absence of biological evaluation. Stability was assessed exclusively in NaCl solutions rather than serum, plasma, whole blood, or cell-containing biological media. No cellular uptake, cytotoxicity, pharmacokinetic, biodistribution, or in vivo imaging experiments were performed. The authors explicitly identified evaluation in plasma, whole blood, and living cells as future work [12].

2.2. Long-Term CT tracking of HSA-fixed iron oxide nanoparticles

Bychkova et al. [13] evaluated free-radical-fixed HSA-coated iron oxide nanoparticles (IONPs) for CT imaging in a rat model of PC-1 hepatocellular carcinoma. Following direct intraarterial administration into the tumor vascular bed, CT-visible vascular contrast persisted for 14 days. However, this finding indicates prolonged local retention of CT-detectable material rather than preservation of intact nanoparticles or their HSA interface, and the regional administration model does not demonstrate systemic tumor targeting. Because no uncoated IONP comparator was included in vivo, the observed contrast and local retention cannot be attributed specifically to HSA and should instead be assigned to the complete HSA-IONP formulation. The absence of pharmacokinetic, quantitative biodistribution, and therapeutic evaluation further precludes classification of the platform as a demonstrated theranostic system [13].

2.3. Fluorescence-based cancer cell detection

Wu et al. took a fundamentally different approach, constructing a preformed adsorption-derived BSA-gold nanocluster (AuNC) layer, described by the authors as a hard protein corona, on sulfate-modified polystyrene (PS) nanoparticles as a dual-color fluorescence probe for breast-cancer cell detection in vitro and xenografted tumor-tissue detection ex vivo. The BSA-containing interface served three functions: BSA acted as the template for synthesizing AuNCs, the adsorbed BSA-AuNC layer improved the colloidal stability of the PS nanoparticles, and the albumin component provided reactive sites for conjugating EpCAM-targeting aptamers through 1-ethyl-3-(3-dimethylaminopropyl) carbodiimide and N-hydroxysuccinimide (EDC/NHS coupling). The resulting construct provided dual-color imaging through green fluorescence from the PS core and red fluorescence from the BSA-AuNC layer. Flow cytometry showed 92.6% positivity in EpCAM-expressing MCF-7 cells treated with PS-BSA-AuNCs-Apt, compared with 23.7% for cells treated with the non-aptamer construct, while substantially lower positivity was observed in the investigated non-target cell lines. These findings demonstrate aptamer-dependent selective cell association under the investigated in vitro conditions. Ex vivo testing of frozen xenograft sections also showed stronger green and red fluorescence in EpCAM-positive MCF-7 tumors than in EpCAM-negative HeLa tumors (Fig. 2). The BSA-AuNC interface reduced the aggregation observed for bare PS nanoparticles after 30 min in 10% human serum, supporting short-term colloidal stabilization under the tested conditions. However, this experiment does not demonstrate prolonged stability, preservation of aptamer accessibility, or maintained targeting after secondary-corona formation. The authors acknowledged that additional protein adsorption in biological environments might mask the targeting groups and

Table 1
Study-level evidence coverage across physicochemical, biological, proteomic, pharmacokinetic, imaging/biodistribution, and in vivo efficacy domains.

Review theme		Study	Physicochemical characterization	Serum or plasma stability	Cell-based testing	Corona proteomics	Animal imaging or biodistribution	PK evaluation	In vivo efficacy
A. Diagnostic imaging	1	Baki et al. (2021)	size, shell thickness, zeta, MRI relaxivity/MPI	only 0.05-0.15 M NaCl, 2 h to 1 week	no cell assay	NR	NR	NR	NR
	2	Wu T. et al. (2022)	size, fluorescence, aptamer conjugation	DLS after 30 min in 10% human serum or PBS	MCF-7, MCF-10A, HEK-293T	NR	ex vivo tumor tissue only	NR	NR
	3	Bychkova et al. (2022)	DLS, TEM-derived shell, EMR, peroxidase activity	IgG challenge and coating-retention tests; no serum proteomics	NR	NR	CT of tumor vascular bed at 30 min and 14 days	NR	NR
B. Theranostic and multimodal therapeutic platforms	4	Zhang et al. (2023)	size, zeta, biomineralization, MRI, photothermal, Fe^{3+} release	water/PBS and 30 min in 10% FBS; BSA/Tf ELISA	4T1 uptake and therapeutic assays	NR	tumor MRI and organ distribution	MRI-based clearance, no plasma PK	4T1 mouse efficacy
	5	Petrov et al. (2025)	DLS, TEM, FTIR, zeta, MRI, DOX loading/release	only pH 4.0-8.5 buffers and 0.15 M NaCl	A549 IC50	NR	NR	NR	NR
	6	Suwannasing et al. (2025)	DLS, zeta, SEM, EDS, FTIR, BSA immobilization	no serum or plasma challenge	U87-MG MTT, clonogenic, γ-H2AX, apoptosis, cell cycle	NR	NR	NR	NR
	7	*Caputo et al. (2026)*	*TEM, DLS, zeta, MRI relaxivity, drug loading*	*DLS in PBS and medium with 10% FBS for 7 days*	*MCF-7, MDA-MB-231, spheroids, Caco-2 barrier model*	*NR*	*NR*	*NR*	*NR*
	8	Bychkova et al. (2025)	DLS, EMR, coating integrity, folate and MB loading	NR; IgG challenge/coating-retention only	MCF-7 and MDA-MB-231 uptake and PDT	NR	NR	NR	NR
	9	Carrese et al. (2023)	DLS, zeta, uptake, photothermal and photoacoustic testing	NR	HS578T and MCF10a spheroids	NR	in vitro photoacoustic spheroid imaging only	NR	NR
	10	Ghosh et al. (2025)	TEM, DLS, TGA, CD, CT, SPECT, radiochemical stability	PBS and mouse-serum radiochemical stability	B16F10 RT, PTT, and combined treatment	NR	SPECT/CT, autoradiography, organ biodistribution	time-point biodistribution only; no plasma PK	B16F10 mouse efficacy
	11	Nosrati et al. (2020)	TEM, DLS, zeta, loading, release, magnetization	NR	4T1 uptake, viability, apoptosis; HEK-293 and hemolysis	NR	NR	NR	4T1 mouse efficacy
	12	Amatya et al. (2023)	TEM, DLS, zeta, FTIR, UV-vis, photothermal stability	storage only; no serum challenge	U87-MG, A431, B16F10 and photothermal testing	NR	NR	plasma ICG signal, half-life and AUC	NR
	13	Dongsheng Li et al. (2023)	SEM, TEM, DLS, zeta, FTIR, loading and release	NR	AGS gastric-cancer chemo-photothermal assays	NR	NR	NR	NR
	14	Ayatollahi et al. (2022)	SEM, DLS, zeta, FTIR, loading and folate binding	NR	Ntera-2 and HFF viability, apoptosis, gene expression	NR	NR	NR	NR
C. Biological identity / stealth	15	Traverso et al. (2023)	size, electrophoresis, fluorescence, protein activity	DLS after 30 min in PBS ± 50% FBS	A549, 16HBE14o-, SH-SY5Y, ARPE-19	NR	local ocular distribution at 24 h after subconjunctival injection	NR	NR
	16	Bozzer et al. (2024)	DLS, TEM, ELISA, Western blotting	long-term PBS plus 1 h diluted normal human serum	macrophage uptake, NALM-6 targeting, cytotoxicity	LC-MS/MS after pooled normal human serum incubation	zebrafish fluorescence and bloodstream retention	restricted time-point retention, no full PK	zebrafish tumor suppression and survival

(*continued on next page*)

Table 1 (*continued*)

	17	Kumar et al. (2024)	spectroscopy, DLS, zeta, electric-field effects	NR	hemolysis only, no cancer-cell assays	NR	NR	NR	NR
	18	Olivieri et al. (2024)	silica-core size, DLS, zeta, coating stoichiometry, spectroscopy	uptake tested in complete medium with 10% FBS; no direct coating-retention assay	CHO-K1, GAG-deficient pgsA-745, and HeLa uptake and paclitaxel cytotoxicity	Contextual FBS-corona profiling only	NR	NR	NR
D. Cancer delivery / barrier	19	Li et al. (2020)	size, zeta, morphology, loading, release	20% FBS at 37 °C for 48 h	A549 uptake and viability	NR	IVIS tumors and organs	~6 h half-life vs 15 min free DOX	A549 xenograft efficacy
	20	Tan et al. (2021)	size, zeta, TEM, loading, release kinetics	transmittance in 50% FBS for 72 h	4T1 uptake, cytotoxicity, competition	NR	tumor and organ DOX distribution	tissue distribution only, no plasma PK	4T1 tumor inhibition and survival
	21	Yang et al. (2021)	size, zeta, TEM, siRNA binding	30 min in 10% FBS; siRNA protection in 50% FBS for 24 h	Bel-7402 uptake, VEGF silencing, MTT	SDS-PAGE/BCA only	NR	NR	Bel-7402 xenograft efficacy
	22	Wu Z. et al. (2024)	size, zeta, morphology, siRNA protection	10% mouse serum or FBS up to 4 h; FITC-BcR retention qualitative	uptake, proliferation, migration, VEGF silencing	LC-MS/MS after ex vivo incubation with tumor-bearing-mouse serum	NR	NR	xenograft antiangiogenic efficacy
	23	Palazzolo et al. (2024)	albumin-coated nanocrystal characterization	MAGL23 in 50% FBS up to 168 h and microsomes; drug stability, not HSA retention	not evaluated in the included 2024 study	NR	tumor drug concentration only	plasma MAGL23, 0-24 h, AUC	OVCAR5 xenograft efficacy
	24	Leung et al. (2021)	DLS, zeta, TEM, FTIR, MALDI, RGD conjugation	DLS in PBS, 1 M NaCl, HEPES + 0.1% BSA, DMEM + 10% FBS	U-87 MG, bEnd.3, C8-D1A; in vitro BBB model	NR	in vivo/ex vivo fluorescence, brain sections, tumor TEM, organ histology	single 24 h imaging time point only	imaging and brain-tumor accumulation only
	25	Goel et al. (2026)	DLS, zeta potential, TEM, FTIR, UV-vis, PXRD, EDX/ICP-MS, VSM, TGA	NR; water-only DLS showed PDI 0.434 and partial aggregation	H1299, HEK-293, migration, clonogenic, apoptosis, hemolysis	NR	NR	NR	NR
	26	Afonso et al. (2024)	DoE, DLS, zeta potential, PDI, pDNA complexation, SEM	4 h pDNA protection in DMEM plus 10% FBS or 10% FBS; particle and BSA-interface stability not measured	U87, HA1800 astrocytes, p53 transcription, rat-erythrocyte hemolysis	NR	NR	NR	NR
	27	Iqbal et al. (2022)	DLS, TEM, zeta, PDI, loading, release	96 h in aqueous physiological media; no serum challenge	4T1 uptake, inhibition, competition, cytotoxicity	NR	tumor and organ lapatinib distribution	plasma concentration, 0 to 24 h, half-life and AUC	4T1 mouse efficacy
	28	Carrese et al. (2021)	DLS, zeta, HSA and DOX binding, release, photothermal testing	NR	HS578T uptake and viability; MCF10a viability	NR	NR	NR	NR
	29	Mahmoud et al. (2024)	DLS, zeta, TEM, UV-vis, BSA quantification	NR	MDA-MB-231 viability, uptake, migration, adhesion	NR	NR	NR	NR
	30	Zhang et al. (2026)	DLS, zeta, TEM, Pt release, oxidative stability	72 h in 10% FBS and other media, DLS only	4T1 proliferation, apoptosis, ROS, DNA damage, metabolism	NR	NR	NR	4T1 mouse efficacy
	31	Li et al. (2021)	DLS, zeta, XRD, loading and release	PBS and culture-medium DLS; no serum proteomics	HCT-116 uptake, viability, apoptosis, cell cycle	NR	tumor accumulation and organ histology	NR	HCT-116 mouse efficacy

(*continued on next page*)

Table 1 (*continued*)

	32 Kim et al. (2021)	TEM, DLS, zeta, UV-vis, FTIR, BSA and Ag quantification	five-day size stability in water only	B16F10 and HUVEC assays	NR	NR	NR	NR
	33 Zareian Baghdadabad et al. (2026)	TEM of AgNPs, DLS, UV-vis	indirect culture-medium observation only	PC3 and LNCaP viability, migration, colonies, apoptosis, cell cycle, ROS and gene expression	NR	NR	NR	NR
	34 Hashemi et al. (2025)	TEM, DLS, zeta, XRD, FTIR, UV-vis, loading and release	NR	4T1 viability with quercetin and 4 Gy irradiation	NR	healthy-mouse survival and blood panels only	NR	NR
	35 Zhao et al. (2021)	TEM, DLS, zeta, FTIR, UV-vis-NIR, photothermal heating	NR	4T1 viability and photothermal treatment	NR	IV blood persistence and organ biodistribution; efficacy used intratumoral dosing	limited blood-concentration time course	4T1 tumor-growth study, n = 2 per group

■ Reported ■ Limited ■ Not reported: NR
No studies included in this review reported validation in cancer-patient cohorts.

alter their activity [14].

2.4. Critical comparison and gaps

Across the three diagnostic platforms, the albumin interface performed non-equivalent functions: colloidal stabilization in the Baki et al. system, formation of a stabilized protein coating in the Bychkova et al. [13] formulation, and provision of a fluorescent and bioconjugation scaffold in the Wu et al. platform. The corresponding evidence ranged from physicochemical contrast-agent characterization to regionally administered in vivo CT visualization and ligand-directed in vitro and ex vivo detection. These different experimental levels preclude direct comparison and do not establish a general albumin-mediated enhancement of diagnostic performance. Collectively, the studies support formulation-specific enabling roles for albumin, but not an albumin-specific improvement in systemic tumor targeting or diagnostic accuracy. Matched albumin-free comparisons under biologically relevant conditions, systemic pharmacokinetics, secondary-corona analysis, and prospective diagnostic validation remain unaddressed.

3. Diagnostic and/or therapeutic platforms

Building on the diagnostic imaging systems discussed above, this section examines albumin surface-engineered platforms developed for therapeutic or combined theranostic applications. The evidence ranges from in vivo MRI and single-photon emission computed tomography/computed tomography (SPECT/CT) imaging combined with therapy to in vitro photoacoustic, photodynamic, radiosensitizing, drug-delivery, and barrier-transport systems. Because the degree of functional integration varies substantially, platforms are described as theranostic only when both diagnostic and therapeutic functions were experimentally demonstrated; otherwise, the reported outcomes are classified according to the functions directly evaluated.

3.1. Ferroptosis and photothermal therapy with dual MRI

Zhang et al. investigated a BSA-templated biomineralized interface on Fe_3O_4 nanoparticles and developed an Fe_3O_4@BSA-TA-Fe^{3+} nanoprobe. BSA served as a biomineralization template for coordinating tannic acid (TA)-Fe^{3+} complexes onto the magnetite cores [15]. The BSA interface acted as the structural scaffold for TA-Fe^{3+} complexation, whereas the resulting biomineral layer, rather than BSA alone, preferentially adsorbed unsaturated transferrin, including apo-transferrin, from serum. This enrichment was proposed to facilitate transferrin-receptor (TfR)-mediated tumor targeting. Comparison of Fe_3O_4 with Fe_3O_4@BSA supports a coating-associated improvement in colloidal dispersion. However, transferrin enrichment was an associative observation, and its causal involvement in TfR-mediated targeting was not tested through receptor blocking, knockdown, or transferrin-depletion experiments. The nanoprobe combined pH-responsive T_1-weighted contrast with Fe_3O_4-dependent T_2-weighted contrast (Fig. 3). Its longitudinal relaxivity increased by approximately 96% as the pH decreased from 7.4 to 4.5, whereas transverse relaxivity remained approximately constant. The spatial mismatch between the T_1 and T_2 signals was interpreted as potentially reflecting intratumoral pH heterogeneity, but quantitative pH mapping was not directly validated. Therapeutically, 808 nm irradiation produced photothermal heating, while pH-triggered Fe^{3+} release promoted intracellular Fenton reactions associated with ferroptosis. In the syngeneic 4T1 tumor model, the complete formulation combined with irradiation produced tumor disappearance in 5/5 mice, with no observed recurrence during the 20-day follow-up. However, longer-term recurrence and survival were not evaluated. Moreover, because an albumin-free but otherwise matched Fe_3O_4-TA-Fe^{3+} construct was not tested, this outcome should be attributed to the complete Fe_3O_4@BSA-TA-Fe^{3+} formulation and irradiation rather than exclusively to BSA.

3.2. Magnetically targeted chemotherapy with MRI potential

Petrov et al. developed HSA-coated, oleic-acid-functionalized magnetite nanoparticles (MNP_OA_HSA) for doxorubicin (DOX) delivery with MRI-related relaxometric potential. HSA coating increased the measured DOX loading from 650 to 725 μg/mg of nanoparticle. The authors attributed this increase to additional DOX-binding sites provided by HSA, superimposed on interactions with the hydrophobic OA-containing surface. However, this mechanistic interpretation was not tested through site-blocking or quantitative binding studies [16].

MNP_OA_HSA released approximately 68–70% of DOX at pH 4.5, compared with approximately 44–45% at pH 7.4 after 120 min. The Tween 20-containing MNP_OA_TW20_HSA formulation showed still greater release under acidic conditions, indicating that release depended on the complete interfacial composition rather than HSA alone. Although the release data were fitted to the Korsmeyer–Peppas model

Table 2
Mechanistic classification of albumin surface and interface systems included in this review.

Study, nanosystem, and reported size	Albumin source and form	Interface class and architecture	Attachment or immobilization	Albumin conformational assessment	Exchange evidence and inferred potential	Intended interfacial role	Biological-medium and interface-stability evidence
Baki et al., 2021 Fe_3O_4 MNPs, 42 nm	BSA	I-A: preformed, adsorption-derived BSA layer	10 mg/mL BSA, pH approximately 8.5, 60°C for 12 h, followed by magnetic purification and washing; no coupling reagent	Not assessed after coating; the effect of the 60°C treatment was not determined	Not measured; moderate to high exchange inferred from noncovalent attachment	Colloidal stabilization; MRI/MPI compatibility	Stable in 0.05–0.15 M NaCl for 2 h to 1 week. No serum, plasma, whole-blood, or direct BSA-retention test
Wu T. et al., 2022 sulfate-PS/BSA-AuNC/Apt, 140.1 nm	BSA-AuNC composite	I-B: hybrid BSA-AuNC hard adsorption layer bearing aptamer	BSA-AuNCs physically adsorbed to sulfate-PS for 15 min. EDC/NHS coupled the aptamer to BSA, not BSA to PS	Not assessed after alkaline AuNC synthesis; native BSA folding cannot be assumed	Not measured; moderate exchange inferred despite the hard, multivalent layer	Colloidal stabilization; dual fluorescence; aptamer display	DLS after 30 min in PBS or 10% human serum. No direct tracing of the original BSA-AuNC layer or long-term biofluid test
Zhang et al., 2023 Fe_3O_4@BSA-TA-Fe^{3+}, 64.8 nm	BSA	I-B: adsorbed BSA mineralization template with an acquired transferrin-rich corona	BSA adsorbed noncovalently to carboxylated Fe_3O_4; free BSA was removed before TA-Fe^{3+} mineralization	Not assessed after adsorption and mineralization	Not measured; moderate exchange inferred. Mineralization may constrain BSA, while the acquired outer corona remains dynamic	Stabilization; biomineralization; transferrin recruitment; MRI, PTT, and ferroptosis	Stability reported in water and PBS. After 30 min in 10% FBS, BSA and transferrin were measured by ELISA, but coating BSA could not be distinguished from serum BSA
Petrov et al., 2025 OA/OA-Tween20-Fe_3O_4, 176 nm	HSA	I-A: preformed, adsorption-derived HSA layer	Overnight adsorption at 25°C onto OA-containing MNPs, followed by magnetic separation and washing; no covalent coupling	FTIR confirmed amide bands, but secondary and tertiary structure were not resolved	Not measured; moderate to high exchange inferred. Acidic rearrangement or partial desorption was proposed	Colloidal stabilization; DOX binding and release; MRI relaxometry	DLS in pH 4.0–8.5 buffers and 0.15 M NaCl. No serum, plasma, or direct HSA-retention assay
Suwannasing et al., 2025 BSA@CuO, approximately 300 nm	BSA	II: EDC/NHS-assisted fixed BSA layer, as assigned by the authors; covalency uncertain	EDC/NHS/BSA reacted with CuO for 24 h. Formation of a covalent amide bond on bare CuO was not independently demonstrated	Amide I and II bands confirmed BSA presence, but native folding was not established	Not measured; low exchange if covalent coupling occurred, otherwise uncertain	Dispersion and biocompatibility; radiosensitization	Single DLS comparison in PBS. No longitudinal, serum, plasma, or direct interface-retention assessment
Traverso et al., 2023 HSA/hTf-CdSe/ZnS QDs, 17–21 nm	HSA; outer HSA or hTf	II: crosslinked, denatured HSA multilayer with an outer native-like HSA or hTf layer	QDs were sonicated with HSA and glutaraldehyde and heated to 60°C; the activated multilayer was then decorated with HSA or hTf	Inner HSA was denatured and crosslinked. The outer layer was considered native-like from electrophoretic behavior but was not quantitatively resolved	Not measured; low exchange inferred from crosslinking	Passivation; native-protein presentation; drug carriage	DLS size was unchanged after exposure to 50% FBS under the tested conditions. DLS did not assess protein exchange, displacement, or secondary-corona composition
Bozzer et al., 2024 HSA-PLGA-PVA NPs, 348.7 nm	HSA	II: covalently fixed HSA layer beneath an acquired human-serum corona	EDC/sulfo-NHS coupling between PLGA surface carboxyl groups and HSA amines	ELISA and Western blot confirmed HSA presence; folding, orientation, and receptor accessibility were not assessed	Not measured; low exchange inferred from covalent coupling	Acquired-corona remodeling; reduced phagocytosis; targeting and drug delivery	Particle size was monitored for up to 10 months at 4°C; the acquired corona was profiled after 1 h in 10% human serum. Prebound HSA was not separately traced
Kumar et al., 2024 BSA-citrate-AuNPs, 32.9–43.5 nm	BSA, DC-field treated	I-B: DC-field-modified, noncovalent BSA interface	A BSA monolayer formed at 15 μM; 0–30 V DC was applied for 3 min while free BSA remained, inducing additional	Minimal perturbation at 5 V, increasing above 5 V; marked aggregation at 30 V	Not measured; moderate to high exchange inferred from the noncovalent multilayer	Interface modulation; curcumin binding	Immediate DLS and zeta-potential characterization only. No time-course, serum, plasma, or direct BSA-retention test

(*continued on next page*)

Table 2 (*continued*)

Study, nanosystem, and reported size	Albumin source and form	Interface class and architecture	Attachment or immobilization	Albumin conformational assessment	Exchange evidence and inferred potential	Intended interfacial role	Biological-medium and interface-stability evidence
			adsorption; no coupling reagent				
Leung et al., 2021 RGD-dcBSA-PEG nanodiamonds, 73.3 nm	Cationized, reduced, denatured BSA; PEGylated and RGD-modified	I-B: modified protein-polymer interface on carboxylated nanodiamonds	BSA was cationized, PEGylated, reduced and denatured, then adsorbed overnight; no nanoparticle-protein coupling reagent	Deliberately reduced and denatured; native albumin structure and receptor functions cannot be assumed	Not measured; moderate exchange inferred from multivalent, noncovalent adsorption	Deaggregation and stabilization; PEG and RGD scaffold; barrier-model transport; imaging	DLS in several media, including DMEM with 10% FBS; incubation duration was not reported. No dcBSA exchange or recovered-layer assay
Li et al., 2020 BSA/HAP/DOX, 68.4 nm	BSA	I-A: preformed, adsorption-derived BSA layer	BSA was incubated with amine-functionalized HAP/DOX for 1 h at room temperature; no coupling reagent	Not assessed	Not measured; moderate to high exchange inferred from noncovalent adsorption	Charge reversal; serum stabilization; hemocompatibility; DOX delivery	Particle size remained stable in 20% FBS at 37°C for 48 h. BSA retention and exchange were not measured
Tan et al., 2021 BSA-CS-DOX NPs, 105.2 nm	BSA	I-A: adsorbed BSA layer on chondroitin-sulfate-containing nanoparticles	BSA was stirred with CS-DOX nanoparticles for 1 h; attachment was attributed to CS-protein affinity and electrostatic interactions	The tryptophan microenvironment was altered; global secondary and tertiary structure were not resolved	Not measured; moderate to high exchange inferred from noncovalent CS-BSA interactions	Serum shielding; targeting; sustained DOX release	Size and PDI were monitored for 1 week; approximately 90% transmittance was retained in 50% FBS for 72 h. BSA retention was not measured
Yang et al., 2021 Bc-coated TsR/siRNA NPs, 228.4 nm	BSA-cRGD (Bc)	I-B: ligand-functionalized, preformed Bc adsorption layer	cRGD was covalently linked to BSA using BS3; Bc was then electrostatically adsorbed to TsR/siRNA nanoparticles	Not assessed after BS3 conjugation and adsorption; SDS-PAGE demonstrated mass change, not folding	Direct short-term evidence: Bc remained after 30 min in 10% FBS but detached substantially at pH 4.0–4.7; longer kinetics were not measured	Serum shielding; cRGD targeting; siRNA protection; acid-detachable interface	DLS after serum dilution and siRNA protection in 50% FBS for 24 h. SDS-PAGE and BCA supported short-term Bc retention and acidic detachment
Wu Z. et al., 2024 BcR-coated CsR/siRNA NPs, 172.2 nm	BSA-cRGD (BcR); BSA supplier not reported	I-B: ligand-functionalized BcR layer beneath an acquired tumor-serum corona	BcR was electrostatically adsorbed to CsR/siRNA nanoparticles; cRGD was covalently linked to BSA	Not assessed after cRGD conjugation and adsorption	Direct short-term evidence: FITC-BcR remained after 1 h in 10% serum or FBS, indicating incomplete displacement; longer kinetics were not measured	Serum shielding; cRGD targeting; acquired-corona modulation; siVEGF delivery	DLS and siRNA protection in 10% serum for up to 4 h; FITC-BcR retention at 1 h. Proteomics used ex vivo serum incubation, not particles recovered after administration
Palazzolo et al., 2024 HSA-MAGL23/F127 nanocrystals, 395.4 nm	HSA	III: HSA-stabilized drug-nanocrystal interface	HSA was added to F127-stabilized nanocrystals for 24 h, followed by washing; noncovalent adsorption or surfactant exchange	Not assessed	Not measured; moderate to high exchange inferred from noncovalent surface association	Nanocrystal stabilization; increased aqueous drug content; prolonged release and delivery	MAGL23 was measured after incubation in 50% FBS for up to 168 h and in microsomes for 40–60 min. Particle integrity and HSA-layer retention were not measured
Goel et al., 2026 CoFe2O4@BSA@Ag, 176.2 nm	BSA	I-B: hybrid adsorption-derived BSA/silver interface on a non-albumin magnetic core	BSA was adsorbed to CoFe2O4 for 24 h in PBS through reported electrostatic and hydrophobic interactions, followed by washing; AgNO3 was then added	Not assessed; FTIR and UV–vis supported association but did not establish preservation of BSA folding	Not measured; moderate to high exchange inferred from noncovalent adsorption	Stabilization and silver-deposition scaffold; anticancer functionality	DLS was performed only in water. The final composite had PDI 0.434 and partial aggregation; serum stability, BSA retention, and exchange

(*continued on next page*)

Table 2 (*continued*)

Study, nanosystem, and reported size	Albumin source and form	Interface class and architecture	Attachment or immobilization	Albumin conformational assessment	Exchange evidence and inferred potential	Intended interfacial role	Biological-medium and interface-stability evidence
			overnight to deposit silver on the BSA-containing interface				were not measured
Afonso et al., 2024 BSA-TMZ-WRAP5/p53, 182.3 nm	BSA	I-A: noncovalent BSA layer on a peptide-DNA core	BSA (0.08%) was added 25 min after core formation; no coupling reagent	Not assessed	Not measured; moderate to high exchange inferred	Surface modulation; TMZ-p53 co-delivery; hemocompatibility	Both formulations protected pDNA for 4 h in medium with FBS. Particle stability, BSA retention, exchange, and corona composition were not measured
Iqbal et al., 2022 BSA-coated PLGA-lapatinib, 155 nm by DLS	BSA	I-A: preformed noncovalent BSA outer coating on a PLGA-lapatinib core	PLGA-lapatinib emulsion was transferred into 5% BSA, sonicated, stirred, centrifuged, washed, and lyophilized	Not assessed	Not measured; moderate to high exchange inferred from noncovalent coating	Colloidal stabilization, pH-responsive release, tumor delivery	Size monitored for 96 h in water, PBS, DMEM, saline, and glucose at 4°C. No serum, plasma, or direct BSA-retention assay
Carrese et al., 2021 MelaSil_Ag-HSA@DOX, 407 nm	Recombinant HSA	I-B: hybrid HSA-functionalized interface on silica-melanin-silver nanoparticles with HSA-bound DOX	HSA was described as bonded using a previously reported functionalization protocol; the detailed linkage procedure was not restated	Tryptophan quenching suggested retained DOX-binding-site accessibility, not global native conformation	Not measured; exchange potential cannot be determined from the reported data	DOX binding, pH-responsive release, cell interaction, chemo-photothermal therapy	No serum, plasma, whole-blood, secondary-corona, or direct HSA-retention study
Mahmoud et al., 2024 GNR-BSA, 128 nm; GNS-BSA, 74.4 nm	BSA	I-A: adsorption-derived BSA layer on MPS-gold nanorods or citrate-gold nanospheres	4 mg BSA was mixed with 1 mL of 2 nM particles for 4 h below pH 5, followed by centrifugation	Not assessed; shape-dependent conformational change was discussed but not measured	Not measured; moderate to high exchange inferred from electrostatic and hydrophobic association	Colloidal stabilization and modulation of cancer-cell interaction	No serum, plasma, whole-blood, secondary-corona, or direct BSA-retention study
Zhang et al., 2026 Pt@BSA, 8.6 nm; Pt@BSA-RM, 112.4 nm	BSA	Boundary hybrid: BSA shell is exposed on Pt@BSA but buried beneath the red-blood-cell membrane in Pt@BSA-RM	Pt precursor was reacted in 8 mg/mL BSA at 80°C for 24 h and dialyzed; Pt@BSA was then extruded with erythrocyte membrane	Not assessed after heating or membrane cloaking	Not measured; BSA accessibility and retention beneath the membrane were not tested	Pt stabilization and radiosensitizer construction; the outer membrane dominates Pt@BSA-RM biological identity	Pt@BSA-RM size and zeta were monitored in 10% FBS and other media for 72 h. DLS does not establish BSA accessibility or secondary-corona resistance
Bychkova et al., 2022 HSA-IONPs, approximately 35 nm by DLS	HSA	II: free-radical-fixed HSA layer on iron oxide	HSA was immobilized during free-radical generation at the IONP surface; excess protein was magnetically removed	Not directly assessed; EMR and IgG challenge supported coating retention	Retention assessed indirectly; exchange in blood was not measured	CT tracking and potential magnetic or catalytic functionality	Coating stability assessed by DLS, EMR, magnetic separation, and IgG challenge. No plasma proteomics or in vivo HSA tracing
Caputo et al., 2026 ZnFe2O4@BSA-cisPt, 183.4 nm by DLS	BSA; HSA tested during method development	I-A/I-B: adsorbed BSA shell carrying cisplatin or fluorophore on zinc ferrite	2–5 mg/mL BSA was stirred with MNPs for 24 h at 4°C, then washed and size-exclusion purified	Not assessed	Additional serum adsorption was supported by DLS and electrophoresis	MRI contrast, cisplatin loading, fluorescence tracking, barrier transport	Stable in PBS and storage; size increased in 10% FBS medium over 7 days, showing additional protein adsorption
Bychkova et al., 2025 FA-HSA@IONPs with methylene blue	HSA modified with folate	I-B: folate-modified HSA coating on iron oxide with noncovalently bound photosensitizer	HSA coating was formed by the established free-radical method; folate was coupled to surface HSA and MB was adsorbed	Not directly assessed	Coating integrity and desorption assessed indirectly; biological-fluid exchange not measured	Folate targeting, PDT delivery, magnetic and catalytic potential	EMR, IgG challenge, and desorption tests; no plasma or secondary-corona analysis

(*continued on next page*)

Table 2 (*continued*)

Study, nanosystem, and reported size	Albumin source and form	Interface class and architecture	Attachment or immobilization	Albumin conformational assessment	Exchange evidence and inferred potential	Intended interfacial role	Biological-medium and interface-stability evidence
Carrese et al., 2023 MelaSil_Ag-HSA@DOX	Recombinant HSA	I-B: HSA-functionalized silica-melanin-silver interface with HSA-bound DOX	HSA functionalization followed the previously reported protocol; detailed coupling chemistry was not restated	Not assessed	Not measured	Photoacoustic signal, DOX delivery, photothermal treatment	No serum, plasma, secondary-corona, or direct HSA-retention study
Ghosh et al., 2025 [188Re]ReOx-HSA, 4–6 nm core	HSA	I-B: HSA-coated rhenium-oxide core with intrinsic radionuclide labeling	Rhenium precursor was reduced with NaBH4 in HSA-containing aqueous medium	CD showed reduced alpha-helical content after coating	Not measured directly	SPECT/CT, radiotherapy, photothermal therapy	Radiochemical stability in PBS and mouse serum; no direct HSA-retention or secondary-corona analysis
Nosrati et al., 2020 Fe3O4-Au-BSA-MTX-CUR	BSA bearing covalently attached MTX	I-B: adsorbed BSA-drug interface on an Fe3O4-Au heterodimer	EDC/NHS coupled MTX to BSA; BSA-MTX and curcumin were then assembled onto Fe3O4-Au and washed	Not assessed	Not measured	Drug delivery, radiosensitization, magnetic potential	No serum, plasma, secondary-corona, or direct BSA-retention study
Amatya et al., 2023 BSA-CuNPs, 93.5 nm by DLS	BSA	I-B: BSA-stabilized multidomain copper core	Cu2 + was complexed with BSA at pH 9 and reduced with NaBH4, followed by centrifugal purification	Not assessed	Not measured	Colloidal stabilization and photothermal treatment	Five-day storage and photothermal stability only; no serum or direct coating-retention test
Dongsheng Li et al., 2023 A-PFH/C-magnetite	Albumin, species not reported	I-B: albumin-functionalized magnetite carrying cisplatin and perfluorohexane	EDC/NHS treatment preceded 24 h albumin coupling; cisplatin and PFH were subsequently loaded	Not assessed	Not measured	Chemo-photothermal treatment and oxygen-carrier function	No serum, plasma, secondary-corona, or direct albumin-retention study
Ayatollahi et al., 2022 ZnO-BSA-DG-FA	BSA	I-B/II: glutaraldehyde-stabilized BSA interface on ZnO bearing diosgenin and folate	BSA was adsorbed to ZnO, diosgenin was incorporated, glutaraldehyde was added, and folate was coupled by EDC/NHS	Not assessed	Not measured	Drug solubilization and folate-associated cell targeting	No serum, plasma, secondary-corona, or direct BSA-retention study
Li et al., 2021 BLDH/5FU-ABX, 168.3 ± 2.0 nm	BSA plus albumin-bound paclitaxel	I-B: adsorbed composite albumin interface on 5FU-loaded Mg2Al LDH	LDH/5FU was added to 6 mg/mL BSA and stirred for 30 min; Abraxane was then incorporated by adsorption	Not assessed	Not measured; exchange cannot be separated between BSA and the Abraxane-derived albumin component	Colloidal stabilization and dual-drug delivery	DLS in PBS and culture medium; no direct albumin-retention, serum-proteomic, or secondary-corona analysis
Kim et al., 2021 BSA-silver NPs, 121.2 ± 43 nm by DLS	BSA	I-B: BSA-capped silver core	Silver nitrate was reduced with NaBH4 in BSA solution; unbound BSA was removed by centrifugal filtration	FTIR supported protein association; conformation not assessed	Not measured	Colloidal stabilization and silver-mediated photothermal treatment	Size monitored for five days in water; no serum, plasma, or coating-retention study
Zareian Baghdadabad et al., 2026 AgNPs-Alb, 76.70 ± 30.9 nm by DLS	BSA	I-B: BSA-containing interface around PVP-stabilized silver nanoparticles	5% BSA and AgNPs were emulsified with PBS, dichloromethane, ethanol, sonication, and solvent evaporation	Not assessed	Not measured	Enhanced cellular anticancer activity	No quantitative serum or plasma stability; absence of visible culture-medium precipitation was reported indirectly
Hashemi et al., 2025 MnFe2O4@BSA-quercetin, 98.13 ± 0.78 nm by DLS	BSA	I-A: noncovalently adsorbed BSA layer on manganese-ferrite cores	50 mg MnFe2O4 was incubated with 250 mg BSA for 12 h and dialyzed for 48 h before quercetin loading	Not assessed	Not measured; noncovalent exchange remains possible	Quercetin loading and pH-dependent release	No serum, plasma, secondary-corona, or direct BSA-retention study

(*continued on next page*)

Table 2 (*continued*)

Study, nanosystem, and reported size	Albumin source and form	Interface class and architecture	Attachment or immobilization	Albumin conformational assessment	Exchange evidence and inferred potential	Intended interfacial role	Biological-medium and interface-stability evidence
Olivieri et al., 2024 BSA-coated fluorescent silica NPs, 61 ± 1 nm for native BSA and 102 ± 14 nm for cationic BSA by DLS	Native BSA and chemically cationized or anionized BSA	I-A/I-B: adsorption-derived native or charge-modified BSA interface on a silica core	3 nM silica NPs were incubated with 10 mg/mL BSA variant in PBS for 24 h at 4 °C, then centrifuged and washed	Spectroscopic and computational analyses assessed BSA-variant interactions; preservation of native folding on particles was not fully established	Direct retention was not measured; uptake was tested in 10% FBS, and an FBS-derived corona was profiled contextually	Glycocalyx-dependent cellular uptake and paclitaxel delivery	Complete-medium uptake was assessed, but no flow, whole-blood, in vivo, or direct coating-retention study was reported
Zhao et al., 2021 AuNR@BSA, larger DLS mode 89.24 ± 42.24 nm	BSA	I-A/I-B: BSA layer replacing or overcoating a CTAB-rich gold-nanorod surface	AuNR@CTAB was mixed with 10 mg/mL BSA, sonicated, centrifuged, transferred to 5 mg/mL BSA at pH 11–12 for at least 18 h, and washed	Not assessed; FTIR supported BSA association, but residual CTAB was not quantified	Not measured	Reduced precursor-associated cytotoxicity and NIR-II photothermal treatment	No serum, plasma, secondary-corona, or direct BSA-retention study was reported

Note: Interfacial architecture was operationally classified as follows: I-A, simple preformed noncovalent albumin adsorption layer; I-B, modified or hybrid adsorption-derived albumin interface; II, fixed albumin layer formed by reported covalent immobilization or chemical crosslinking; and III, albumin-stabilized drug-nanocrystal interface. These review-specific categories do not represent standardized nomenclature. Expected dynamic exchange was inferred from the reported interfacial architecture unless albumin retention, displacement, or exchange was directly measured.

with high reported goodness of fit, the unusually low release exponents for MNP_OA_HSA (n = 0.09–0.10) and the absence of independent mechanistic validation limit their interpretation as definitive evidence of Fickian diffusion.

The r_2/r_1 ratio of 15.5 at 1.88 T indicated a relaxometric profile consistent with T_2-weighted behavior. However, comparison with the reported Resovist® ratio at 1.5 T cannot establish superior performance because the measurements were obtained at different magnetic-field strengths. Moreover, the absolute r_2 of MNP_OA_HSA was 5.58 $mM^{-1}\cdot s^{-1}$, compared with the reported value of 61.0 $mM^{-1}\cdot s^{-1}$ for Resovist®. Because no MRI experiments were performed, the study demonstrates MRI-related relaxometric potential rather than effective imaging performance.

The half-maximal inhibitory concentration (IC_{50}) against A549 lung adenocarcinoma cells was comparable to that of free DOX (0.7 versus 0.8 μg DOX/mL), providing no evidence of enhanced in vitro cytotoxic potency. No animal imaging, pharmacokinetic, biodistribution, efficacy, or other in vivo experiments were conducted.

3.3. Albumin-mediated radiosensitization

Suwannasing et al. addressed glioblastoma radiosensitization using BSA-coated CuO nanoparticles (BSA@CuO-NPs). The particles were prepared using EDC/NHS-mediated carbodiimide chemistry, although the authors indicated that both covalent and non-covalent interactions might contribute to stabilization of the BSA interface. The BSA coating substantially reduced the extensive aggregation observed for bare CuO nanoparticles in phosphate-buffered saline (PBS), supporting a coating-associated improvement in colloidal dispersion [17]. Cu^{2+}/Cu^{+} redox cycling, oxidative stress, and nanoparticle-mediated enhancement of radiation interactions were proposed as possible contributors to radiosensitization under 6 MV photon irradiation at 2 Gy. However, reactive oxygen species (ROS) generation, mitochondrial dysfunction, and the underlying radiation-interaction mechanisms were not directly measured. Clonogenic analysis demonstrated an enhanced radiation response, with the surviving fraction decreasing to 0.40 ± 0.06 for BSA@CuO-NPs combined with irradiation, compared with 0.58 ± 0.16 for radiation alone. The combination also increased phosphorylated histone γ-H2AX positivity from 46.5% after radiation alone to 81.4%, accompanied by increased apoptosis and G2/M-phase accumulation. These findings support increased radiation-associated DNA damage and reduced clonogenic survival, although they do not independently establish the proposed redox or physical mechanisms.

However, these data were obtained exclusively in U87-MG cells in vitro, with no in vivo validation or assessment of blood-brain barrier (BBB) transport, brain delivery, pharmacokinetics, or biodistribution. No non-malignant glial or neural cells were included, preventing evaluation of tumor selectivity and neural safety. Furthermore, the biological experiments lacked a matched bare-CuO nanoparticle group. The study therefore demonstrates radiosensitization by the complete BSA@CuO formulation but does not establish whether BSA independently enhanced radiosensitization relative to uncoated CuO nanoparticles.

3.4. MRI, drug delivery, and barrier-model evaluation

Caputo et al. noncovalently coated initially ethanol-dispersible zinc ferrite cores with an estimated 5.6 BSA molecules per particle, producing the aqueous MNP@BSA formulation [18]. Transmission electron microscopy (TEM) visualized a lower-contrast protein shell surrounding the inorganic cores, with a reported dry-shell thickness of 1.6 ± 0.3 nm (Fig. 4A). The directly demonstrated contributions of BSA were conversion of the inorganic cores into a water-dispersible platform and provision of an interfacial shell for cisplatin loading and fluorophore conjugation. Particle size remained essentially unchanged in PBS for one week, and the dispersions remained stable during two months of storage at 4 °C. In 10% fetal bovine serum (FBS), however, the hydrodynamic size increased progressively over seven days without visible precipitation. This indicates maintained dispersion despite continued serum-protein adsorption, rather than complete resistance to secondary-corona formation. BSA coating reduced saturation magnetization and therefore did not improve the intrinsic magnetic properties of the zinc ferrite core. Nevertheless, MNP@BSA retained measurable MR contrast in agarose at 1 T, with an r_2/r_1 ratio of 16.2, supporting a relaxometric profile consistent with T_2-weighted imaging. Albumin therefore added aqueous dispersibility and carrier and conjugation functions while preserving the core-derived imaging potential. MNP@BSA-cisPt entered MCF-7 spheroids and produced greater loss of viability than free cisplatin or unloaded MNP@BSA. However, this remains an outcome of the complete formulation because no albumin-free, cisplatin-loaded comparator was tested. Rhodamine-labelled MNP@BSA also showed transport across a Caco-2 monolayer, with an apparent

Table 3
Experimental context, in vivo sample size, dose and administration route, comparator structure, and principal reported outcomes of the included studies. N/A, not applicable because no in vivo administration was performed; NR, not reported in the primary publication or accessible supplementary information.

Study and formulation	Application and experimental model	In vivo sample size, dose, and administration route	Payload or modality	Albumin-relevant comparator or control	Principal reported outcome	Pharmacokinetic assessment	Safety or toxicity assessment
Baki et al., 2021 BSA-coated Fe_3O_4 MNPs	Enabling MRI/MPI study; no cancer cells or animals	Sample size: N/A; dose: N/A; route: N/A (no in vivo study).	MRI/MPI contrast; no therapeutic payload	Matched physicochemical control: uncoated Fe_3O_4 MNPs. Resovist benchmark; no alternative-protein control	BSA-coated MNPs showed $r_2 = 600\ L{\cdot}mol^{-1}{\cdot}s^{-1}$, approximately sixfold Resovist, with improved salt stability	Not evaluated	Not evaluated
Wu T. et al., 2022 PS-BSA-AuNC-Apt probe	Breast cancer: MCF-7 cells and ex vivo xenograft tumor sections	Sample size: NR; dose: N/A; route: N/A (ex vivo tumor sections only).	Dual fluorescence and EpCAM aptamer	No albumin-specific control. Aptamer-free comparisons isolated the aptamer contribution, not BSA	The complete probe achieved 92.6% MCF-7 detection and specific staining of xenograft tumor sections	Not evaluated	Not evaluated
Zhang et al., 2023 Fe_3O_4@BSA-TA-Fe^{3+}	4T1 breast cancer cells and tumor-bearing BALB/c mice; 20-day follow-up	Sample size: n = 5/group (25 mice total); dose: 10 mg Fe^{3+}/kg; route: intravenous, single administration.	TA-Fe^{3+}, MRI, PTT, and ferroptosis	Partial control: Fe_3O_4@BSA and treatment controls were included; no albumin-free TA-Fe^{3+} analog or TfR-blocking control	The complete formulation plus 808-nm irradiation eliminated tumors in 5/5 mice without recurrence during 20 days	Limited: serial MRI assessed tumor accumulation and qualitative biodistribution or clearance; no plasma concentration-time PK	In vitro cytotoxicity, body weight, major-organ histology, hematology, and blood biochemistry were assessed at the tested dose
Petrov et al., 2025 HSA-coated OA/OA-Tween20 Fe_3O_4 MNPs	Lung adenocarcinoma: A549 cells; in vitro only	Sample size: N/A; dose: N/A; route: N/A (in vitro only).	DOX delivery and MRI relaxometry	Matched control: OA or OA-Tween20 MNPs with and without HSA; free DOX comparison	The final formulations provided up to 725 μg DOX/mg NP, pH-dependent release, and an A549 IC_{50} of 0.7 μg/mL	Not evaluated	A549 viability was tested for blank and DOX-loaded carriers; no normal-cell, hemocompatibility, or in vivo safety assessment
Suwannasing et al., 2025 BSA@CuO nanoparticles	Glioblastoma: U87-MG cells with 2-Gy irradiation; in vitro only	Sample size: N/A; dose: N/A; route: N/A (in vitro only; BSA@CuO at IC_{20} with a single 2-Gy irradiation exposure).	X-ray radiosensitization; no drug payload	Bare CuO served as a physicochemical comparator; biological radiosensitization lacked a matched bare-CuO group	BSA@CuO plus 2 Gy produced a surviving fraction of 0.40 and 81.4% γ-H2AX-positive cells	Not evaluated	U87-MG viability, apoptosis, and cell-cycle effects were assessed; no normal-cell, hemocompatibility, or in vivo safety study
Traverso et al., 2023 HSA/hTf-decorated CdSe/ZnS QDs	A549 cancer cells, non-neoplastic 16HBE14o- cells, and local murine retinal uptake; no tumor model	Sample size: n = 3/group (12 mice total); dose: 10 μL containing 100 pM each of HSA-QDs and hTf-QDs; route: subconjunctival, single administration.	Digitoxin delivery and QD fluorescence	Partial control: outer HSA versus hTf identified an outer-protein effect; no albumin-free QD control	At 37 °C, hTf-QD uptake exceeded HSA-QD uptake by 8.2 particles per A549 cell; digitoxin-loaded QDs selectively reduced A549 cell number	Limited: local retinal distribution after subconjunctival injection; no systemic PK	A549 and 16HBE14o- cytotoxicity were assessed; blank particles showed low toxicity, but cadmium release remained a concern; no systemic safety study
Bozzer et al., 2024 HSA-PLGA-PVA nanoparticles	B-cell acute lymphoblastic leukemia: NALM-6 cells and human-zebrafish xenografts	Sample size: saline n = 26, free DOX n = 37, and doxo-t-NP n = 36; dose: 4.6 nL containing 1 μM free or encapsulated DOX; route: injection into the duct of Cuvier.	DOX delivery and anti-CD19 targeting	Matched in vitro control: NP versus NP-HSA. Targeted and untargeted HSA-NPs were tested in zebrafish, but no uncoated in vivo circulation comparator was included	NP-HSA altered the secondary corona and reduced macrophage uptake from approximately 35–20%; targeted DOX nanoparticles reduced tumor burden and improved zebrafish survival	Limited: fluorescence biodistribution in healthy and tumor-bearing zebrafish at 24 h; no plasma PK	RBC lysis, coagulation, complement, primary immune-cell interactions, and zebrafish survival were assessed; no mammalian systemic study
Kumar et al., 2024 DC-field-engineered BSA-AuNPs	Biophysical and hemolysis study; no cancer cells or animals	Sample size: N/A; dose: N/A; route: N/A (no in vivo study).	Curcumin-binding study	Matched biophysical controls: citrate-AuNP versus BSA-AuNP and a 0–30 V series; no biological albumin-specific control	DC exposure altered BSA-AuNP size and charge. The reported 2.5-fold Kapp increase at 5 V applied to free BSA-curcumin, not BSA-AuNP-curcumin	Not evaluated	Hemolysis only; no cellular or animal safety assessment
Leung et al., 2021 RGD-dcBSA-PEG nanodiamonds	U-87 MG cells, an in vitro endothelial barrier model, and U-87 MG xenograft mice	Sample size: dcBSA-PEG-ND n = 4, RGD-dcBSA-PEG-ND n = 4, and PBS n = 3; dose: 8.75 mg/kg; route: tail-vein	Cy7 fluorescence imaging; no therapeutic payload	No albumin-specific control. RGD versus non-RGD dcBSA-PEG nanodiamonds isolated the RGD contribution, not dcBSA	The complete system showed 53.5 ± 2.1% apparent transport across the in vitro barrier model and brain-tumor-associated	Limited: fluorescence biodistribution in xenograft mice; no plasma concentration-time PK	Viability was tested in three cell lines up to 1000 μg/mL; liver, kidney, and spleen histology showed no pathology under the tested

(*continued on next page*)

Table 3 (*continued*)

Study and formulation	Application and experimental model	In vivo sample size, dose, and administration route	Payload or modality	Albumin-relevant comparator or control	Principal reported outcome	Pharmacokinetic assessment	Safety or toxicity assessment
		injection, single administration.			fluorescence in mice; intact in vivo BBB crossing was not directly established		conditions; no long-term safety panel
Li et al., 2020 BSA/HAP/DOX nanoparticles	Non-small-cell lung cancer: A549 cells and A549 xenograft mice	Sample size: n = 6/group; dose: 5 mg DOX/kg every 2 days for 2 weeks; route: intravenous.	DOX delivery	Matched control: HAP/DOX versus BSA/HAP/DOX; free-BSA competition and free-DOX controls	The complete formulation showed an approximately 6-h blood half-life versus approximately 15 min for free DOX and a final tumor volume of 323 ± 52 mm^3	Formal: blood-persistence analysis and ex vivo organ or tumor biodistribution at 12 h	Hemolysis was 1.12% at 1 mg/mL; A549 viability and mouse body weight were assessed; no comprehensive organ pathology or clinical-chemistry panel
Tan et al., 2021 BSA-CS-DOX nanoparticles	Breast cancer: 4T1 cells and orthotopic 4T1 tumor-bearing mice	Sample size: efficacy n = 8/group and biodistribution n = 4/group; dose: 5 mg DOX/kg every 4 days for three doses; route: intravenous tail-vein injection.	DOX delivery	Matched control: BSA-coated BC-DOX versus BSA-free CS-DOX, with free-DOX and saline controls	82.8% tumor-volume reduction at day 18; separately, 91.4% tumor-weight inhibition; median survival 50 days	Limited: organ and tumor DOX distribution at 1 and 4 h and tumor-penetration imaging; no formal plasma PK	4T1 cytotoxicity, body weight, and major-organ histology were assessed; the complete formulation reduced cardiac and systemic toxicity at the tested dose
Yang et al., 2021 Bc-coated TsR/siVEGF nanoparticles	Hepatocellular carcinoma: Bel-7402 cells and xenograft mice; 10-day study	Sample size: n = 5/group; dose: 0.5 mg siRNA/kg on days 1, 3, 5, 7, and 9; route: tail-vein injection.	siVEGF delivery	Composite-interface control: TsR versus TsRBc. BSA and cRGD contributions could not be separated because BSA-only and cRGD-only surfaces were absent	The complete TsRBc/siVEGF formulation achieved 87% VEGF silencing and the greatest tumor-growth suppression among the tested groups	No formal PK or in vivo biodistribution; siRNA protection in plasma was assessed outside the animal for up to 24 h	Blank-carrier cytotoxicity in Bel-7402 cells and mouse body weight were assessed; no organ histology, hematology, or long-term toxicity evaluation
Wu Z. et al., 2024 BcR-coated CsR/siVEGF nanoparticles	Hepatocellular carcinoma and angiogenesis models: cellular assays and tumor-bearing nude mice; 10-day study	Sample size: n = 5/group; dose: NR; route: intravenous, five administrations over 10 days.	siVEGF delivery	Composite-interface control: CsR versus CsR/BcR. BSA and cRGD contributions could not be separated because BSA-only and cRGD-only surfaces were absent	The complete formulation reduced VEGF mRNA to approximately 30% of saline control, inhibited tumor angiogenesis, and altered the ex vivo serum-corona profile	Not evaluated; the tumor-bearing mouse-serum corona experiment was ex vivo and did not constitute in vivo PK	No comprehensive systemic safety or long-term toxicity assessment was reported
Palazzolo et al., 2024 HSA-MAGL23/F127 nanocrystals	Ovarian cancer: OVCAR5 cells and ovarian xenograft mice	Sample size: efficacy n = 6/group and pharmacokinetics n = 3/time point; dose: 20 mg/kg once weekly for four doses (efficacy) and 100 mg/kg once (pharmacokinetics); route: intraperitoneal.	MAGL23 inhibitor delivery	No albumin-specific control. MAGL23AF was compared with unformulated MAGL23 and vehicle, but no HSA-free F127 nanocrystal was included	The complete formulation produced 53% tumor inhibition, approximately 40% tumor necrosis, increased AUC, and slightly greater tumor accumulation	Formal: mouse plasma concentration-time analysis from 0 to 24 h and organ biodistribution	Mouse body weight, tolerability, and organ toxicity were assessed; the formulation avoided the spleen damage observed with unformulated MAGL23
Goel et al., 2026 $CoFe_2O_4$@BSA@Ag	Lung adenocarcinoma: H1299 cells; HEK-293 cells and human erythrocytes for in vitro safety	Sample size: N/A; dose: N/A; route: N/A (no in vivo study). In vitro experiments were generally performed in triplicate; H1299 exposure was 10–80 μg/mL for 48 h, with additional assays at 25–55 μg/mL	Silver-modified magnetic nanocomposite; no drug payload	Matched formulation controls: $CoFe_2O_4$ and CoFe2O4@BSA, plus cisplatin. CoFe2O4 versus CoFe2O4@BSA provided an albumin-associated comparison; CoFe2O4@BSA versus CoFe2O4@BSA@Ag isolated silver addition	The complete composite showed an H1299 IC50 of 38.28 μg/mL, approximately 67.3% apoptosis, and concentration-dependent inhibition of migration and colony formation	Not evaluated	HEK-293 viability remained above 70% at the tested higher concentrations; hemolysis was below 5% up to 100 μg/mL. No animal or long-term systemic safety study was performed
Afonso et al., 2024 BSA-coated TMZ-WRAP5/p53 nanocomplexes	Glioblastoma: U87 cells; HA1800 human astrocytes and rat erythrocytes for in vitro safety	Sample size: N/A; dose: N/A; route: N/A (no in vivo study). Optimization was validated in triplicate; cell-viability experiments used six independent measurements	Temozolomide and p53 plasmid co-delivery	Matched BSA-free TMZ-WRAP5/p53 complex; additional naked-pDNA, TMZ-only, non-transfected, and assay controls	BSA reduced hemolysis from 5.9% to 3.9% and increased U87 viability reduction relative to the BSA-free complex at 24 and 48 h, but not at 72 h; p53 transcription was shown qualitatively	Not evaluated	HA1800 viability remained above 90% and did not differ significantly between coated and uncoated complexes; hemolysis was 3.9% with BSA. No animal or long-term systemic safety study was performed

(*continued on next page*)

Table 3 (*continued*)

Study and formulation	Application and experimental model	In vivo sample size, dose, and administration route	Payload or modality	Albumin-relevant comparator or control	Principal reported outcome	Pharmacokinetic assessment	Safety or toxicity assessment
Iqbal et al., 2022 BSA-coated PLGA-lapatinib	4T1 breast cancer cells; healthy and subcutaneous 4T1 BALB/c female mice	PK: n = 5/group, one intravenous 10 mg/kg dose. Biodistribution: sample size not reported, one intravenous 10 mg/kg dose. Efficacy: n = 5/group, three intravenous 10 mg/kg doses	Lapatinib	Matched uncoated PLGA-lapatinib nanoparticles and free lapatinib; blank particles for selected assays	Coated particles increased uptake, plasma persistence, tumor drug concentration, and tumor growth inhibition relative to uncoated particles and free drug	Full plasma profile to 24 h: half-life 6.38 h and AUC 47.22 μg·h/mL for coated particles	Hemolysis, body weight, organ histology, and serum liver and kidney markers; toxicity group n = 3
Carrese et al., 2021 MelaSil_Ag-HSA@DOX	HS578T breast cancer and MCF10a mammary cells; no animal model	Sample size: N/A; dose and route: N/A, no in vivo study	Doxorubicin plus 808 nm photothermal treatment	Free DOX and HSA-functionalized carrier without DOX; no matched HSA-free hybrid carrier	Acid-sensitive DOX release and increased cell killing with the complete chemo-photothermal formulation	Not evaluated	MCF10a viability only; no animal or systemic toxicity evaluation
Mahmoud et al., 2024 GNR-BSA and GNS-BSA	MDA-MB-231 breast cancer cells, with prostate cell lines also tested; no animal model	Sample size: N/A; dose and route: N/A, no in vivo study	Unloaded gold nanorods or nanospheres	Untreated cells and comparison between coated shapes; no albumin-free biological control	Coated nanorods, but not nanospheres, reduced MDA-MB-231 viability and transiently retarded migration	Not evaluated	No normal-cell, animal, or systemic toxicity assessment
Zhang et al., 2026 Pt@BSA and Pt@BSA-RM	4T1 breast cancer cells and subcutaneous 4T1 BALB/c mice	Methods: n = 6/group; figures: n = 3/group. Intratumoral 2.5 mg/kg every 2 days, four doses; 5 Gy local X-ray after each dose	Platinum radiosensitizer and X-ray irradiation	Pt, Pt@BSA, Pt@BSA-RM, cisplatin, and irradiation controls; no albumin-free nanoparticle matched to Pt@BSA	Pt@BSA-RM plus irradiation produced the strongest tumor suppression, a composite membrane-level outcome	Not evaluated	Body weight and organ histology; no blood chemistry or hematology reported
Bychkova et al., 2022 HSA-IONPs	PC-1 hepatocellular carcinoma implanted in male rats	n = 6 total; 20, 40, or 60 μg IONPs per tumor; intraarterial regional administration	CT contrast; magnetic and peroxidase-like potential	Uncoated and adsorption-coated physicochemical controls; no uncoated in vivo comparator	Tumor vascular-bed CT contrast at 30 min and 14 days	Not evaluated	Behavior, body weight, local reaction, and limited pathology monitoring
Caputo et al., 2026 MNP@BSA-cisPt	MCF-7 and MDA-MB-231 cells, MCF-7 spheroids, Caco-2 monolayer	Sample size: N/A; dose and route: N/A, no in vivo study	MRI, rhodamine tracking, cisplatin	Bare MNP physicochemical controls, MNP@BSA, free cisplatin; no matched albumin-free drug carrier	MRI relaxivity, spheroid entry, cisplatin delivery, and in vitro epithelial transport	Not evaluated	2D and 3D viability only
Bychkova et al., 2025 MB/FA-HSA@IONPs	MDA-MB-231 and MCF-7 breast-cancer cells	Sample size: N/A; dose and route: N/A, no in vivo study	Methylene-blue PDT, fluorescence, magnetic potential	HSA@IONPs without folate, free MB, MB-HSA@IONPs, and component controls	Folate increased uptake and phototoxicity selectively in high-folate-receptor cells	Not evaluated	Dark cytotoxicity only; no systemic safety
Carrese et al., 2023 MelaSil_Ag-HSA@DOX	HS578T and MCF10a three-dimensional spheroids	Sample size: N/A; dose and route: N/A, no in vivo study	DOX, 808 nm PTT, photoacoustic imaging	Bare versus HSA-modified uptake; HSA carrier without DOX; no HSA-free DOX-loaded matched carrier	Spheroid penetration, photoacoustic signal, and chemo-photothermal cytotoxicity	Not evaluated	MCF10a spheroid viability only
Ghosh et al., 2025 [188Re]ReOx-HSA	B16F10 melanoma cells and subcutaneous tumors in C57BL/6 mice	n = 4/group for therapy; intratumoral 1.85 MBq for optimal RT/PTT, with 808 nm irradiation	SPECT/CT, CT contrast, 188Re RT, 808 nm PTT	Saline and modality controls; no albumin-free nanoparticle	Tumor retention and combined RT/PTT tumor-growth delay	Time-point organ biodistribution only; no plasma PK	Body weight, blood parameters, and major-organ histology
Nosrati et al., 2020 F-Au-BSA-MTX-CUR	4T1 cells and subcutaneous 4T1 BALB/c mice	n = 5/group across 12 groups; one intravenous 125 μL dose of 6 mg/mL formulation; 2, 4, or 6 Gy X-ray	MTX, curcumin, X-ray radiosensitization	Multiple formulation and radiation controls; no albumin-free matched F-Au-drug formulation	Complete formulation plus radiation reduced tumor growth	Not evaluated	HEK-293 viability, hemolysis, LD50, body weight, and organ histology
Amatya et al., 2023 BSA-CuNPs	U87-MG, A431, B16F10 cells; healthy C57BL/6 mice	MTD: n = 3/dose, intravenous. PK: n = 5, intravenous ICG-loaded particles, 420 μg ICG/kg and 40 mg BSA/kg	885 nm photothermal treatment	CuSO4, BSA-Cu2 + complex, laser-only controls; no albumin-free CuNP	In vitro photothermal killing; preliminary healthy-mouse PK	Half-life 1.98 h, AUC 769 μg·h/mL for ICG-tracked formulation	24 h mortality-based MTD only
Dongsheng Li et al., 2023 A-PFH/C-MNPs	AGS gastric-cancer cells; no animal model	Sample size: N/A; dose and route: N/A, no in vivo study	Cisplatin, PFH, photothermal treatment	Cisplatin and selected nanoparticle controls; no matched albumin-free carrier	In vitro chemo-photothermal cytotoxicity and apoptosis-related findings	Not evaluated	No normal-cell or systemic toxicity assessment

(*continued on next page*)

Table 3 (*continued*)

Study and formulation	Application and experimental model	In vivo sample size, dose, and administration route	Payload or modality	Albumin-relevant comparator or control	Principal reported outcome	Pharmacokinetic assessment	Safety or toxicity assessment
Ayatollahi et al., 2022 ZnO-BSA-DG-FA	Ntera-2 cancer cells and HFF fibroblasts; no animal model	Sample size: N/A; dose and route: N/A, no in vivo study	Diosgenin and folate	Component comparisons were incomplete; no matched albumin-free or folate-free final carrier	In vitro cytotoxicity, apoptosis, cell-cycle, and gene-expression findings	Not evaluated	HFF viability only; no systemic toxicity assessment
Li et al., 2021 BLDH/5FU-ABX	HCT-116 cells and HCT-116 xenografts in female BALB/c nude mice	n = 6/group; three intravenous tail injections on days 0, 4, and 8; 5FU 3 mg/kg and Abraxane 20 mg/kg, equivalent to paclitaxel 2 mg/kg, per injection	5FU and albumin-bound paclitaxel	BLDH/5FU and BLDH/ABX single-drug controls; no matched albumin-free dual-drug LDH	Synergistic cellular activity and strongest tumor-growth inhibition with the dual formulation	No full plasma PK; tumor accumulation was examined	Body weight and major-organ histology; no major treatment-associated signal reported
Kim et al., 2021 BSA-silver NPs	B16F10 melanoma cells and HUVEC; no animal model	Sample size: N/A; dose and route: N/A, no in vivo study	Silver-mediated cytotoxicity and 690 nm photothermal treatment	Silver ions, PBS, and laser-only controls; no matched uncoated silver NP	ROS-associated melanoma-cell killing, antiangiogenic cell responses, and photothermal killing in vitro	Not evaluated	HUVEC assays only; no normal-tissue or systemic toxicity assessment
Zareian Baghdadabad et al., 2026 AgNPs-Alb	PC3 and LNCaP prostate-cancer cells; no animal model	Sample size: N/A; dose and route: N/A, no in vivo study; cell experiments generally triplicate	Silver nanoparticle cytotoxicity	Matched AgNP comparator and bicalutamide; no normal-cell control	Lower IC50, reduced migration and colony formation, and altered apoptosis-related endpoints relative to AgNPs	Not evaluated	No normal-cell, hemolysis, or systemic toxicity assessment
Hashemi et al., 2025 MnFe2O4@BSA-quercetin	4T1 mammary-carcinoma cells; healthy female BALB/c mice	n = 4/dose; 25, 50, 100, or 150 mg/kg intravenous; survival monitored for three weeks	Quercetin and 4 Gy irradiation in vitro	Free quercetin and carrier controls; no matched albumin-free MnFe2O4-quercetin formulation	pH-dependent release and enhanced in vitro cytotoxicity with irradiation; no tumor efficacy study	Not evaluated	Hemolysis below 5% to the highest tested concentration; survival, body weight, and blood panels in healthy mice
Olivieri et al., 2024 native-, cationic-, or anionic-BSA-coated fluorescent silica NPs	CHO-K1, GAG-deficient pgsA-745, and HeLa cells; no animal model	Sample size: N/A; dose and route: N/A, no in vivo study; paclitaxel cytotoxicity was based on three independent measurements	Fluorescent uptake probe and paclitaxel	Matched albumin-charge variants, bare silica NPs, GAG-deficient cells, enzymatic GAG cleavage, soluble heparin competitors, and uptake inhibition	Heparan sulfate supported uptake of native- and especially cationic-BSA interfaces; paclitaxel IC50 was 51 pM for cationic versus 192 pM for native BSA particles	Not evaluated	Carrier controls showed no significant cytotoxicity; no animal or systemic safety assessment
Zhao et al., 2021 AuNR@BSA	4T1 breast-cancer cells and subcutaneous 4T1 tumors in BALB/c mice	Efficacy: n = 2/group, intratumoral injection followed by 1064 nm irradiation at 0.75 W/cm2 for 10 min; separate PK/biodistribution: 200 μL intravenous, sample size not reported	NIR-II photothermal therapy	AuNR@BSA, AuNR@BSA plus laser, laser-only, and blank groups; CTAB-coated rods were compared in vitro, but no matched albumin-free photothermal formulation was tested	AuNR@BSA plus laser suppressed 4T1 tumor growth over 14 days; the result is formulation-level and preliminary	Approximately 1.5 h blood half-life; predominant liver and spleen accumulation at 24 h	Body weight was monitored; comprehensive systemic toxicology was not reported

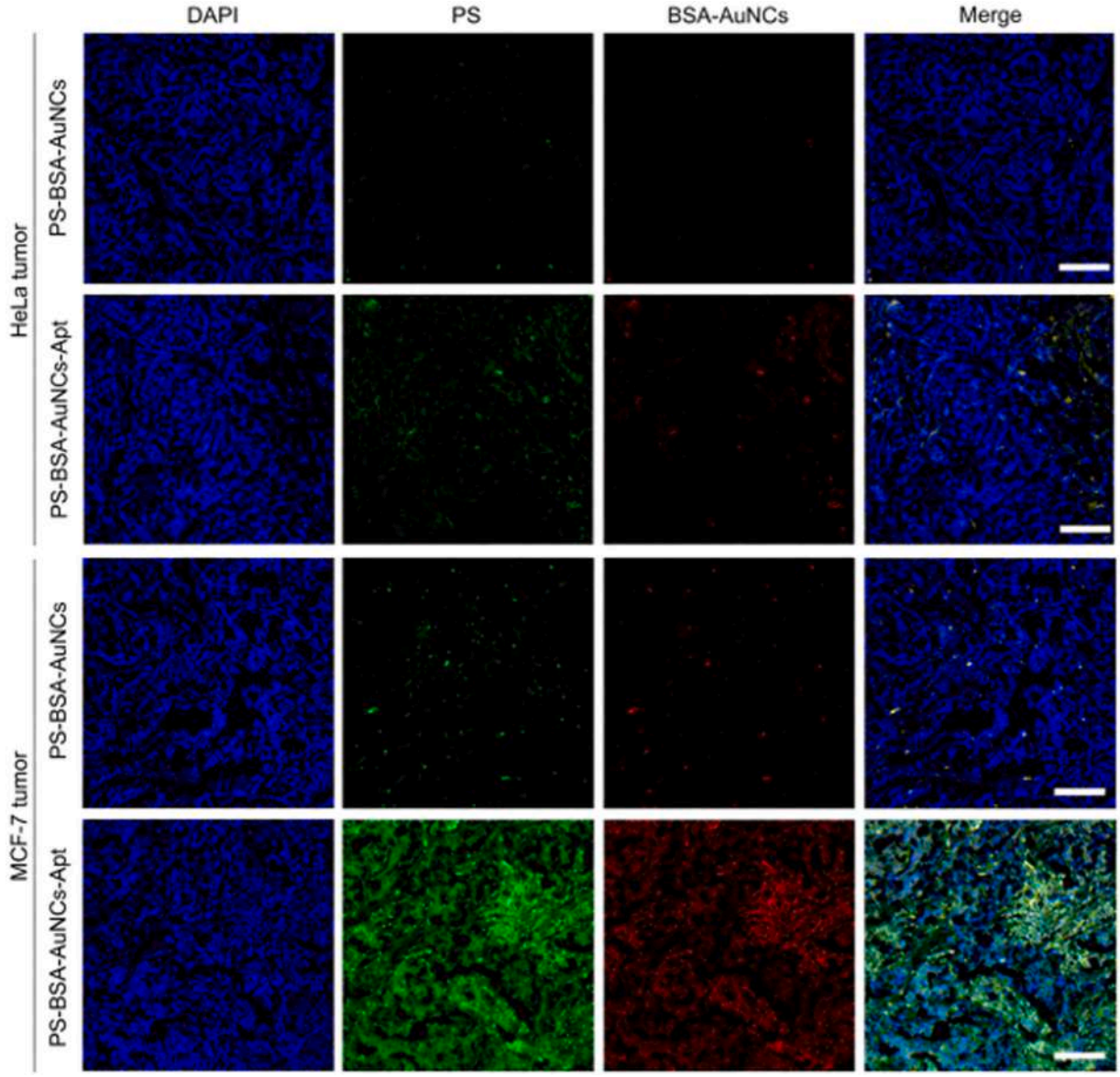

Fig. 2. Representative fluorescence micrographs of xenografted HeLa cervical-cancer and MCF-7 breast-cancer tissue sections incubated ex vivo with PS-BSA-AuNCs or EpCAM-aptamer-functionalized PS-BSA-AuNCs-Apt. DAPI (blue) stains nuclei-6,4′, PS-associated fluorescence is shown in green, BSA-AuNC fluorescence is shown in red, and merged images show signal colocalization. From top to bottom, the four groups are HeLa tumor + PS-BSA-AuNCs, HeLa tumor + PS-BSA-AuNCs-Apt, MCF-7 tumor + PS-BSA-AuNCs, and MCF-7 tumor + PS-BSA-AuNCs-Apt. Scale bars = 100 μm.

permeability coefficient (Papp) of $5.5 \pm 0.7 \times 10^{-7}$ cm/s and $82 \pm 3\%$ recovery. This demonstrates in vitro epithelial-monolayer transport, not oral absorption or in vivo barrier crossing. No animal imaging, pharmacokinetic, biodistribution, or efficacy study was performed.

3.5. Photodynamic and photoacoustic theranostics

Bychkova et al. extended the HSA-coated iron-oxide nanoparticle (IONP) platform by conjugating folic acid (FA) to the HSA interface and noncovalently loading methylene blue (MB) [19]. The HSA layer increased the particle diameter from approximately 33 ± 2–54 ± 6 nm, with 107 ± 32 μg of protein per milligram of iron oxide retained after the multistep folate-modification procedure. Less than 6% of fluorescently labelled HSA desorbed during challenge with additional HSA or immunoglobulin G (IgG), while electron magnetic resonance measurements indicated that the coating limited direct contact between IgG and the iron-oxide surface. These experiments directly support the formation of a comparatively persistent HSA interface under the tested buffer conditions, although they do not establish coating retention in serum or in vivo.

HSA also provided a binding environment for MB, yielding 5.8 ± 0.6 μg of photosensitizer per milligram of iron oxide, as well as a surface for folate presentation. The folate component was primarily responsible for receptor-sensitive delivery. Specifically, FA-modified particles produced approximately twofold greater uptake after 3 h in folate-receptor-rich MDA-MB-231 cells than matched non-FA HSA-coated particles (Fig. 4B). Excess free folate reduced this advantage. Upon irradiation, MB/FA-HSA@IONPs produced greater killing of MDA-MB-231 cells than free MB or MB-HSA@IONPs, whereas no comparable advantage was observed in low-receptor MCF-7 cells. Thus, albumin functioned as the stabilizing, photosensitizer-binding, and ligand-bearing interface, while the enhanced cellular uptake and photodynamic response were attributable primarily to folate within the composite interface. The study remained entirely in vitro, and neither magnetic resonance (MR) imaging nor another diagnostic modality was experimentally evaluated.

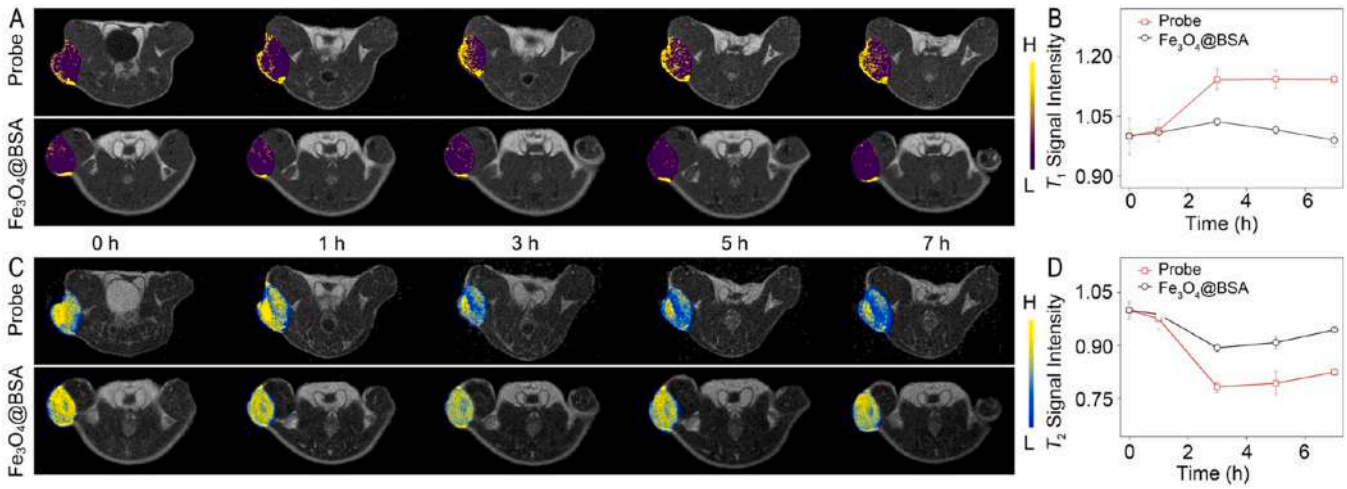

Fig. 3. In vivo T_1/T_2 magnetic resonance imaging performance of the Fe_3O_4@BSA-TA-Fe^{3+} platform. (A) Serial T_1-weighted images and (B) corresponding relative T_1 signal-intensity changes in 4T1 tumor-bearing mice after administration of Fe_3O_4@BSA-TA-Fe^{3+} (Probe) or Fe_3O_4@BSA. (C) Serial T_2-weighted images and (D) corresponding relative T_2 signal-intensity changes. The comparison demonstrates formulation-level dual-contrast MRI behavior and does not independently isolate an albumin-specific imaging or targeting effect.

Carrese et al. provided more direct in vitro photoacoustic-theranostic evidence by evaluating the same DOX-loaded, HSA-modified silica-melanin-silver platform for imaging and combined chemo-photothermal treatment in HS578T breast-cancer spheroids [20]. Relative to a matched bare-particle control, HSA coating increased mean spheroid-associated fluorescence from 6.716 to 26.320 arbitrary units after 18 h, whereas HSA-coated particles produced only 2.991 arbitrary units in non-malignant MCF10A spheroids (Fig. 4C). This approximately 3.9-fold increase relative to the bare-particle control directly supports a coating-associated increase in tumor-spheroid association and penetration. However, the proposed secreted protein acidic and rich in cysteine (SPARC)-mediated mechanism was inferred from the cellular phenotypes and prior evidence rather than tested through receptor blocking or knockdown.

DOX-loaded particles progressively entered HS578T spheroids, with prominent nuclear drug localization after 24 h. Following irradiation at 808 nm and 3 W/cm^2 for 5 min, the combined formulation reduced spheroid viability by approximately 80%, 86%, and 90% at DOX concentrations of 1.3, 2.6, and 5.2 μM, respectively, 24 h after irradiation. However, unloaded HSA-coated particles also produced substantial photothermal cytotoxicity, confirming that heating arose primarily from the melanin-silver core rather than albumin. Photoacoustic imaging of the treated spheroids yielded concentration-dependent signals consistent with melanin absorption, with reported contrast-to-noise ratios (CNRs) of 12–35 and signal-to-noise ratios (SNRs) of 13–36. HSA therefore contributed the exposed biological interface, enhanced spheroid penetration, and DOX carriage, whereas the melanin-silver core generated the photoacoustic and photothermal functions. The polydispersity index (PDI) of 0.45 indicated a heterogeneous particle distribution. This heterogeneity, together with the lack of animal imaging, pharmacokinetic, biodistribution, serum-corona, or in vivo efficacy studies, limits the translation of this otherwise integrated in vitro theranostic demonstration.

The two studies support different levels of theranostic integration. Bychkova et al. [19] demonstrated a comparatively persistent HSA interface under buffer conditions that bound MB and displayed folate, enabling folate-dependent uptake and photodynamic killing in breast-cancer cells. Because diagnostic imaging was not experimentally evaluated, this system is more accurately described as a photodynamic delivery platform with proposed magnetic theranostic potential. Carrese et al. [20] directly combined photoacoustic imaging and chemo-photothermal treatment using the same formulation in a three-dimensional tumor model. Across the two platforms, albumin acted mainly as a stabilizing, cargo-binding, and ligand-bearing biological interface, while folate drove receptor-sensitive targeting in the Bychkova system and the melanin-silver core generated imaging contrast and heat in the Carrese platform. Neither study demonstrated systemic delivery, secondary-corona behavior, pharmacokinetics, or combined imaging and therapeutic efficacy in vivo.

3.6. Radio-photothermal and chemoradiation platforms

Ghosh et al. synthesized ReOx cores directly in an HSA-containing aqueous medium, producing HSA-coated particles with a hydrodynamic diameter of 15.6 ± 0.8 nm and an HSA content of approximately 50% by weight. HSA formed the outer stabilizing interface, enabling a small water-dispersible formulation whose hydrodynamic size remained essentially unchanged for 7 days. Following intrinsic radiolabeling, [188Re]ReOx-HSA retained 91.4 ± 0.3% radiochemical stability in mouse serum at 48 h (n = 3) [21]. However, this radiochemical endpoint does not directly establish retention of the HSA interface, preservation of particle integrity in vivo, or resistance to secondary-corona formation. Circular dichroism also indicated loss of HSA alpha-helical content after coating. Because no uncoated ReOx comparator was tested, the observed formulation stability cannot be assigned specifically to albumin.

The diagnostic and therapeutic functions arose principally from the rhenium components: high-atomic-number Re supplied CT attenuation, 188Re generated the SPECT signal and β-radiotherapy, and ReOx converted 808 nm light into heat. In B16F10 cells, photothermal therapy and radiotherapy alone killed 30 ± 3% and 37 ± 3% of cells, respectively, whereas the combined treatment killed 87 ± 2% (n = 3), supporting a synergistic formulation-level response.

Following intratumoral administration in B16F10 melanoma-bearing mice, CT and SPECT/CT visualized the tumor, SPECT signal remained detectable through 48 h, and autoradiography showed broad intratumoral distribution. Tumor-associated activity reached 459.4 ± 23.4% of the injected dose per gram of tumor (%ID/g) at 1 h and remained detectable at 72 h. However, this high value reflects direct intratumoral administration and normalization to tumor mass, rather than systemic or albumin-mediated targeting. The optimized combined regimen arrested tumor growth during the observation period without significant body-weight changes or major abnormalities in the measured blood parameters and examined organ histology. Thus, the study demonstrates a locally administered, SPECT/CT-guided radio-photothermal platform, but the efficacy belongs to the complete ReOx-188Re-laser

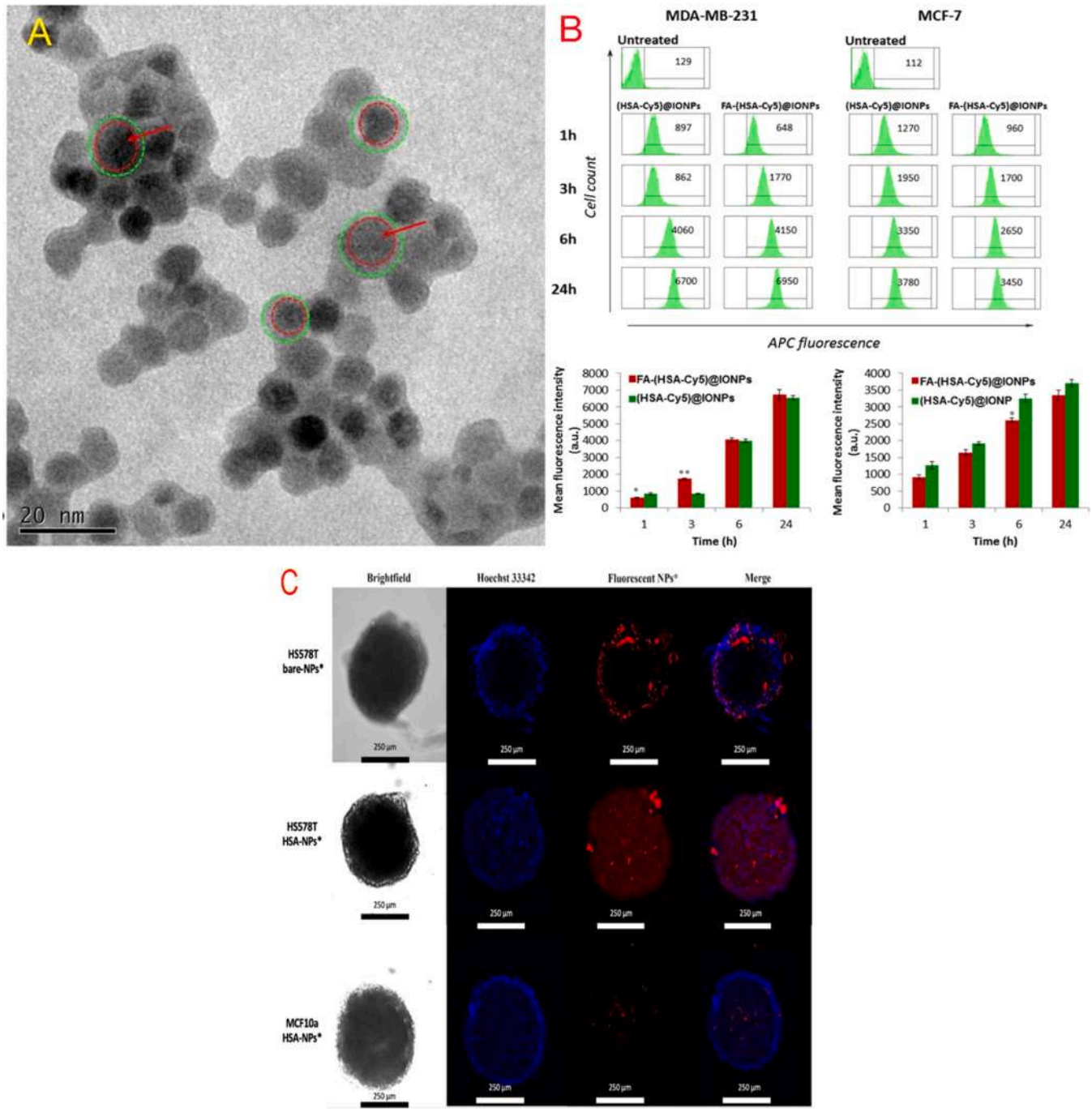

Fig. 4. Representative structural and cellular evidence from albumin-engineered diagnostic and/or therapeutic platforms. (A) TEM image of BSA-coated zinc-ferrite nanoparticles (MNP@BSA); red dashed circles mark the inorganic cores, green dashed circles the protein shell, and red arrows indicate lattice fringes. Scale bar = 20 nm. (B) Time-dependent uptake of (HSA-Cy5)@IONPs and FA-(HSA-Cy5)@IONPs in MDA-MB-231 and MCF-7 cells. At 3 h, folate-functionalized particles produced an approximately twofold higher fluorescence signal in MDA-MB-231 cells, whereas no corresponding advantage was observed in MCF-7 cells. (C) Fluorescence microscopy of HS578T spheroids treated for 18 h with bare or HSA-functionalized silica-melanin-silver nanoparticles and MCF10A spheroids treated with HSA-functionalized particles. Nuclei are shown in blue and fluorescent nanoparticles in red; scale bars = 250 µm.

system. Albumin-specific targeting, retention, or therapeutic benefit remains unproven because no matched HSA-free formulation, systemic administration, plasma pharmacokinetic analysis, or long-term survival assessment was included.

Nosrati et al. developed a chemoradiation platform based on a BSA-coated Fe3O4-Au heterodimer, designated F-Au, with methotrexate (MTX) covalently coupled to BSA by EDC/NHS chemistry and curcumin (CUR) retained through hydrophobic interactions and hydrogen bonding [22]. The clearest directly demonstrated albumin contribution was interfacial stabilization: uncoated Fe3O4-Au rapidly precipitated in PBS, whereas BSA enabled dispersion under the tested buffer conditions and supplied functional groups for drug attachment. Dynamic light scattering (DLS) measurements and zeta potential remained essentially unchanged for 14 days, demonstrating storage stability of the manufactured formulation in buffer, but not stability in blood or resistance to secondary-corona formation.

The reported MTX and CUR loadings were 3.0% and 6.12%, respectively. CUR release was faster at pH 5 than at pH 7.4, while only

16% of covalently linked MTX was released within 72 h without proteinase K, compared with 69% in its presence. These results support protease-sensitive release from the composite BSA-drug interface rather than an independent therapeutic effect of albumin. In 4T1 cells, X-ray cytotoxicity increased with the F-Au radiosensitizer dose, and MTX-bearing particles showed greater uptake than F-Au-BSA, indicating that the targeting advantage arose mainly from MTX rather than BSA. In 4T1-bearing mice, the complete F-Au-BSA-MTX-CUR formulation combined with 2 Gy irradiation produced the earliest and strongest reported tumor regression, whereas F-Au-BSA and F-Au-BSA-MTX without irradiation did not significantly suppress tumor growth. Four of five mice receiving F-Au-BSA-MTX plus 2 Gy died, whereas no mortality was reported in the corresponding CUR-containing irradiation groups. This finding is consistent with a formulation-associated radioprotective contribution from CUR, but the small groups preclude a definitive conclusion. No major organ damage was identified histologically in the selected treatment groups. The study therefore demonstrates systemic chemoradiation efficacy of the complete drug-loaded nanoradiosensitizer, but not albumin-specific tumor targeting, prolonged circulation, radiosensitization, or imaging. No matched BSA-free nanohybrid, pharmacokinetic or biodistribution analysis, or diagnostic imaging experiment was included.

Ghosh et al. therefore represent a locally administered radiophotothermal theranostic platform, because the same platform supported CT and SPECT/CT localization and combined radiotherapy-photothermal treatment. Nosrati et al. instead represent a systemically administered chemoradiation platform without demonstrated diagnostic imaging. HSA stabilized the small radiolabeled ReOx formulation in the former study, whereas BSA stabilized the otherwise PBS-unstable F-Au heterodimer and provided a scaffold for MTX conjugation and CUR loading in the latter. Nevertheless, the imaging and energy-conversion functions in Ghosh arose from Re and 188Re, while the radiosensitizing and cytotoxic effects in Nosrati depended on F-Au, MTX, CUR, and X-ray irradiation. Neither study included a matched albumin-free in vivo control, leaving the incremental therapeutic benefit of albumin unresolved.

3.7. Theranostic integration: evidence strength and translational gaps

The platforms reviewed in this section represent distinct levels of theranostic evidence. Zhang et al. provided the most complete integration, combining systemic administration, in vivo T1- and T2-weighted MRI, and ferroptosis-associated photothermal therapy in the same tumor-bearing mouse model. Ghosh et al. also demonstrated in vivo integration by combining CT and SPECT/CT visualization with radiophotothermal treatment. However, the intratumoral administration used in that study establishes local image-guided treatment rather than systemic theranostic delivery. Carrese et al. directly combined photoacoustic imaging with chemo-photothermal therapy in three-dimensional tumor spheroids, providing formulation-level theranostic integration without in vivo validation.

The remaining studies demonstrated only partial theranostic components. Caputo et al. combined MRI relaxometry with cisplatin delivery and barrier-model transport, but did not perform in vivo imaging or therapeutic evaluation. Bychkova et al. [19] demonstrated folate-dependent photodynamic activity without evaluating a diagnostic imaging modality. Petrov et al. reported an MRI-compatible relaxometric profile rather than experimental image acquisition, while Suwannasing et al. demonstrated in vitro radiosensitization without a diagnostic component. Nosrati et al. demonstrated systemically administered chemoradiation in tumor-bearing animals, but no imaging modality was evaluated. This hierarchy distinguishes contrast-generating potential from experimentally demonstrated imaging and distinguishes therapeutic activity from integration of imaging and therapy within the same formulation and experimental model.

Across these platforms, albumin primarily enabled colloidal stabilization, cargo binding, biomineralization, or ligand presentation, whereas imaging signals and therapeutic activity were generated mainly by the inorganic cores, radionuclides, loaded drugs, or externally applied energy. Even the most integrated studies therefore demonstrate theranostic performance of the complete formulation rather than an independent albumin-specific theranostic advantage. None evaluated a matched albumin-free final platform across both the imaging and therapeutic components of the system. Future theranostic studies should compare the complete platform with matched albumin-free controls and, where applicable, controls separating albumin from additional targeting ligands or hybrid-interface components. These comparisons should be integrated with systemic administration, serial imaging and therapeutic evaluation in the same model, quantitative pharmacokinetic and biodistribution analyses, and direct assessment of engineered-albumin retention and secondary-corona formation. Longer-term recurrence, survival, and systemic-safety endpoints will also be required to determine whether albumin provides a reproducible translational advantage within multifunctional theranostic platforms.

4. Biological identity, secondary corona, and stealth

Beyond their diagnostic and therapeutic functions, engineered albumin interfaces may modify nanoparticle biological identity at the nano-bio interface. Four studies examined complementary aspects of this process, including detectable secondary-corona formation, corona-associated macrophage interactions, electric-field-induced reorganization of preformed albumin layers, and charge-dependent interactions with the cellular glycocalyx. Collectively, these findings suggest that stealth-related behavior may depend on the architecture and composition of albumin-containing interfaces, as well as on the amount and identity of subsequently adsorbed proteins. However, they do not establish a universal mechanism applicable across different albumin configurations and nanoparticle cores.

4.1. Apparent resistance to detectable secondary-corona formation

Traverso et al. developed CdSe/ZnS quantum dots (QDs) passivated with a crosslinked, partly denatured HSA multilayer and externally decorated with HSA or human transferrin (hTf) [23]. The resulting particles remained water-dispersible and fluorescent. Electrophoretic analysis supported external protein decoration, while alkaline-phosphatase activity and cellular-uptake experiments indicated that representative surface-displayed proteins retained biological functionality. Secondary-corona formation was evaluated only for hTf-QDs after 30 min of exposure to 50% FBS. Their mean hydrodynamic diameter was 21.46 $\pm$ 1.88 nm in PBS and 19.71 $\pm$ 1.73 nm in serum-containing medium. The absence of an increase in mean hydrodynamic diameter indicates no detectable DLS enlargement under the tested conditions, but does not demonstrate complete resistance to additional protein adsorption. DLS may fail to detect thin or incomplete protein layers, compositionally selective adsorption, protein exchange without a substantial size change, or low-abundance particle subpopulations. Confirmation would require orthogonal quantitative adsorption and surface-composition measurements, such as labeled-protein adsorption assays, electrophoretic or liquid chromatography-tandem mass spectrometry (LC-MS/MS) analysis, isothermal titration calorimetry, quartz crystal microbalance, or surface plasmon resonance.

The hTf-QDs also showed temperature-dependent uptake in A549 cells. At 37 °C, the mean uptake difference between hTf-QDs and HSA-QDs was 8.2 particles per cell, compared with 0.46 particles per cell at 4 °C. This result supports active uptake driven primarily by the exposed hTf rather than an independent HSA-targeting effect. Digitoxin-loaded hTf-QDs also selectively reduced A549 cell numbers, supporting functional cargo delivery by the complete construct. HSA therefore acted mainly as the water-solubilizing, stabilizing, and protein-bearing scaffold, whereas hTf supplied the demonstrated targeting function.

Following subconjunctival administration, fluorescence was

detected across several murine retinal layers in non-perfused sections, but after PBS perfusion, confirmed intracellular uptake was limited to retinal pigment epithelial cells. The findings therefore indicate retinal distribution rather than cellular internalization throughout the outer nuclear layer. They also do not establish that the engineered HSA interface remained unchanged in vivo. Major limitations include the short serum-incubation period, absence of quantitative protein-adsorption or proteomic analysis, local rather than systemic administration, a single 24 h observation point, three mice per group, and absence of tumor-bearing animals, formal pharmacokinetics, systemic biodistribution, toxicity assessment, or in vivo corona recovery. Potential cadmium release from the CdSe/ZnS core was also not comprehensively evaluated.

4.2. Proteomic dissection of corona-mediated stealth

Bozzer et al. provided detailed LC-MS/MS characterization of the secondary protein corona formed on poly(lactic-co-glycolic acid)-poly (vinyl alcohol) (PLGA-PVA) nanoparticles containing a covalently immobilized HSA surface layer [24]. Following incubation in normal human serum for 1 h and three washing steps, 105 protein species were identified on NP-HSA, compared with 79 on uncoated nanoparticles. These values describe the number of identified protein species rather than the total mass of adsorbed protein. The principal observed effect was therefore a change in corona diversity and relative composition, rather than a demonstrated reduction in total protein adsorption. The NP-HSA corona showed greater relative representation of albumin, apolipoproteins A-I, A-II, and C-III, and clusterin, while terminal complement components C5–C9 were not detected.

The absence of C5–C9 is potentially relevant because these proteins participate in terminal complement activation and membrane-attack-complex formation. However, their absence cannot be described as complete complement blockade or as the critical molecular event responsible for stealth. C3 and C4, immunoglobulins, fibrinogen, coagulation-associated proteins, other opsonins, and multiple phagocytic pathways may also influence nanoparticle recognition and clearance.

Macrophage internalization decreased from approximately 35% for uncoated nanoparticles to approximately 20% for NP-HSA, with $p \leq 0.01$ (Fig. 5A). This matched comparison supports an HSA-interface-associated reduction in macrophage interaction after serum exposure. However, HSA coating did not significantly alter lymphocyte interaction, coagulation behavior, or the measured residual activity of the classical complement pathway relative to uncoated nanoparticles. Its immune-modulating effect was therefore selective rather than a general suppression of blood and immune interactions. The study demonstrated an association between altered corona composition and reduced macrophage uptake, but did not establish a direct causal role for any individual enriched or depleted protein. Protein-depletion, complement-reconstitution, receptor-blocking, and genetic-perturbation experiments were not performed.

In zebrafish xenografts, t-NP-HSA produced approximately threefold greater colocalization with NALM-6 cells than untargeted NP-HSA, approximately 15% versus 5% (Fig. 5B). At 24 h, more than 60% of both NP-HSA and t-NP-HSA remained non-internalized in the bloodstream compartment, and fewer than 25% were associated with macrophages, without significant differences between the targeted and untargeted formulations. The 24-h result therefore represents a single-time-point distribution measurement rather than a formal pharmacokinetic demonstration of prolonged circulation. After doxorubicin loading, doxo-t-NP reduced NALM-6 fluorescence and increased survival relative to saline during the three-day observation period, although survival was similar to that with free doxorubicin. The matched comparisons associate HSA with reduced macrophage internalization, anti-CD19 with enhanced interaction with CD19-positive tumor cells, and doxorubicin with therapeutic activity. HSA and anti-CD19 were both covalently attached to the nanoparticle surface, rather than anti-CD19 being conjugated through HSA. The targeting, distribution, and therapeutic findings therefore belong to the complete formulation and cannot be attributed exclusively to HSA or to the non-detection of C5 to C9. Translation is limited by the zebrafish-embryo xenograft model, three-day follow-up, and absence of mammalian pharmacokinetic, organ-level biodistribution, long-term efficacy, and systemic-safety evaluation.

4.3. Electric-field modulation of a preformed BSA interface

Kumar et al. used direct-current electric fields to modulate a preformed BSA interface on approximately 24 nm gold nanoparticles (GNPs) [25]. Electric-field treatment was applied for 3 min to preformed BSA-GNP conjugates in the presence of unbound BSA. At 15 μM total BSA, the apparent hydrodynamic size increased from 32.9 nm at 0 V to 148.2 nm at 30 V, with intermediate increases at 5 and 15 V. The authors interpreted this as additional BSA adsorption and multilayer-corona formation. However, surface-bound BSA and the multilayer architecture were not independently measured, and DLS cannot distinguish additional adsorption from particle or protein aggregation. The smaller field-dependent size increases of BSA-GNP conjugates than free BSA support reduced, rather than absent, aggregation or conformational reorganization. The apparent association constant for curcumin binding to BSA-GNP was $1.403 \times 10^5\ M^{-1}$ without field treatment, compared with 0.942 and $1.137 \times 10^5\ M^{-1}$ at 5 and 15 V and $0.6818 \times 10^5\ M^{-1}$ at 30 V. Thus, the field-treated values did not exceed the untreated value, supporting retained spectroscopic binding rather than increased affinity. The formulations showed low hemolytic activity, but the assay used erythrocytes from a single healthy donor and does not establish broader biocompatibility. No serum-corona, cancer-cell, or in vivo studies were performed. The study therefore supports electric-field-dependent changes in apparent size and spectroscopic curcumin binding, but not a defined multilayer architecture, stealth, increased drug loading, controlled release, targeted delivery, or therapeutic efficacy.

4.4. Glycocalyx-dependent uptake of modified albumin interfaces

Olivieri et al. coated 50 nm fluorescent silica nanoparticles with native, cationic, or anionic BSA [26]. Native and cationic BSA, but not anionic BSA, bound heparin, while glycosaminoglycan (GAG)-deficient cells, enzymatic cleavage, competition, and inhibition implicated heparan sulfate in uptake. The HeLa-cell perturbation experiments further showed that enzymatic glycocalyx modification and excess heparin altered uptake of the native- and cationic-BSA-coated nanoparticles (Fig. 5C). GAG deficiency reduced CHO-cell uptake 1.7-fold for native-BSA-coated particles and 30-fold for cationic-BSA-coated particles; cationic-BSA particles also showed approximately tenfold greater HeLa-cell uptake than native-BSA particles. Paclitaxel-loaded cationic- and native-BSA particles yielded particle-based IC50 values of 51 and 192 pM, respectively, although drug content was estimated rather than directly quantified for each formulation. These matched experiments support charge- and GAG-dependent uptake under static in vitro conditions, but partial denaturation of anionic BSA complicates attribution of its behavior solely to charge. The mechanism was not tested under blood flow or in vivo; serum reduced native-BSA, but not cationic-BSA, uptake.

4.5. Stealth reconsidered: mechanistic hypotheses for charge-function decoupling

The available studies challenge a simple model in which nanoparticle stealth depends only on minimizing total protein adsorption. Traverso et al. found no detectable DLS enlargement after short exposure of HSA-passivated quantum dots to 50% FBS, whereas Bozzer et al. identified more protein species on HSA-coated than uncoated nanoparticles alongside lower macrophage internalization. Kumar et al. and

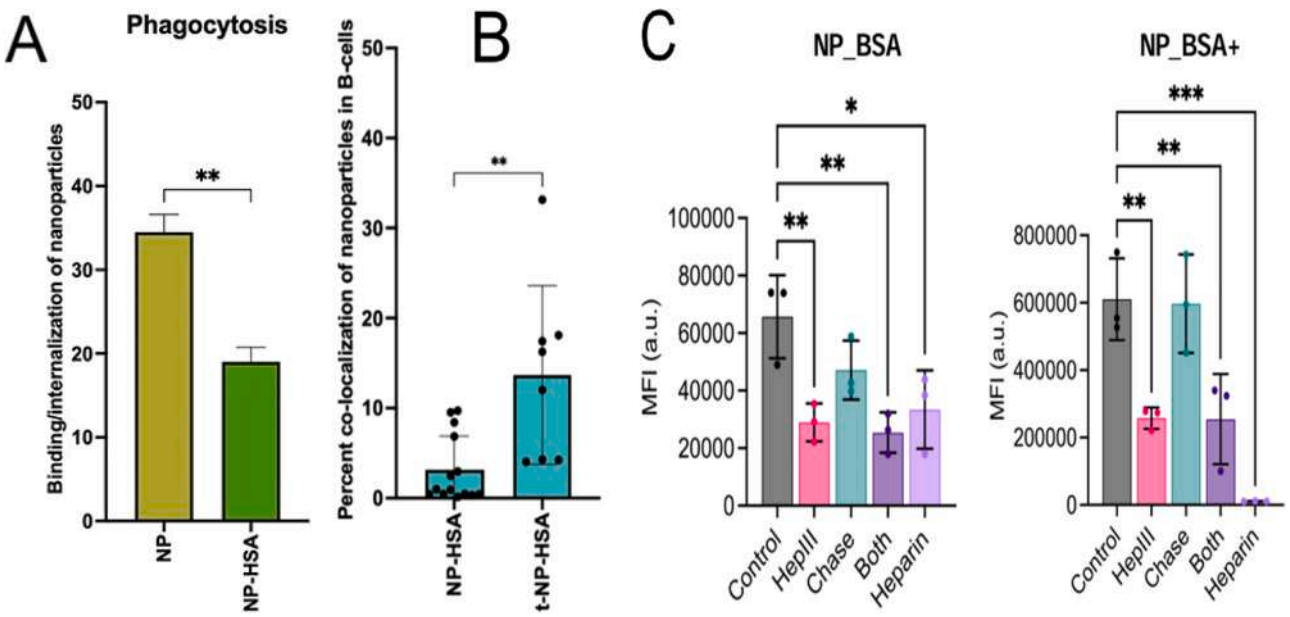

Fig. 5. Representative cellular-interaction outcomes of engineered albumin-containing nanoparticle interfaces. (A) Phagocytic binding/internalization of uncoated nanoparticles (NP) and HSA-coated nanoparticles (NP-HSA) after incubation in the presence of normal human serum, showing reduced phagocytic interaction with NP-HSA. (B) Tumor-B-cell interaction of untargeted NP-HSA and anti-CD19-targeted t-NP-HSA in the zebrafish xenograft model, illustrating the additional targeting effect associated with anti-CD19 functionalization. (C) Uptake of native-BSA-coated (NP_BSA) and cationic-BSA-coated (NP_BSA+) silica nanoparticles by HeLa cells following glycocalyx-modifying enzyme treatment or competition with excess heparin, illustrating heparan-sulfate-associated modulation of cellular uptake.

Olivieri et al. [26] further showed that interface organization, albumin charge, and glycocalyx interactions can affect ligand binding or cellular uptake. Collectively, these findings support an architecture- and composition-dependent view of albumin-containing interfaces but do not establish a universal stealth mechanism.

Within this context, the proposed "Zeta Potential Paradox" should denote a hypothesis of charge-function decoupling, not evidence that positively charged albumin-containing interfaces evade immune recognition. Wu et al. composite cRGD-BSA precoating had a measured zeta potential of +23.43 mV while reducing total serum-protein adsorption and reshaping the ex vivo acquired corona, including depletion of complement factor D and lower representation of proteins associated with immunoglobulins, complement activation, coagulation, and acute-phase responses. This profile suggests a potentially less opsonizing biological identity, but complement activity, macrophage recognition, systemic clearance, and prolonged circulation were not measured. Leung et al. multicomponent RGD-streptavidin-dcBSA-PEG nanodiamonds likewise had a positive zeta potential (+12.10 mV), remained colloidally stable in protein-containing medium, and showed enhanced barrier-model transport and brain-tumor-associated fluorescence. However, the positive charge appeared after streptavidin-RGD assembly, whereas dcBSA-PEG nanodiamonds were negatively charged, and neither an acquired corona nor immune clearance was assessed. This study therefore shows that positive measured charge can coexist with delivery-related functionality, not stealth [27,28]. Several mechanisms could explain this apparent decoupling. Zeta potential is measured at the hydrodynamic shear plane and does not represent local charge domains, surface heterogeneity, or ligand accessibility. Albumin or PEG may screen underlying charge while leaving localized cationic domains or ligands accessible, whereas corona composition and macrophage recognition also depend on surface chemistry and protein presentation [29,30]. Albumin charge and interactions with cell-surface glycosaminoglycans, particularly heparan sulfate, can further regulate uptake [26], consistent with related charge-dependent nanoparticle studies [31]. Their relative contributions remain unresolved. Albumin cannot be assumed to confer stealth because its effects depend on conformation and presentation. Adsorption or denaturation can expose cryptic epitopes recognized by mononuclear-phagocyte scavenger receptors [32], a possibility relevant but untested for Leung et al.'s deliberately denatured and cationized BSA. Testing charge-function decoupling will require matched formulations varying albumin conformation, charge, PEG coverage, and ligand presentation, combined with corona proteomics, complement and macrophage assays, and mammalian pharmacokinetic and biodistribution studies. Whether the engineered interface remains relevant after secondary-corona formation and vascular-glycocalyx contact remains unresolved.

5. Cancer-specific controlled release strategies

The therapeutic relevance of an albumin surface or interface engineering strategy depends on its ability to deliver payloads with appropriate spatial and temporal control. This section evaluates 21 studies of albumin-engineered delivery across non-small-cell lung cancer, breast cancer, hepatocellular carcinoma, ovarian cancer, glioblastoma, colon cancer, skin cancer, and prostate cancer, together with healthy-animal safety studies, to compare tumor- and formulation-specific design principles.

5.1. Lung cancer

Li et al. coated amine-functionalized hydroxyapatite nanoparticles containing doxorubicin (HAP/DOX) with BSA for A549 non-small-cell lung cancer [33]. BSA coating increased the hydrodynamic diameter from 55.6 ± 2.3 to 68.4 ± 3.6 nm, decreased the PDI from 0.127 to 0.095, and reversed the zeta potential from +27.2 ± 3.3 to −25.1 ± 2.8 mV. The complete formulation showed an encapsulation efficiency of 90.31 ± 4.35% and a loading efficiency of 15.26 ± 1.87%, but corresponding HAP/DOX values were not reported, preventing isolation of the BSA contribution. At 120 h, cumulative DOX release was approximately 87% at pH 5.0 versus 28% at pH 7.4, supporting acid-responsive release (Fig. 6A). DOX loading into HAP was attributed to Ca^{2+}-DOX complexation, although acid-induced destabilization of this complex was not directly demonstrated. BSA/HAP/DOX produced 1.78-fold greater intracellular DOX accumulation in A549 cells than

HAP/DOX after 2 h, while excess free BSA selectively reduced this signal for BSA/HAP/DOX. These matched experiments support an incremental BSA-dependent cellular interaction. In vivo, BSA/HAP/indocyanine green (ICG) yielded 5.96-fold greater ex vivo tumor fluorescence than HAP/ICG and 0.66-fold liver fluorescence at 12 h. These relative fluorescence signals suggest altered distribution but do not quantify nanoparticle or drug concentrations. The blood half-life of BSA/HAP/DOX was approximately 6 h versus 15 min for free DOX. However, the absence of an HAP/DOX pharmacokinetic comparator prevents attribution of this prolongation specifically to BSA. Final tumor volumes were reduced to 323 ± 52 mm^3, compared with approximately 1400 mm^3 for saline controls, with HAP/DOX producing an intermediate response. Blank BSA/HAP maintained greater than 95% A549-cell viability at 150 μg/mL after 48 h, supporting low short-term carrier cytotoxicity only. Thus, the matched uptake, competition, and HAP/ICG comparisons support an incremental BSA contribution, whereas pharmacokinetic and absolute efficacy outcomes reflect the complete formulation. BSA surface coverage, retention or exchange during circulation, and secondary-corona formation in vivo were not assessed.

Goel et al. formed a drug-free $CoFe_2O_4$@BSA@Ag hybrid by adsorbing BSA onto polyvinylpyrrolidone (PVP)-stabilized $CoFe_2O_4$ and depositing silver. Relative to bare $CoFe_2O_4$, the final composite had a larger hydrodynamic diameter (176.2 versus 89 nm), a slightly lower but still high PDI (0.434 versus 0.470), and a more negative zeta potential (−16.8 versus −6.2 mV). Because the BSA-coated intermediate was not evaluated by DLS, these comparisons cannot separate BSA from silver effects; high polydispersity and partial aggregation also limit colloidal-stability claims. Serum stability and BSA retention were not assessed. In H1299 cells, the 48-h IC50 decreased from 58.8 μg/mL for CoFe2O4@BSA to 38.28 μg/mL for CoFe2O4@BSA@Ag, supporting an incremental silver-associated effect. The final composite reduced viable cells to 25.8%, produced approximately 67.3% apoptosis, and inhibited migration and colony formation. HEK-293 viability remained above 70% at higher tested concentrations, and hemolysis remained below 5% up to 100 μg/mL. Except for the comparative H1299 MTT assay, these outcomes were assessed only for the complete composite. All biological experiments were in vitro (n = 3), without animal pharmacokinetic, biodistribution, efficacy, or systemic toxicity studies [34].

The two studies differ in interface architecture, therapeutic mode, and evidence maturity. Li et al. used an adsorbed BSA layer to modify delivery of a defined DOX payload. Matched HAP/DOX and HAP/ICG controls plus free-BSA competition support an incremental BSA-associated effect on cellular interaction and relative fluorescence distribution; serum-stability, blood-persistence, and A549 xenograft studies added broader formulation-level evidence. Goel et al. instead used BSA as a coating and silver-deposition scaffold in a drug-free $CoFe_2O_4$ composite. Its stepwise MTT controls distinguish coating-associated and silver-associated changes, but the other anticancer and preliminary safety endpoints were measured only for the final composite, and all evidence remains in vitro. Li G. therefore provides

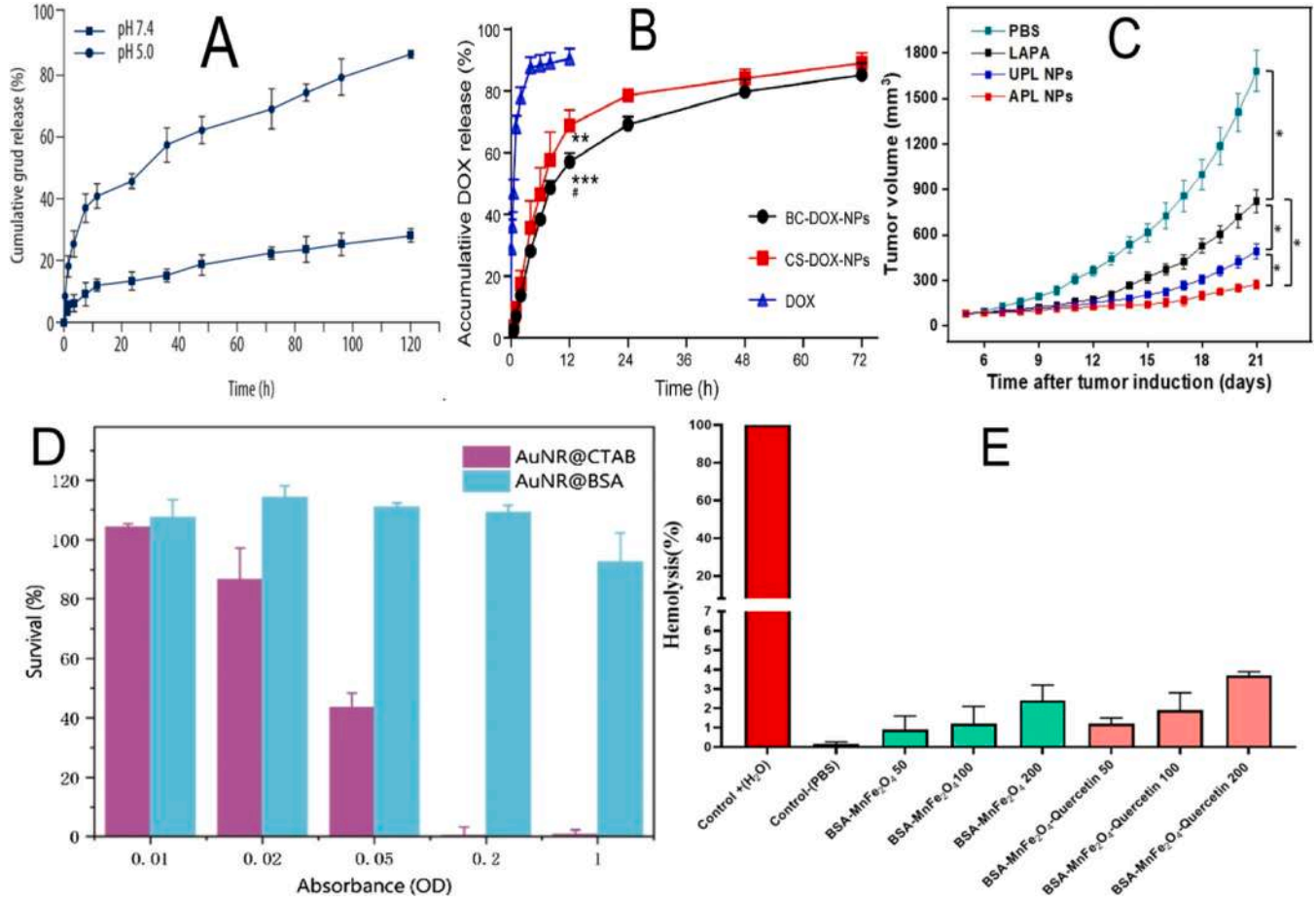

Fig. 6. Representative experimental outcomes across albumin-engineered lung- and breast-cancer nanoplatforms. (A) Cumulative doxorubicin release from BSA/HAP/DOX nanoparticles under acidic and physiological pH conditions, illustrating pH-dependent release of the complete formulation. (B) In vitro doxorubicin release from BSA-coated BC-DOX-NPs, matched BSA-free CS-DOX-NPs, and free DOX. (C) Tumor-growth curves in 4T1 tumor-bearing mice treated with PBS, free lapatinib, uncoated lapatinib-loaded PLGA nanoparticles (UPL NPs), or BSA-coated lapatinib-loaded nanoparticles (APL NPs). (D) Viability of 4T1 cells exposed to CTAB-rich or BSA-coated gold nanorods, illustrating the improved cellular compatibility associated with interface replacement. (E) Hemolysis measured for the $MnFe_2O_4$@BSA-quercetin formulation and relevant controls, providing preliminary hemocompatibility evidence.

stronger evidence for an albumin-associated delivery contribution, although its half-life advantage lacks an albumin-free nanoparticle comparator; Goel demonstrates physicochemical feasibility and formulation-level cytotoxicity without in vivo validation. Neither study assessed persistence, exchange, or secondary-corona masking of the pre-engineered BSA interface in biological media or circulation.

5.2. Breast cancer: targeted drug delivery and multimodal therapy

Tan et al. formed chondroitin sulfate (CS)-DOX nanoparticles (CS-DOX-NPs) by electrostatic self-assembly and then adsorbed BSA to produce albumin-corona nanoparticles (BC-DOX-NPs) [35]. The authors proposed complementary targeting through the albumin-associated 60-kDa glycoprotein (gp60) and SPARC pathways, together with cluster of differentiation 44 (CD44) recognition by CS. Compared with matched BSA-free CS-DOX-NPs, BSA adsorption increased the diameter from 99.71 to 105.16 nm, reduced the PDI from 0.188 to 0.173, shifted the zeta potential from −7.89 to −3.52 mV, and increased encapsulation efficiency from 80.7% to 85.1%. Drug-loading efficiency decreased from 9.34% to 5.42%, but the proposed mass-dilution explanation was not tested. BSA also improved stability in 50% FBS and reduced early DOX release from approximately 46% to 38% at 6 h; both formulations released approximately 90% by 72 h (Fig. 6B). In vivo, BC-DOX-NPs produced 2.7-fold greater tumor DOX accumulation at 4 h and lower liver drug concentration than CS-DOX-NPs. At day 18, tumor-volume reduction was 82.8% versus 62.0%, and median survival was 50 versus 43 days. The separately reported 91.4% inhibition value was derived from tumor weight and is not directly comparable with the volume-based reductions. These matched results support an incremental contribution from the BSA-containing interface, whereas the absolute outcomes remain those of the complete multicomponent formulation.

CS competition examined CD44 involvement, whereas gp60 and SPARC were not tested by receptor blocking or knockdown. Uptake remaining above that of BSA-free particles after CS competition suggests an additional BSA-associated pathway but does not identify its receptor. Stability was assessed for one week during storage and for 72 h in 50% FBS, without whole-blood testing or confirmation that the BSA interface persisted in vivo. Supplementary histology showed myocardial-fiber changes in the BSA-free, but not the BSA-coated, group; however, missing clinical chemistry, hematology, cardiac biomarkers, and long-term toxicity testing preclude firm systemic-safety conclusions.

Iqbal et al. provided a clearer coating-specific test by comparing BSA-coated lapatinib-loaded PLGA nanoparticles with a matched uncoated carrier [36]. The coated formulation showed pH-dependent release, with 62.54% of lapatinib released at pH 5.0 versus 30.26% at pH 7.4 over 48 h. Preincubation with free albumin reduced 4T1-cell uptake by 76.32%, indicating an albumin-sensitive uptake process without identifying a receptor. After a single intravenous 10 mg/kg lapatinib-equivalent dose in healthy mice, the coated particles had a 6.38 h plasma half-life, compared with 2.23 h for uncoated particles and 0.29 h for free drug (n = 5 per group). In 4T1 tumor-bearing mice, three intravenous 10 mg/kg doses increased tumor drug concentration relative to both controls and produced greater tumor-growth inhibition (Fig. 6C). These comparisons support a coating-associated delivery benefit, although gp60 and SPARC involvement and persistence of the manufactured BSA interface were not tested.

Carrese et al. [37] used recombinant HSA as the exposed drug-binding interface of a silica-melanin-silver hybrid. Doxorubicin loading produced MelaSil_Ag-HSA@DOX particles of 407 ± 29 nm, and fluorescence quenching indicated that HSA binding sites remained accessible after immobilization [37]. At 24 h, approximately 80% of DOX was released at pH 5.2 versus about 20% at pH 7.4, while 808 nm irradiation enhanced HS578T-cell killing. HSA therefore supplied the drug-binding and pH-responsive release compartment, whereas photothermal conversion arose from the melanin-containing core and irradiation. Because no matched HSA-free, DOX-loaded carrier was tested biologically, the chemo-photothermal outcome remains attributable to the complete formulation.

Carrese et al., discussed in Section 3.5, extended the same platform to three-dimensional HS578T breast-cancer and non-neoplastic MCF-10A spheroids [20]. HSA-functionalized particles showed greater uptake and deeper penetration than bare particles in HS578T spheroids, together with substantially lower interaction with MCF-10A spheroids. DOX delivered by the HSA-containing formulation showed time-dependent redistribution and prominent nuclear localization after 24 h. These findings associate HSA functionalization with enhanced interaction in the tumor-spheroid model, but SPARC involvement was not directly tested and no matched HSA-free, DOX-loaded formulation was evaluated. In vivo delivery, pharmacokinetics, biodistribution, and secondary-corona formation were not assessed.

Mahmoud et al. compared BSA adsorbed onto 3-mercapto-1-propanesulfonate (MPS)-modified gold nanorods (GNR-BSA) and citrate-stabilized gold nanospheres (GNS-BSA) at approximately pH 4 in MDA-MB-231 cells [38]. BSA increased the rod diameter from 98.1 ± 3.9 to 127.95 ± 2.2 nm after MPS replacement of the hexadecyltrimethylammonium bromide (CTAB)-rich precursor and shifted the zeta potential from −12.4 ± 4.9 to +11.1 ± 5.5 mV. For spheres, BSA increased the diameter from 64.1 ± 8.9 to 74.4 ± 3.8 nm and shifted the zeta potential from −22.3 ± 3.3 to +12.0 ± 3.5 mV. These changes support albumin-containing interfaces but do not exclude aggregation or protein conformational change. GNR-BSA had a reported IC50 of approximately 3.0 μg/mL and about 5% cellular internalization, whereas GNS-BSA showed less than 0.4% uptake and minimal cytotoxicity. GNR-BSA also delayed scratch closure at 24 h, while neither geometry substantially altered adhesion. Because the formulations differed in shape, size, chemistry, charge, and BSA coverage and lacked albumin-free controls, they demonstrate geometry-dependent formulation behavior rather than an isolated BSA effect. No serum-interface or animal study was performed.

Zhang et al. prepared predominantly zero-valent platinum nanocores within a BSA shell (Pt@BSA) [39]. Coextrusion with murine red-blood-cell membranes formed membrane-coated Pt@BSA (Pt@BSA-RM), increasing the hydrodynamic diameter from 8.6 ± 2.1 to 112.4 ± 3.4 nm. Thus, BSA was the synthesis-associated shell of the inner platinum core, whereas the membrane became the biologically exposed outer interface. The final assembly remained stable for 72 h in PBS, 10% FBS, and simulated body fluid and released platinum under 1 mM hydrogen peroxide, but no BSA-free platinum control was included. In 4T1 cells, Pt@BSA-RM plus X-ray irradiation generated more ROS and DNA damage than Pt@BSA plus irradiation. In subcutaneous 4T1 tumors, intratumoral Pt@BSA-RM at 2.5 mg/kg every 2 days plus four 5 Gy irradiations produced the greatest tumor suppression and less organ histopathology than Pt@BSA plus irradiation. These comparisons isolate an incremental benefit of the outer membrane, not albumin, and the intratumoral design does not establish systemic albumin-mediated targeting or prolonged circulation.

Zhao et al. reduced CTAB around gold nanorods and then incubated the rods with BSA under alkaline conditions to generate BSA-coated gold nanorods (AuNR@BSA) for second near-infrared-window (NIR-II) photothermal therapy [40]. Relative to the CTAB-rich precursor (AuNR@CTAB), BSA substitution reversed the zeta potential and retained absorption near 1064 nm. AuNR@BSA was substantially less cytotoxic to 4T1 cells than the CTAB-rich precursor (Fig. 6D), directly associating interface replacement with improved cellular compatibility, although residual CTAB was not quantified. Irradiation at 1064 nm and 0.75 W/cm^2 for 10 min reduced 4T1 survival to approximately 20%, but heat generation arose from the gold-nanorod-laser interaction. After intravenous administration, AuNR@BSA had an approximately 1.5 h blood half-life and predominant liver and spleen accumulation at 24 h, but no albumin-free in vivo comparator. Intratumoral treatment involved only two mice per group and therefore establishes local formulation-level photothermal efficacy, not systemic albumin-mediated tumor targeting.

Hashemi et al. adsorbed BSA onto preformed MnFe2O4

nanoparticles for 12 h, removed unbound protein by dialysis, and then loaded quercetin. The approximately 7 nm inorganic cores produced BSA-coated particles of 85.27 ± 0.26 nm with a PDI of 0.25. Quercetin loading increased the diameter to 98.13 ± 0.78 nm, with 27.5% loading efficiency. Molecular docking predicted quercetin binding to BSA, but loading was not compared with a matched albumin-free carrier. Quercetin release reached 62% at pH 5.7 and 41% at pH 7.4 after 120 h, demonstrating pH-dependent dialysis release, not tumor-selective release in vivo. In 4T1 cells, the complete formulation reduced viability relative to free quercetin, and 4 Gy irradiation further increased cytotoxicity; missing albumin-free and unloaded-core controls prevent separation of BSA, quercetin, manganese ferrite, and radiation effects. Hemolysis remained below 5% at the highest reported concentration (Fig. 6E), and intravenous doses of 25–150 mg/kg caused no deaths in four healthy BALB/c mice per dose. These findings provide preliminary formulation-level compatibility evidence, without tumor-delivery, pharmacokinetic, or in vivo efficacy validation [41].

Across eight studies evaluating seven breast-cancer platforms, evidence for benefits obtained by adding albumin was uneven. Tan et al. and Iqbal et al. provided the clearest matched-carrier comparisons, linking BSA coating to delivery, circulation, or therapeutic performance, although receptor mechanisms remained untested. Zhao et al. isolated improved cellular compatibility after replacing a CTAB-rich interface, but not systemic BSA effects. The Carrese studies showed accessible HSA drug-binding sites and greater tumor-spheroid interaction, but lacked an HSA-free therapeutic control. Mahmoud et al. and Hashemi et al. lacked albumin-free biological controls. In Zhang et al., BSA formed an inner shell, while the red-blood-cell membrane was the outer and directly compared interface. Thus, albumin served stabilizing, drug-binding, compatibility-modifying, or uptake-associated functions, but no study isolated it as the sole driver of complete targeting or multimodal response. Interface persistence after secondary-corona formation remained unresolved.

5.3. Hepatocellular carcinoma: corona-protected small interfering RNA

Yang et al. precoated redox-responsive chitosan-based nanoparticles (TsR) with cyclic RGDyK peptide-modified BSA for delivery of small interfering RNA (siRNA) targeting vascular endothelial growth factor (siVEGF) in Bel-7402 hepatocellular carcinoma models [42]. The chitosan-based core complexed siRNA and supported lysosomal escape and redox-responsive release, whereas the composite BSA-cRGD layer was intended to limit secondary protein adsorption and promote tumor-cell interaction. Relative to uncoated TsR nanoparticles, precoating improved dilution stability, reduced serum-protein adsorption from 1.720 to 0.901 mg/mg carrier, and protected siRNA in 50% FBS without abolishing redox-responsive release. It also increased cellular uptake and lysosomal escape, produced an additional 13% reduction in VEGF messenger RNA (mRNA) relative to the uncoated siVEGF-loaded carrier, and significantly reduced tumor volume and weight in the matched in vivo comparison. These matched comparisons support a delivery benefit from the composite BSA-cRGD interface. However, the absence of BSA-only and cRGD-only coating controls prevents separation of their individual contributions.

Building on the earlier BSA-cRGD strategy, Wu et al. subsequently used cRGD-modified BSA precoating (BcR) on siVEGF-loaded chitosan-based nanoparticles (CsR/siVEGF) to examine delivery and the subsequently acquired serum corona [28]. CsR/siRNA/BcR particles measured 172.22 ± 0.75 nm and +23.43 ± 2.57 mV and adsorbed approximately 67% less total serum protein than uncoated CsR particles despite retaining a positive surface charge. Relative to uncoated CsR/siVEGF, BcR precoating improved serum stability and siRNA protection and enhanced inhibition of tumor growth and angiogenesis.

In Bel-7402 xenografts (n = 5), five intravenous doses over 10 days reduced VEGF mRNA and protein to approximately 30% and 25% of saline-control levels, respectively. Coculture assays also showed reduced endothelial-cell proliferation, migration, invasion, and tube formation ($p < 0.01$ for all endpoints). These outcomes reflect the activity of the complete chitosan-siVEGF-cRGD-BSA formulation, not of albumin alone. LC-MS/MS identified 693 proteins on CsR and 695 on CsR/BcR particles, with 528 shared; the BcR-associated corona showed 6.80-fold serotransferrin enrichment, 1.59-fold albumin enrichment, and approximately 17.9-fold lower complement factor D. Thus, BcR reduced total adsorption but did not prevent secondary-corona formation, instead quantitatively reshaping its composition. Because particles were incubated ex vivo with serum from tumor-bearing mice rather than recovered after circulation, the proteomic results do not represent an in vivo corona. The proposed functional roles of the altered proteins also remain untested by blocking, depletion, receptor-inhibition, or complement-activity experiments.

5.4. Ovarian cancer: albumin-stabilized drug nanocrystals

Palazzolo et al. evaluated HSA-stabilized nanocrystals of MAGL23, a reversible monoacylglycerol lipase (MAGL) inhibitor (K_i = 39 nM), without a conventional polymeric or inorganic carrier core. The system was carrier-free in the drug-nanocrystal sense, but not excipient-free: Pluronic F-127 was used during nanocrystallization before HSA addition, washing, centrifugation, lyophilization, and resuspension. The process increased aqueous drug content approximately 1000-fold relative to intrinsic solubility. The albumin-formulated MAGL23 nanocrystals (MAGL23AF) contained 22 ± 4% HSA by weight, had a hydrodynamic diameter of 395.4 nm and a PDI of 0.1, and released 42 ± 6% of the drug over 72 h [43]. Compared with unformulated MAGL23, MAGL23AF showed greater stability in human liver microsomes at 40 and 60 min ($p < 0.05$). In 50% FBS/PBS, stability showed a favorable trend at 168 h, but the difference was not statistically significant. In subcutaneous OVCAR5 xenografts (n = 6), four weekly intraperitoneal doses of 20 mg/kg produced a tumor-inhibition rate of 53% at day 25, versus 21% for unformulated MAGL23 ($p < 0.05$) (Fig. 7A). Intratumoral necrosis was approximately 40% with MAGL23AF, 20% with unformulated drug, and less than 10% in untreated controls. Stable body weight supports short-term tolerability only. A separate pharmacokinetic study in FVB/N mice used 100 mg/kg intraperitoneally and found a significantly greater plasma area under the concentration-time curve (AUC) for MAGL23AF. Because strain, dose, and cohort differed from the efficacy experiment, increased exposure cannot be directly linked to the xenograft response.

The demonstrated benefits apply to the complete Pluronic F-127/HSA formulation. Without matched nanocrystals lacking HSA, the albumin-specific contribution cannot be quantified. Proposed gp60- or SPARC-mediated targeting was not tested by receptor blocking or genetic intervention. Other limitations include one subcutaneous xenograft, small cohorts, short follow-up, and no measurement of HSA retention, exchange, or secondary-corona formation after systemic exposure.

5.5. Glioblastoma: drug-gene co-delivery and brain-tumor targeting

Afonso et al. optimized a noncovalently BSA-coated WRAP5 peptide nanocomplex for co-delivery of temozolomide (TMZ) and p53 plasmid DNA (pDNA) [44]. In the selected formulation, 0.08% BSA was added 25 min after formation of the peptide-pDNA core at a nitrogen-to-phosphate (N/P) ratio of 1.03. Relative to the matched BSA-free complex, coating increased the hydrodynamic diameter from 140.7 to 182.3 nm, shifted the zeta potential from +13.4 to +9.8 mV, increased the PDI from 0.220 to 0.248, and reduced pDNA complexation from 99.8% to 96.5%. The coating did not uniformly improve physicochemical properties. Both formulations protected pDNA for 4 h in culture medium containing 10% FBS, so protection was not albumin-specific. Rat-erythrocyte hemolysis decreased from 5.9% to 3.9%, while HA1800 astrocyte viability did not differ significantly. In U87 cells, coating produced greater viability loss at 24 and 48 h, but not at

72 h (Fig. 7B), and conventional reverse-transcription polymerase chain reaction (RT-PCR) qualitatively detected p53 transcription. Because uptake and the proposed SPARC and gp60 pathways were not tested, these outcomes remain attributable to the complete TMZ-WRAP5-p53-BSA formulation. No barrier or animal study, pharmacokinetics, biodistribution, BSA-retention, or secondary-corona evaluation was performed.

Leung et al. [27] coated nanodiamonds with a multicomponent dcBSA-PEG-streptavidin-RGD interface for glioblastoma imaging. dcBSA served as the coating and scaffold for 2–4 biotinylated PEG chains; RGD was introduced through streptavidin-biotin assembly [27]. The final particles measured 73.28 ± 0.31 nm and +12.10 ± 2.60 mV in water. Because dcBSA-PEG nanodiamonds were negatively charged before completion of the streptavidin-RGD assembly, the final positive charge cannot be attributed to BSA cationization alone. In an endothelial model with a transendothelial electrical resistance (TEER) of only 27.23 ± 2.46 $\Omega \cdot cm^2$, relative permeability at 480 min increased from 32.1 ± 5.4% for dcBSA-PEG nanodiamonds to 53.5 ± 2.1% for the RGD-containing construct. These values were normalized to cell-free inserts, not an absolute administered-dose fraction crossing an intact blood-brain barrier. RGD also increased U-87 MG uptake approximately 4-fold at 1 h (500 μg/mL), without significant short-term cytotoxicity up to 1000 μg/mL; proposed uptake pathways were not tested. After one intravenous dose of 8.75 mg/kg in mice bearing intracranial U-87 MG xenografts (n = 4 per nanoparticle group), the RGD-containing construct produced greater tumor-associated cyanine 7 (Cy7) fluorescence at 24 h than the non-RGD formulation. This supports greater accumulation of the complete construct, but does not distinguish intact barrier transcytosis from blood-tumor barrier disruption or vascular leakage. Cy7 labeled the protein interface rather than the nanodiamond core. The result therefore reflects the combined effects of dcBSA modification, PEGylation, streptavidin, RGD, charge, and tumor vascular properties, not albumin alone. Small groups, one imaging time point, no formal pharmacokinetics, and no independent assessment of core and interface persistence further limit interpretation.

Afonso et al. and Leung et al. represent complementary but non-equivalent applications under "Glioblastoma: Drug-Gene Co-delivery and Brain-Tumor Targeting." Afonso et al. used a relatively simple noncovalent BSA coating and a matched BSA-free formulation, providing stronger evidence that albumin addition reduced hemolysis and transiently influenced the U87 cellular response; however, the study remained entirely in vitro and did not evaluate barrier transport or animal delivery. Leung et al. examined a more complex dcBSA-PEG-streptavidin-RGD interface and extended the evaluation to an endothelial model and intracranial xenograft imaging, but the enhanced transport, uptake, and tumor-associated fluorescence cannot be attributed independently to albumin or interpreted as demonstrated transport across an intact BBB. Thus, Afonso provides the stronger albumin-specific control design, whereas Leung provides broader biological and imaging evidence. Neither study established persistence of the engineered albumin interface, formal pharmacokinetics, intact in vivo BBB transcytosis, or therapeutic efficacy in glioblastoma.

5.6. Colorectal cancer: albumin-stabilized combination chemotherapy

Li et al. intercalated 5-fluorouracil (5FU) into Mg2Al layered double hydroxide (LDH) nanoparticles, then adsorbed albumin-bound paclitaxel (Abraxane, ABX) together with additional BSA [45]. The resulting albumin-stabilized LDH (BLDH/5FU-ABX) had a hybrid ABX/BSA interface rather than a simple BSA coating. Relative to LDH/5FU, adding ABX and BSA increased the diameter from 95.0 ± 5.5 to 168.3 ± 2.0 nm, increased the PDI from 0.112 to 0.181, and shifted the zeta potential from +42.6 to −14.0 mV; 5FU and ABX loading efficiencies were 56.4 ± 7.4% and 93.2 ± 5.2%, respectively. Because ABX and BSA were added together, these changes cannot be assigned to BSA independently. The clearest interface-level benefit was colloidal stabilization: LDH/5FU aggregated in PBS and reached 339.4 ± 7.4 nm in serum-containing Dulbecco's modified Eagle's medium (DMEM), whereas BLDH/5FU-ABX remained approximately 165 nm in both media. At pH 5.5, coated and uncoated carriers each released approximately 90% of 5FU within 120 min, indicating that acid-responsive release mainly reflected LDH dissolution. DLS stability and a BSA-FITC exchange surrogate did not establish resistance to secondary-corona formation or ABX retention during circulation.

In HCT-116 cells, BLDH-mediated delivery increased BSA-FITC uptake approximately 6-fold over free BSA-FITC, demonstrating a carrier-mediated uptake advantage rather than albumin-specific targeting. At 1.25 μg/mL 5FU and 2.0 μg/mL ABX, the dual formulation reduced viability to approximately 15%, versus approximately 58% and 55% for the single-drug formulations, with a reported combination index of 0.48. In HCT-116 xenografts (n = 6), three intravenous injections on days 0, 4, and 8 delivered 3 mg/kg 5FU and 20 mg/kg ABX, equivalent to 2 mg/kg paclitaxel, and produced greater tumor-growth inhibition and necrosis than either single-drug formulation. Stable body weight and unremarkable major-organ histology support short-term tolerability only. These outcomes support synergistic chemotherapy by the complete LDH-5FU-ABX-BSA system. Without an albumin-free dual-drug carrier, a free 5FU-ABX combination, formal pharmacokinetics, direct biodistribution in the efficacy experiment, or comprehensive safety testing,

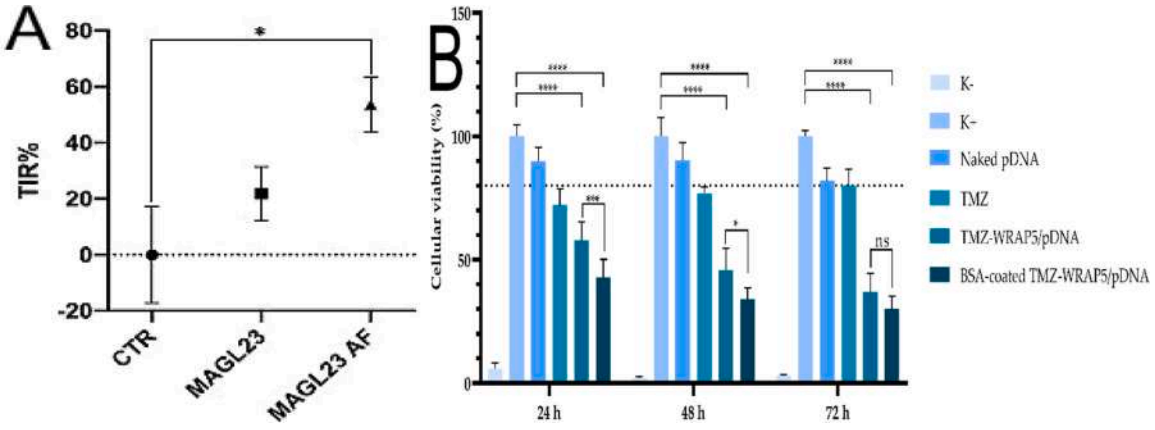

Fig. 7. Representative therapeutic outcomes illustrating different levels of albumin-interface attribution. (A) Tumor-inhibition rate in OVCAR5 xenografts following treatment with unformulated MAGL23 or HSA-formulated MAGL23 nanocrystals (MAGL23AF). The comparison demonstrates improved performance of the complete MAGL23AF formulation but does not isolate the contribution of HSA because a matched HSA-free nanocrystal formulation was not evaluated. (B) Viability of U87 glioblastoma cells after 24, 48, and 72 h exposure to TMZ/p53 delivery formulations, including matched BSA-free and BSA-coated TMZ-WRAP5/pDNA nanocomplexes. The matched comparison supports coating-associated differences at 24 and 48 h, whereas the effect was not maintained at 72 h.

efficacy and tolerability cannot be attributed specifically to albumin.

5.7. Skin cancer: silver-mediated and photothermal therapy

Kim et al. prepared BSA-coated silver nanoparticles by $NaBH_4$ reduction of silver nitrate in the presence of BSA, then removed unbound protein by centrifugal filtration [46]. The formulation remained size-stable for 5 days and had an approximately 100 nm core, a hydrodynamic diameter of 121.2 ± 43 nm, a PDI of 0.095, and a zeta potential of −31.3 ± 5.3 mV. Without a matched uncoated silver nanoparticle, the magnitude of BSA-mediated stabilization cannot be quantified. In B16F10 melanoma cells, the particles generated dose-dependent ROS and an IC50 of 65.8 ± 9.2 μM as silver, versus 120 ± 14.4 μM for silver ions. TEM supported internalization, and human umbilical vein endothelial cell experiments showed reduced proliferation, migration, and tube formation. After 690 nm irradiation for 10 min, viability fell to 8.2% and 4.2% at maximum temperatures of 45 and 50 °C, respectively. These outcomes characterize the complete BSA-silver formulation. This in vitro study did not evaluate serum-interface evolution, pharmacokinetics, tumor delivery, efficacy, or systemic toxicity.

Amatya et al. complexed Cu^{2+} with BSA before $NaBH_4$ reduction, so BSA participated in copper nanoparticle formation and provided the aqueous interface [47]. The particles measured 93.5 ± 9 nm, with a PDI of 0.13 and a zeta potential of −10.9 ± 5.5 mV, and retained size and photothermal performance for 5 days at 4 °C. A matched BSA-free copper nanoparticle was not tested, so albumin-specific effects on biological performance cannot be determined. At 120 μg Cu/mL in B16F10 cells, viability was 67.8% without irradiation and 23.8%, 8.4%, and 7.9% after 885 nm irradiation for 10 min at 1.0, 1.2, and 1.3 W, respectively; laser alone caused little cytotoxicity. In healthy mice (n = 3 per dose), no deaths occurred at or below 16 mg Cu/kg, whereas doses above 32 mg Cu/kg caused deaths within 24 h. A separate intravenous study of an indocyanine green (ICG)-loaded variant in healthy mice (n = 5), at 420 μg ICG/kg and 40 mg BSA/kg, yielded a 1.98 h plasma half-life, an AUC of 769 μg h/mL, and a 2.7 h mean residence time. Because plasma fluorescence tracked ICG in a labeled variant rather than copper directly, these values do not establish copper-core pharmacokinetics or tumor imaging.

Comparison of the two studies shows similar interfacial roles but different evidence depth. Kim *et al.* provided broader in vitro evidence, including ROS-associated melanoma cytotoxicity, cellular localization, antiangiogenic activity, and silver-mediated photothermal killing, but no animal data. Amatya *et al.* demonstrated copper-mediated photothermal killing and added preliminary acute-tolerability and plasma-disposition measurements in healthy mice, but did not test tumor delivery or in vivo efficacy. In both systems, BSA supported metal-particle formation, aqueous dispersion, and short-term storage stability, whereas ROS generation and photothermal conversion arose primarily from the metal cores. Because neither study included matched BSA-free nanoparticles, neither establishes albumin-specific tumor targeting, cellular uptake, antiangiogenesis, circulation extension, or therapeutic efficacy.

5.8. Gastric cancer: cisplatin delivery and photothermal treatment

Li et al. used carbodiimide chemistry to immobilize albumin on hydrothermally prepared magnetite nanoparticles containing cisplatin and perfluorohexane (PFH), producing A-PFH/C-MNPs [48]. Electron microscopy showed an approximately 131.2 nm diameter and an approximately 8.3 nm albumin-containing layer; cisplatin-loading efficiency exceeded 60%. At 1800 min, cisplatin release was 37.7%, 59.1%, and 73.5% at pH 7.5, 5.0, and 2.5, respectively. Gravimetric PFH loss at 60 min increased from less than 12% at 37 °C to approximately 59% at 45 °C. Albumin served as an interfacial scaffold, but no albumin-free release control isolated the proposed albumin gate. The cisplatin profile therefore cannot be assigned specifically to albumin, while the temperature-dependent measurement primarily reflects PFH volatilization.

In AGS gastric-cancer cells, A-PFH/C-MNPs combined with 808 nm photothermal treatment (PTT) produced 49.5% early and 30.8% late apoptosis, versus 34.8% and 28.7% for albumin-cisplatin-magnetite nanoparticles and 25.9% and 19.2% for free cisplatin, respectively. The irradiated PFH-containing formulation also produced the highest ROS signal and SubG1 population, each reported as 3.06-fold above the untreated control, and increased TNF-alpha, Bax, and caspase-3 expression. These results support the complete combination formulation. However, the key comparison lacked both the PFH-containing formulation without irradiation and the PFH-free formulation with irradiation, so PFH and PTT effects cannot be separated. This cell-culture study did not report sample size or evaluate pharmacokinetics, tumor delivery, in vivo efficacy, or systemic safety.

5.9. Testicular embryonal carcinoma: folate-modified diosgenin delivery

Ayatollahi et al. adsorbed BSA onto green-synthesized ZnO nanoparticles, incorporated diosgenin (DG), crosslinked the protein-containing assembly with glutaraldehyde, and coupled FA through carbodiimide chemistry [49]. The resulting ZnO-BSA-DG-FA particles measured 243.13 nm by dynamic light scattering and approximately 100 nm by scanning electron microscopy, with a PDI of 0.33, a zeta potential of −20.76 mV, DG encapsulation of 81.38%, and FA coupling of 52.09%. BSA thus formed a crosslinked hybrid interface that accommodated DG and supplied groups for FA conjugation. A single zeta-potential measurement does not establish storage or serum stability, and the absence of matched ZnO, ZnO-BSA, BSA-DG, and BSA-free controls prevents isolation of BSA effects on dispersion, loading, ligand presentation, or delivery.

After 48 h, the complete formulation produced an IC50 of 13.47 μg/mL in NTERA-2 cells, versus 20.46 μg/mL in human umbilical vein endothelial cells and greater than 25 μg/mL in human foreskin fibroblasts. It increased the SubG1 population and caspase-3 and caspase-9 transcript levels without a significant caspase-8 change. These findings are consistent with intrinsic apoptotic signaling but do not demonstrate protein activation or identify the responsible component. The modest normal-cell comparison reflects formulation-level differential cytotoxicity; folate-receptor dependence, cellular uptake, serum-interface evolution, and in vivo efficacy were not tested.

5.10. Prostate cancer: albumin-coated metallic nanoparticles

Zareian Baghdadabad et al. compared PVP-stabilized silver nanoparticles (AgNPs) with a BSA-containing formulation in PC3 and LNCaP prostate-cancer cells [50]. Coating increased the mean hydrodynamic diameter from 26.5 ± 8.88 to 76.70 ± 30.9 nm and reduced the 24 h IC50 from 48 ± 0.32 to 32 ± 0.08 μM in PC3 cells and from 110 ± 1.74 to 95 ± 1.32 μM in LNCaP cells. AgNPs-Alb more strongly inhibited PC3 migration and colony formation in both cell lines. Early apoptosis increased from 20.9% to 44.4% in PC3 cells, whereas the corresponding LNCaP values decreased from 70.7% to 66.7%. The coating was also associated with a higher LNCaP SubG1 fraction, lower VEGF-A expression, and higher Bax/Bcl2 ratios, but not with uniform improvement across all endpoints. Although the paired formulations support coating-associated effects, most downstream assays used one-half of each formulation's own IC50, creating unequal silver-formulation concentrations. Cellular uptake, albumin-receptor involvement, normal-cell toxicity, physiological stability, secondary-corona formation, and animal outcomes were not evaluated.

Mahmoud et al., whose BSA-gold architectures are described in Section 5.2, also evaluated GNR-BSA and GNS-BSA in DU-145 and PC-3 cells [38]. GNR-BSA produced greater cytotoxicity and uptake, approximately 10% in DU-145 and 14% in PC-3 cells, versus less than 0.4% for GNS-BSA, and more strongly delayed scratch closure; adhesion effects were modest. Because BSA-coated rods were compared with BSA-coated spheres rather than with albumin-free counterparts of each

geometry, these are formulation-level effects of shape, size, precursor chemistry, and BSA presentation.

Zareian Baghdadabad et al. provide the stronger coating-addition control, whereas Mahmoud et al. demonstrate geometry-dependent behavior between two BSA-coated gold architectures. Neither study establishes albumin-receptor targeting, durable serum-interface stability, reduced immune recognition, or in vivo prostate-tumor delivery. Across the ten cancer-specific settings, engineered albumin interfaces served different functions, including charge modulation, ligand and payload presentation, nucleic-acid protection, nanocrystal or colloidal stabilization, and compatibility of metallic or photothermal platforms. Substantial differences in cores, albumin architectures, co-components, payloads, routes, models, and comparator quality demonstrate platform adaptability but preclude quantitative ranking as equivalent albumin-specific effects.

6. Corona proteomics: current evidence and future diagnostic validation

Engineered albumin-containing interfaces may eventually support proteomics-assisted cancer research by acting as standardized nanoconcentrators that enrich selected proteins from complex biological samples. In the present evidence base, however, only two included studies characterized secondary-corona composition by LC-MS/MS, and neither evaluated cancer-patient cohorts, disease discrimination, diagnostic sensitivity or specificity, receiver operating characteristic curves, predictive values, or independent validation. Corona proteomics should therefore be presented as a hypothesis-generating research framework rather than an established diagnostic or liquid-biopsy method.

6.1. Direct corona-proteomic evidence and attribution limits

Bozzer et al. compared otherwise similar PLGA-PVA nanoparticles with and without covalently immobilized HSA after 1 h in normal human serum. LC-MS/MS identified 105 protein species on NP-HSA and 79 on uncoated nanoparticles, with 31 shared proteins [24]. NP-HSA showed greater relative representation of albumin, ApoA1, ApoA2, ApoC3, and clusterin, while no proteins from the terminal complement pathway were documented (Fig. 8A). The larger number of identified species does not establish greater total protein mass; rather, the matched comparison directly shows that HSA immobilization altered corona diversity and composition instead of preventing secondary adsorption. Reduced macrophage uptake was associated with this altered profile, but the causal contribution of individual proteins was not tested, and the targeting and therapeutic outcomes remain attributable to the complete HSA-anti-CD19-doxorubicin formulation.

Wu et al. compared chitosan-based CsR nanoparticles with a composite cRGD-modified BSA precoating using serum collected from tumor-bearing mice [28]. LC-MS/MS identified 693 proteins on CsR and 695 on CsR/BcR, with 528 shared; serotransferrin and albumin were enriched 6.80-fold and 1.59-fold, respectively, while complement factor D was reduced to approximately 1/17.9 of the level on CsR (Fig. 8B). These findings demonstrate corona reshaping by the composite cRGD-BSA interface, not by albumin alone, because BSA-only, cRGD-only, and protein-replacement controls were absent. The nanoparticles were incubated ex vivo with tumor-bearing mouse serum rather than injected and recovered after circulation. Serotransferrin-mediated targeting and complement-associated immune effects therefore remain untested interpretations, while the antiangiogenic outcomes belong to the complete siVEGF-loaded formulation. Together, these studies support surface-design-dependent secondary-corona composition. Bozzer et al. provide the stronger albumin-specific comparison, whereas Wu et al. establish an effect of a composite cRGD-BSA interface. Neither study validated an individual corona protein as a targeting, stealth, or diagnostic mechanism.

6.2. Diagnostic potential and current evidence boundaries

Standardized nanoparticle panels could potentially enrich selected protein subsets and generate candidate corona fingerprints for cancer research. This remains hypothetical because neither included proteomic study tested human cancer samples, distinguished patients from controls, or evaluated diagnostic performance. Any comparison with established liquid-biopsy approaches should therefore be framed as a future validation objective, not a demonstrated advantage.

Clinical translation requires standardized sample collection, corona formation, nanoparticle recovery, washing, protein desorption, LC-MS/MS acquisition, database searching, quality control, and reporting. Across multicenter studies, standardized processing improved reproducibility, including an increase in interfacility overlap in identified corona proteins from approximately 11–40% in one study, although substantial variability remained [51,52]. Tumor type and stage, medication, age, inflammation, and other physiological variables may further confound disease-associated signatures. Prospective, appropriately matched human cohorts, locked analytical workflows, predefined performance criteria, and independent validation are therefore required before diagnostic claims are justified.

6.3. Emerging methodological directions for corona characterization

Recent analytical developments could extend corona characterization beyond bulk end-point proteomics. Single-particle inductively coupled plasma mass spectrometry (ICP-MS) or tandem ICP-MS/MS can measure particle-number concentration and, for suitable elemental cores, infer size distributions. Applied before and after recovery, these measurements could quantify particle loss and support normalization of proteomic abundance to particle number. Cryo-electron microscopy (cryo-EM) and cryo-electron tomography can visualize corona morphology, spatial heterogeneity, and particle-to-particle variation, although they do not identify the observed biomolecules as albumin without an independent molecular assay. Single-particle ICP-MS likewise does not identify surface proteins, and cryogenic imaging may underrepresent rapidly exchanging soft-corona components. These methods should therefore complement, rather than replace, quantitative proteomics [53,54]. Proteoform-resolved top-down mass spectrometry may distinguish intact albumin, complement, apolipoprotein, and coagulation-protein variants that conventional peptide-based analysis can combine under the same protein identity [55]. High-throughput magnetic-nanoparticle enrichment and rapid on-bead digestion workflows could support larger clinical cohorts and nanoparticle-panel screening [56]. Nanoflow cytometry can quantify protein adsorption and particle-to-particle heterogeneity in situ at the single-particle level while monitoring nanoparticle aggregation in serum. Its molecular specificity depends on fluorescence labeling, so it does not provide untargeted protein identification and should complement mass spectrometry [57].

These advances require rigorous artifact control and workflow harmonization. Digestion protocol selection can substantially alter protein recovery, representation, and the apparent corona profile [58,59]. Future studies should combine particle-number normalization, structural imaging, mass spectrometry, appropriate biological-fluid controls, and functional validation. For albumin-containing interfaces, the nanoparticle core and albumin layer should be traced independently before biological exposure, after controlled serum incubation, and following recovery from circulation. This integrated approach could determine albumin retention, displacement, secondary-corona formation, and their relationships with biological outcomes, but it does not itself establish diagnostic validity.

6.4. Conceptual diagnostic validation pathways

Studies in this field should distinguish among three evidence levels:

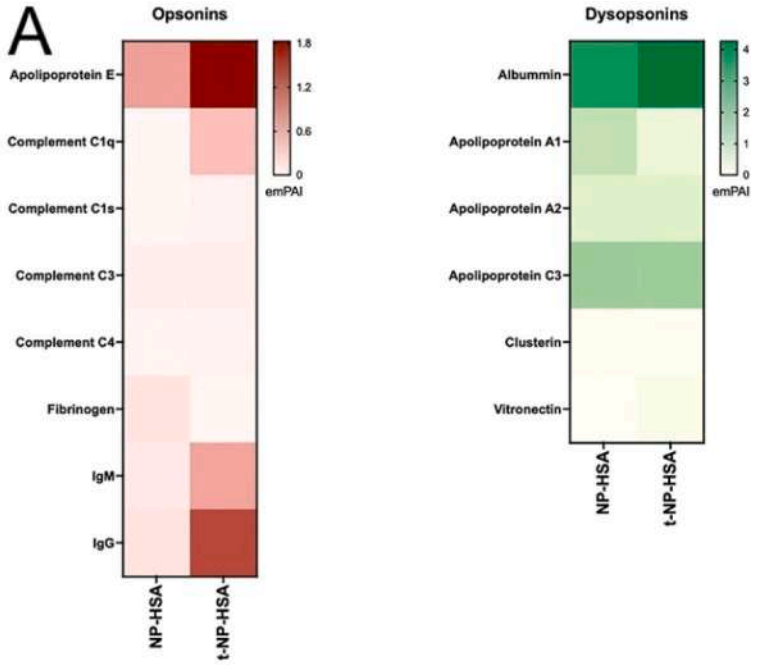

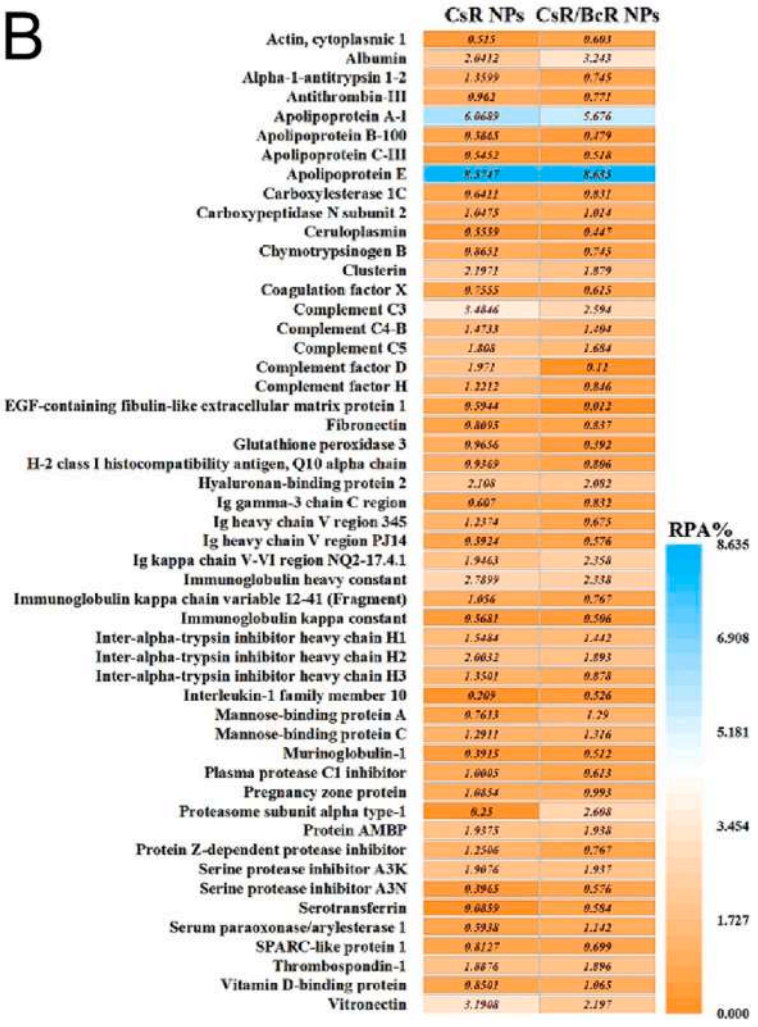

(caption on next page)

Fig. 8. Secondary-corona proteomic remodeling by engineered albumin-containing nanoparticle interfaces. (A) Relative representation of selected opsonin- and dysopsonin-associated proteins identified after serum exposure of uncoated PLGA-PVA nanoparticles (NP) and nanoparticles bearing covalently immobilized HSA (NP-HSA), illustrating HSA-interface-associated changes in secondary-corona composition. (B) Heat map of abundant corona proteins identified on chitosan-based CsR nanoparticles and particles bearing the composite cRGD-modified BSA precoating (CsR/BcR) after ex vivo incubation with serum from tumor-bearing mice. The two studies demonstrate surface-design-dependent corona remodeling, but neither establishes a causal biological or diagnostic role for individual corona proteins.

directly demonstrated changes in corona composition associated with an engineered albumin interface, biological outcomes attributable to the complete formulation, and mechanistic interpretations inferred from the reported functions of individual corona proteins. The available proteomic studies demonstrate that nanoparticle surface design can influence the composition of coronas generated under controlled serum or plasma exposure. However, they do not establish cancer detection, patient classification, diagnostic accuracy, or a causal relationship between an individual corona protein and a biological outcome.

Fig. 9 therefore presents a conceptual framework for future diagnostic validation rather than an experimentally established workflow. The proposed ex vivo pathway involves incubating a defined nanoparticle panel with prospectively collected samples from cancer patients and appropriately matched controls under standardized preanalytical and analytical conditions. Candidate corona signatures would require predefined quality-control criteria, a locked classification model, sensitivity, specificity, receiver operating characteristic and area-under-the-curve analyses, predictive-value estimation, reproducibility assessment, and independent external validation.

An optional in vivo nanoconcentrator pathway (Fig. 9) would involve systemic administration of a defined nanoparticle, recovery of the circulating particles after a predetermined interval, preservation and LC-MS/MS analysis of the acquired corona, and comparison with independently validated reference profiles. None of the reviewed studies completed this workflow. Its feasibility remains uncertain because nanoparticle dosing safety, recovery efficiency, interface evolution, corona preservation, biological variability, and diagnostic reproducibility have not been established. Accordingly, neither pathway should be presented as an available method for early cancer detection or liquid biopsy. Quantitative particle-recovery studies, matched albumin-free and alternative-protein controls, prospective patient cohorts, predefined diagnostic thresholds, and independent validation are required before clinical relevance can be assessed.

7. Critical evaluation and future outlook

The strength of albumin-specific attribution varied substantially across the reviewed systems. Table 4 therefore distinguishes direct albumin/interface evidence from formulation-level outcomes and proposed or untested albumin-related mechanisms.

7.1. *In vivo persistence and evolution of pre-engineered albumin interfaces*

Pre-injection size, charge, coating thickness, drug loading, and colloidal stability characterize the manufactured formulation, not its biological identity after administration. Noncovalently adsorbed albumin may desorb or exchange, whereas covalent or crosslinked layers may persist yet become conformationally masked by a secondary corona. Thus, immobilization does not establish that albumin remains the dominant exposed interface in vivo [60,61]. No reviewed study recovered a formulation from the circulation of a tumor-bearing mammalian model and directly quantified the retention, conformation, orientation, or exchange of its engineered albumin layer. Traverso et al. relied on short-term DLS [23]; Bozzer et al. [24] and Wu et al. [28] characterized coronas generated under controlled serum conditions; Caputo et al. observed serum-associated particle growth [18]; and Li et al. used a BSA-FITC exchange surrogate [45]. These findings describe restricted in vitro or ex vivo conditions and do not establish interface persistence after systemic circulation. Such whole-formulation readouts, including blood half-life, whole-particle fluorescence, tumor accumulation, and efficacy, cannot by themselves establish retention of the engineered albumin layer [62]. Future studies should independently trace the core and albumin component, recover particles at multiple circulation times, and compare the manufactured, serum-exposed, and in vivo recovered interfaces using quantitative protein analysis and proteomics.

7.2. *Charge, albumin conformation, and glycocalyx interactions*

The positively measured interfaces reported by Wu et al. and Leung et al. remained compatible with siVEGF activity or transport in an endothelial model, but neither study used charge-matched controls. Moreover, Leung's low-resistance barrier model and tumor fluorescence do not demonstrate transport across an intact blood-brain barrier. Zeta potential is medium-dependent and does not independently define ligand accessibility, local charge domains, macrophage avoidance, or circulation behavior.

Olivieri et al. [26] provided more direct mechanistic evidence by comparing silica nanoparticles coated with native, cationic, or anionic BSA. Cellular uptake depended on both albumin presentation and cell-surface glycosaminoglycans; cationic-BSA nanoparticle uptake fell 30-fold in glycosaminoglycan-deficient CHO cells [26]. This supports a glycocalyx-sensitive interaction rather than a universal charge rule, but the static cell models did not establish tumor targeting, immune stealth, pharmacokinetics, or in vivo efficacy. Accordingly, apparent charge-function decoupling remains a hypothesis requiring matched controls for charge, albumin conformation, PEG and ligand density, followed by corona, complement, macrophage, pharmacokinetic, and biodistribution testing.

7.3. *Stealth as corona composition rather than protein exclusion*

Bozzer et al. [24] and Wu et al. [28] showed that albumin-containing interfaces can alter secondary-corona composition rather than eliminate protein adsorption. Bozzer *et al.* associated an altered corona profile with reduced macrophage uptake, whereas Wu et al. reported enrichment and depletion of selected serum proteins. Neither study established a causal role for an individual corona protein or a universal albumin-mediated stealth mechanism. Likewise, the absence of documented proteins from the terminal complement pathway in the Bozzer dataset cannot be equated with complete complement blockade, because early complement components, immunoglobulins, coagulation proteins, scavenger receptors, and other phagocytic pathways remain relevant. Stealth should therefore be evaluated using quantitative adsorption, corona composition, complement activation, immune-cell uptake, and in vivo clearance rather than DLS stability or albumin presence alone.

7.4. *Translational and mechanistic validation challenges*

Albumin source remains a major translational variable. Most reviewed formulations used BSA or modified BSA, although BSA is xenogeneic in humans and is not functionally interchangeable with HSA. BSA and HSA share approximately 76% amino-acid sequence similarity, and differences in exposed residues, ligand binding, receptor recognition, and adsorption-induced epitopes may alter loading, release, corona formation, and immune interactions [63]. Pre-existing anti-BSA IgG and exposure-associated increases were reported in humans, although no related clinical events were detected in that study [64]. Species

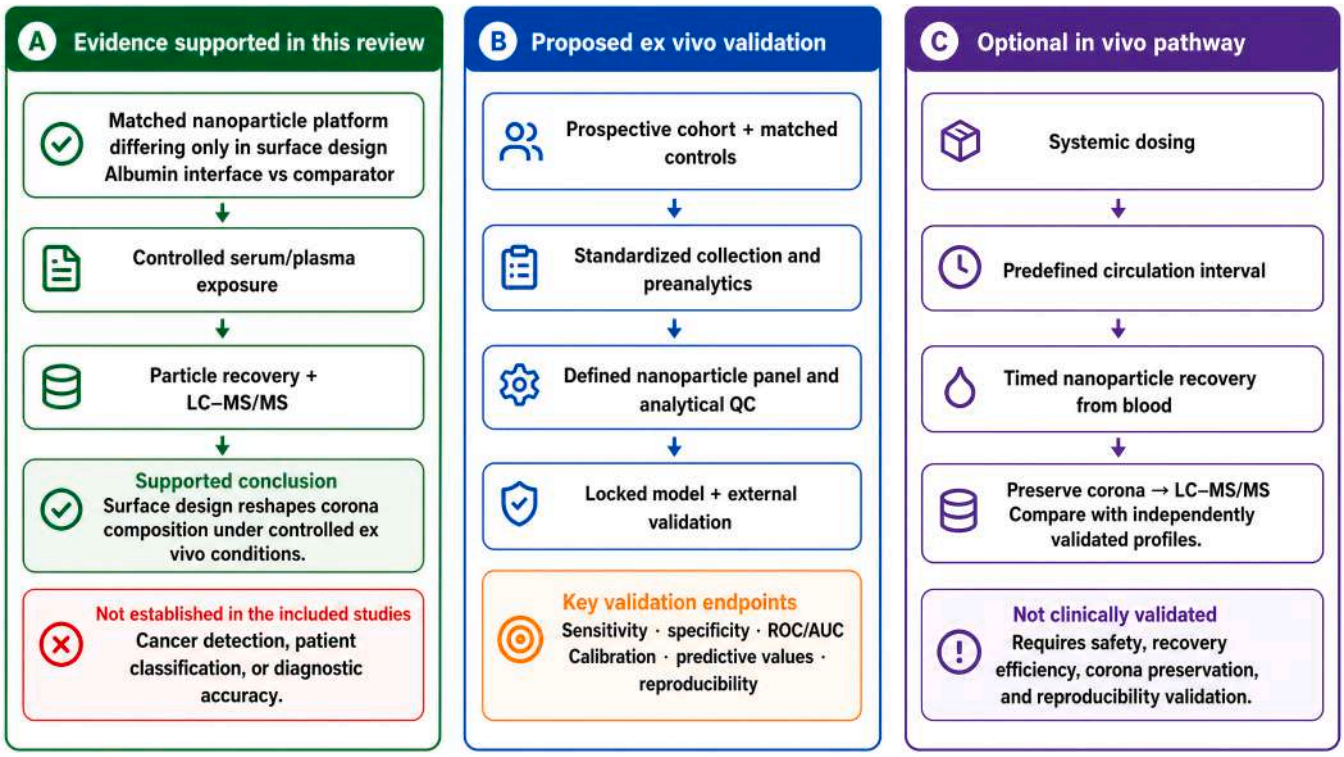

Fig. 9. Evidence boundaries and proposed validation pathways for nanoparticle-corona proteomics in cancer research. The framework distinguishes currently demonstrated secondary-corona remodeling from proposed ex vivo diagnostic-validation and optional in vivo nanoconcentrator pathways. The latter pathways remain conceptual and have not been clinically validated.

differences also complicate interpretation of receptor-mediated circulation and pharmacokinetics. At acidic pH, cross-species experiments showed an approximately 100-fold affinity difference between mouse neonatal Fc receptor (FcRn) binding to HSA, about 90 μM, and human FcRn binding to mouse albumin, 0.8 μM [65]. Thus, the circulation behavior of a BSA-containing formulation in mice does not establish equivalent FcRn-mediated recycling for an analogous HSA formulation in humans. This limitation is additional to the unresolved question of whether nanoparticle-bound albumin retains the conformation and receptor accessibility required for FcRn engagement. BSA systems should therefore be treated as proof-of-concept unless matched BSA and HSA formulations demonstrate comparable physicochemical, immunological, and pharmacokinetic behavior. Caputo et al. showed that HSA could form the intended coating during formulation screening, but subsequent biological experiments used BSA and did not establish biological equivalence between the two albumins [18]. Human-directed development should use well-characterized pharmaceutical-grade or recombinant HSA. A trial of recombinant HSA in healthy participants assessed the free protein, not a nanoparticle-bound HSA interface [66]; candidate nanoformulations still require testing of conformation, FcRn accessibility, corona evolution, complement activation, anti-albumin responses, repeated-dose safety, and manufacturing consistency. FcRn recycling, gp60 transcytosis, SPARC association, and transferrin-receptor targeting remain plausible but mostly inferred. Receptor expression, ligand enrichment, or tumor accumulation alone does not demonstrate receptor-mediated transport. These mechanisms require receptor blocking or genetic perturbation, ligand depletion, competitive binding, and matched albumin-free or ligand-free controls before albumin-specific causality is claimed.

7.5. Immunotherapy integration as an unvalidated future direction

Albumin-engineered interfaces may eventually be combined with immune-modulating payloads, checkpoint blockade, or treatments that induce immunogenic cell death. However, no reviewed study tested an albumin-interface formulation with programmed cell death protein 1 (PD-1) or programmed death-ligand 1 (PD-L1) blockade or established a causal effect on antitumor immunity. Even complete tumor disappearance reported for a photothermal multicomponent formulation [15] cannot be interpreted as evidence of immunogenic cell death without immune-cell profiling, rechallenge, depletion, or checkpoint-combination experiments. Immunotherapy integration should therefore remain a testable future direction rather than a demonstrated platform capability.

8. Conclusion

Engineered albumin interfaces have been investigated as functional components of non-albumin nanoparticles and drug nanocrystals across diagnostic imaging, theranostics, controlled release, tumor targeting, and biological-identity modulation. Their contributions are architecture- and formulation-dependent rather than universal. The strongest evidence supports coating-associated changes in colloidal behavior, surface charge, payload association and release, cellular interaction, macrophage uptake, and secondary-corona composition. Direct attribution of an incremental effect to the albumin-containing interface requires matched albumin-free comparators or albumin-specific mechanistic interventions.

Pharmacokinetic, biodistribution, imaging, and therapeutic outcomes generally remain properties of the complete formulation because albumin was combined with targeting ligands, polymers, inorganic cores, membrane coatings, therapeutic payloads, or externally applied energy. Accordingly, these heterogeneous systems should not be ranked using nominal albumin-specific effect sizes. Proposed mechanisms involving FcRn, gp60, SPARC, transferrin receptors, integrins, or charge-mediated uptake also remain provisional unless verified by receptor blocking, competitive binding, genetic perturbation, ligand depletion, or otherwise matched controls. In vitro epithelial or endothelial

Table 4
Evidence attribution for albumin/interface-specific effects, formulation-level outcomes, and proposed mechanisms.

Study and formulation	Direct albumin/interface evidence	Formulation-level outcome	Proposed or untested albumin-related mechanism
Baki et al., 2021 BSA-coated Fe_3O_4 MNPs	Direct, physicochemical only: Coating-associated changes in size, charge, salt stability, and relaxivity were demonstrated against uncoated MNPs.	MRI/MPI contrast performance of the final BSA-coated Fe_3O_4 system.	In vivo stealth, prolonged circulation, and persistence of the BSA layer remain untested.
Wu T. et al., 2022 PS-BSA-AuNC-Apt probe	Partial physicochemical evidence: comparison with bare PS supported short-term colloidal stabilization by the BSA-AuNC-containing interface; aptamer-free comparisons isolated the aptamer contribution to targeting rather than a BSA-specific targeting effect.	Breast-cancer-cell detection and xenograft-section staining by the complete fluorescent aptamer probe.	Albumin-specific preservation of aptamer accessibility or biological recognition was not demonstrated.
Zhang et al., 2023 Fe_3O_4@BSA-TA-Fe^{3+}	Direct, physicochemical only: Fe_3O_4 versus Fe_3O_4@BSA supported a BSA-associated improvement in dispersion.	Tumor elimination, MRI contrast, photothermal activity, and ferroptosis produced by the complete formulation with irradiation.	The albumin-apo-transferrin-TfR targeting pathway remains unverified by blocking, depletion, or an albumin-free TA-Fe^{3+} control.
Petrov et al., 2025 HSA-coated OA/OA-Tween20 Fe_3O_4 MNPs	Direct, matched interface comparison: HSA-associated changes in stability, relaxivity, DOX loading, and blank-carrier cytotoxicity were demonstrated.	DOX release and A549 cytotoxicity of the complete HSA-coated magnetic formulations.	HSA-mediated tumor targeting and circulation prolongation were not tested in vivo.
Suwannasing et al., 2025 BSA@CuO nanoparticles	Direct, physicochemical only: Bare CuO versus BSA@CuO supported a coating-associated improvement in dispersion.	Radiosensitization, DNA-damage, apoptosis, and cell-cycle outcomes of BSA@CuO plus irradiation.	Albumin-specific cellular uptake and the proposed ROS/mitochondrial pathway were not directly tested.
Traverso et al., 2023 HSA/hTf-decorated CdSe/ZnS QDs	Partial outer-protein comparison: HSA versus hTf principally demonstrated an hTf-dependent effect; no albumin-free QD was included.	Digitoxin delivery, cellular uptake, and A549 growth inhibition by the complete protein-decorated QDs.	HSA-mediated caveolar uptake and complete prevention of secondary-corona formation were not demonstrated.
Bozzer et al., 2024 HSA-PLGA-PVA nanoparticles	Direct, matched interface comparison: HSA altered the acquired-corona profile and reduced macrophage uptake; no improvement in the measured complement outcome was found.	Zebrafish biodistribution, tumor targeting, DOX delivery, and survival outcomes of the complete targeted formulation.	An HSA-specific circulation advantage was not isolated in vivo because an uncoated comparator was absent.
Kumar et al., 2024 DC-field-engineered BSA-AuNPs	Direct, biophysical only: BSA adsorption and voltage-dependent changes in particle size, charge, and protein perturbation were demonstrated.	Curcumin-binding and hemolysis behavior of the tested BSA-gold systems.	Controlled cancer delivery remains hypothetical because no cancer-cell or animal experiment was performed.
Leung et al., 2021 RGD-dcBSA-PEG nanodiamonds	None isolated: RGD versus non-RGD nanodiamonds identified the RGD contribution, not the independent contribution of dcBSA.	Barrier-model transport, cellular uptake, and brain-tumor-associated fluorescence of the complete RGD-dcBSA-PEG system.	An albumin-specific BBB mechanism and a necessary role for positive charge were not independently established.
Li et al., 2020 BSA/HAP/DOX nanoparticles	Direct, matched interface comparison: BSA-free versus BSA-coated particles and free-BSA competition supported an albumin-related contribution to uptake and tumor accumulation and relative tumor-associated fluorescence.	Blood persistence, biodistribution, and antitumor outcomes of the complete BSA/HAP/DOX formulation.	The receptor pathway responsible for the albumin-related contribution was not identified.
Tan et al., 2021 BSA-CS-DOX nanoparticles	Direct, matched interface comparison: BSA-free versus BSA-coated particles supported coating-associated effects on serum stability, cellular uptake, tumor drug accumulation, and tumor response.	Tumor inhibition, survival, biodistribution, and toxicity outcomes of the complete BSA-CS-DOX formulation.	CD44 involvement was examined, but proposed gp60 and SPARC contributions were not directly tested.
Yang et al., 2021 Bc-coated TsR/siVEGF nanoparticles	Composite-interface evidence: TsR versus TsRBc demonstrated an effect of the cRGD-BSA layer, but BSA and cRGD contributions could not be separated.	VEGF silencing and tumor-growth suppression by the complete siVEGF-loaded chitosan formulation.	SPARC, integrin-mediated targeting, and reduced opsonization were not functionally validated.
Wu Z. et al., 2024 BcR-coated CsR/siVEGF nanoparticles	Composite-interface evidence: CsR versus CsR/BcR demonstrated an effect of the cRGD-BSA layer on protein adsorption and ex vivo corona composition.	VEGF suppression, antiangiogenic activity, and tumor response of the complete siVEGF-loaded formulation.	The functional roles of serotransferrin enrichment and complement-factor-D depletion remain untested.
Palazzolo et al., 2024 HSA-MAGL23/F127 nanocrystals	None isolated: No matched HSA-free F127 nanocrystal formulation was evaluated.	Solubility, pharmacokinetics, biodistribution, tumor response, necrosis, and tolerability of the complete formulation.	HSA-specific nanocrystal stabilization and tumor targeting were inferred rather than isolated.
Goel et al., 2026 CoFe2O4@BSA@Ag	Partial matched-interface evidence: CoFe2O4 versus CoFe2O4@BSA supported an albumin-associated change in H1299 cytotoxicity, but physicochemical characterization did not consistently include the BSA-only intermediate	Apoptosis, migration and colony inhibition, hemocompatibility, and normal-cell viability were outcomes of the complete CoFe2O4-BSA-Ag composite	Tumor targeting, in vivo biocompatibility, circulation behavior, and stability or persistence of the BSA interface remain untested
Afonso et al., 2024 BSA-coated TMZ-WRAP5/p53 nanocomplexes	Direct, matched-interface evidence: BSA-free versus BSA-coated complexes demonstrated coating-associated changes in size, charge, hemolysis, and U87 viability at 24 and 48 h; pDNA protection and astrocyte viability were not improved specifically by BSA	p53 transcription and glioblastoma-cell viability outcomes reflect the complete TMZ-WRAP5-p53-BSA co-delivery system	BBB transport, SPARC or gp60 targeting, TMZ-p53 synergy, in vivo efficacy, and persistence of the BSA interface remain untested
Iqbal et al., 2022 BSA-coated PLGA-lapatinib	Direct, comparatively strong: matched coated and uncoated particles plus albumin competition support coating-associated uptake, PK, and biodistribution differences	Tumor inhibition and safety reflect the complete BSA-PLGA-lapatinib formulation	An albumin-sensitive uptake process was supported, but SPARC and gp60 were not identified directly
Carrese et al., 2021 MelaSil_Ag-HSA@DOX	Limited: HSA and DOX binding were characterized, but no matched HSA-free carrier was tested biologically	pH-responsive release and chemo-photothermal cytotoxicity reflect the silica-melanin-silver-HSA-DOX formulation	SPARC-mediated uptake and albumin-driven pH response were proposed but not isolated experimentally

(*continued on next page*)

Table 4 (*continued*)

Study and formulation	Direct albumin/interface evidence	Formulation-level outcome	Proposed or untested albumin-related mechanism
Mahmoud et al., 2024 GNR-BSA and GNS-BSA	Physicochemical coating evidence only; the biological design did not include matched albumin-free nanorods and nanospheres	Viability, uptake, and migration outcomes reflect particle shape, precursor chemistry, and the BSA-containing formulation	An independent albumin contribution to cytotoxicity or migration inhibition remains untested
Zhang et al., 2026 Pt@BSA and Pt@BSA-RM	Boundary evidence: Pt@BSA has an exposed albumin layer, whereas Pt@BSA-RM has an erythrocyte-membrane outer interface	Radiosensitization and in vivo efficacy primarily reflect the complete Pt@BSA-RM plus irradiation regimen	BSA persistence, accessibility, and its independent contribution beneath the membrane remain untested
Bychkova et al., 2022 HSA-IONPs	Direct physicochemical evidence for a more stable free-radical-fixed HSA coating than simple adsorption	CT contrast after local intraarterial administration reflects the complete HSA-IONP system	Systemic tumor targeting, MRI performance, and therapeutic activity were not demonstrated
Caputo et al., 2026 MNP@BSA-cisPt	Coating-associated stability and functionalization were demonstrated, but biological experiments lacked a matched albumin-free drug carrier	MRI relaxivity, spheroid penetration, drug delivery, and barrier-model transport reflect the full formulation	The Caco-2 result does not establish in vivo absorption or receptor-mediated albumin transcytosis
Bychkova et al., 2025 MB/FA-HSA@IONPs	The HSA-coated control isolated a folate-dependent uptake and PDT contribution, not an independent HSA effect	Phototoxicity reflects the folate-HSA-IONP-methylene-blue formulation	Magnetic targeting, MRI, and in vivo tumor delivery remain proposed
Carrese et al., 2023 MelaSil_Ag-HSA@DOX	Bare versus HSA-modified particles supported a coating-associated spheroid-uptake difference	Photoacoustic and chemo-photothermal outcomes reflect the complete hybrid formulation	SPARC involvement and in vivo theranostic performance remain unverified
Ghosh et al., 2025 [188Re]ReOx-HSA	No albumin-free nanoparticle comparator isolated an HSA contribution	SPECT/CT retention and RT/PTT efficacy reflect the intratumorally administered radiolabeled formulation	Systemic targeting, metastatic delivery, and albumin-specific retention remain untested
Nosrati et al., 2020 F-Au-BSA-MTX-CUR	No matched albumin-free nanohybrid was used	Tumor response reflects Fe3O4-Au, BSA, MTX, curcumin, and X-ray irradiation	Albumin-specific circulation prolongation and tumor targeting were not established.
Amatya et al., 2023 BSA-CuNPs	BSA-containing synthesis was characterized, but no albumin-free CuNP control isolated the coating contribution	Photothermal cytotoxicity and preliminary PK reflect the complete BSA-CuNP or ICG-loaded formulation	Tumor imaging and in vivo efficacy were not evaluated
Dongsheng Li et al., 2023 A-PFH/C-MNPs	No albumin-specific biological control	Chemo-photothermal effects reflect the albumin-PFH-cisplatin-magnetite formulation	Imaging, tumor targeting, and in vivo efficacy remain untested
Ayatollahi et al., 2022 ZnO-BSA-DG-FA	No matched albumin-free or ligand-specific final formulation control	Cellular outcomes reflect ZnO, crosslinked BSA, diosgenin, and folate	Albumin-specific targeting and in vivo therapeutic performance remain untested
Li et al., 2021 BLDH/5FU-ABX	Composite albumin-containing surface stabilization was characterized, but no matched albumin-free dual-drug formulation isolated its contribution.	Cellular and animal efficacy reflects LDH, 5FU, Abraxane, and the composite albumin interface	Albumin-specific tumor accumulation, circulation extension, and release control remain untested
Kim et al., 2021 BSA-silver NPs	Protein association and final-particle properties were characterized, but no uncoated silver-NP biological comparator was included	ROS, antiangiogenic, and photothermal effects reflect the complete BSA-silver formulation	Albumin-mediated uptake, circulation, and tumor selectivity remain untested
Zareian Baghdadabad et al., 2026 AgNPs-Alb	A matched AgNP comparator supports coating-associated cellular differences	All evidence is in vitro and the final interface also contains PVP and process-derived components	Albumin-receptor uptake, systemic targeting, and in vivo selectivity were proposed but not demonstrated
Hashemi et al., 2025 MnFe2O4@BSA-quercetin	BSA coating and dialysis were reported, but no albumin-free drug-loaded control isolated its contribution	Release, cytotoxicity, radiosensitization, and healthy-mouse safety reflect the full formulation	Magnetic targeting, tumor-selective release, tumor accumulation, and efficacy remain untested
Olivieri et al., 2024 BSA-coated fluorescent silica NPs	Strong cell-level evidence: matched albumin-charge variants and multiple glycocalyx perturbations linked albumin charge/presentation and heparan sulfate to cellular uptake.	Paclitaxel potency reflects the complete drug-loaded silica-albumin formulation	Relevance under blood flow, systemic exposure, tumor delivery, and in vivo glycocalyx heterogeneity remains untested
Zhao et al., 2021 AuNR@BSA	BSA association, charge reversal, and lower cytotoxicity than the CTAB-coated precursor were demonstrated, although residual CTAB was not quantified	Photothermal tumor suppression reflects AuNR@BSA plus 1064 nm irradiation after intratumoral administration	Systemic albumin-mediated targeting, coating persistence, and an albumin-specific efficacy contribution remain untested

transport should not be interpreted as demonstrated oral absorption or passage across an intact blood-brain barrier.

The available corona evidence further indicates that albumin does not simply prevent protein adsorption. Instead, engineered albumin surfaces may alter the diversity and relative composition of the acquired corona, with potentially selective effects on immune-cell interactions. However, DLS stability does not prove the absence of secondary adsorption, and proteomic associations do not identify causal stealth proteins without functional validation. Moreover, the reviewed corona-proteomic studies did not include validated cancer-patient cohorts, diagnostic-performance metrics, or independent clinical validation. Corona-based cancer detection and the proposed nanoconcentrator workflow must therefore remain clearly identified as hypothesis-generating research directions rather than established diagnostic technologies.

Translation will require direct evidence that the manufactured albumin interface persists, remains conformationally accessible, and contributes causally after biological exposure. Priority studies should independently trace the nanoparticle core and albumin layer, recover circulating particles at multiple time points, quantify albumin retention and exchange, and compare pre-injection, serum-generated, and in vivo acquired interfaces. Matched albumin-free, ligand-free, charge-controlled, and alternative-protein comparators should be combined with standardized corona proteomics, complement and immune-cell assays, pharmacokinetics, organ-level biodistribution, repeated-dose safety, and clinically relevant tumor models. Because BSA is xenogeneic in humans, promising BSA-based systems should also be reformulated and validated with well-characterized pharmaceutical-grade or recombinant HSA. Until these requirements are met, conclusions should remain formulation-specific, proportional to the controls used, and explicit about whether an outcome is albumin-associated, composite-interface-dependent, or attributable to the complete nanoparticle system.

CRediT authorship contribution statement

Gábor Katona: Writing – review & editing, Supervision, Funding

acquisition, Conceptualization. **Maher Darwish:** Writing – review & editing, Writing – original draft. **Ildikó Csóka:** Writing – review & editing, Writing – original draft, Supervision, Funding acquisition, Conceptualization. **Hanan Mohammad:** Writing – review & editing, Writing – original draft, Visualization.

Consent for publication

Not applicable.

Ethics approval and consent to participate

Not applicable.

Declaration of Generative AI and AI-assisted technologies in the writing process

During the preparation and revision of this work, the authors used ChatGPT (OpenAI), scite, Consensus, Elicit, and SciSpace to support supplementary literature discovery, citation-context checking, evidence organization, cross-study comparison, language refinement, and consistency checking. No AI tool was used to make autonomous decisions regarding study eligibility or scientific interpretation. All AI-assisted outputs, references, numerical data, and source-dependent statements were critically reviewed and verified by the authors against the original publications. The authors reviewed and edited the content as needed and take full responsibility for the content of the published article.

Competing interests

The authors declare no competing interests.

Declaration of Competing Interest

The authors declare that they have no known competing financial interests or personal relationships that could have appeared to influence the work reported in this paper.

Acknowledgments

This publication was funded by The University of Szeged Open Access Fund (FundRef, Grant no. 8766). This work was supported by János Bolyai Research Scholarship of the Hungarian Academy of Sciences (G. Katona, BO/00043/25).

Data availability

No data was used for the research described in the article.

References

[1] W. Huang, et al., Research progress and application opportunities of nanoparticle–protein corona complexes, Biomed. Pharmacother. 139 (2021) 111541.
[2] T. Zhao, et al., Engineering the protein corona: strategies, effects, and future directions in nanoparticle therapeutics, Biomed. Pharmacother. 175 (2024) 116627.
[3] M. Mahmoudi, et al., The protein corona from nanomedicine to environmental science, Nat. Rev. Mater. (2023) 1–17.
[4] D. Baimanov, et al., situ analysis of nanoparticle soft corona and dynamic evolution, Nat. Commun. 13 (1) (2022) 5389.
[5] J.R. Shaw, et al., Inflammatory disease progression shapes nanoparticle biomolecular corona-mediated immune activation profiles, Nat. Commun. 16 (1) (2025) 924.
[6] J.S. Suk, et al., PEGylation as a strategy for improving nanoparticle-based drug and gene delivery, Adv. Drug Deliv. Rev. 99 (Pt A) (2016) 28–51.
[7] V. Hornok, Serum albumin nanoparticles: problems and prospects, Polymers 13 (21) (2021).
[8] E.N. Hoogenboezem, C.L. Duvall, Harnessing albumin as a carrier for cancer therapies, Adv. Drug Deliv. Rev. 130 (2018) 73–89.
[9] Q. Peng, et al., Preformed albumin corona, a protective coating for nanoparticles based drug delivery system, Biomaterials 34 (33) (2013) 8521, 30.
[10] H. Mohammad, et al., Functionalized albumin nanoparticles: a multifunctional platform for enhanced brain drug delivery, Mater. Today Bio 35 (2025) 102616.
[11] X. Zhou, et al., Structure-driven design of albumin-based drug delivery systems, Adv. Colloid Interface Sci. 352 (2026) 103840.
[12] A. Baki, et al., Albumin-coated single-core iron oxide nanoparticles for enhanced molecular magnetic imaging (MRI/MPI), Int. J. Mol. Sci. 22 (12) (2021) 6235.
[13] A.V. Bychkova, et al., Albumin-functionalized iron oxide nanoparticles for theranostics: engineering and long-term in situ imaging, Pharmaceutics 14 (12) (2022) 2771.
[14] T. Wu, et al., Bovine serum albumin-gold nanoclusters protein corona stabilized polystyrene nanoparticles as dual-color fluorescent nanoprobes for breast cancer detection, Biosens. Bioelectron. 215 (2022) 114575.
[15] P. Zhang, et al., Nanoprobe based on biominerals in protein corona for dual-modality MR imaging and therapy of tumors, ACS Nano 17 (1) (2023) 184–196.
[16] K. Petrov, et al., Synthesis of magnetic nanoparticles coated with human serum albumin and loaded by doxorubicin, Magnetochemistry 11 (2) (2025) 13.
[17] C. Suwannasing, et al., Albumin-coated copper oxide nanoparticles for radiosensitization of human glioblastoma cells under clinically relevant x-ray irradiation, Nanomaterials 15 (17) (2025) 1376.
[18] A. Caputo, et al., Albumin coating of magnetic nanoparticles for imaging, tracking and delivery through biological barriers, Nanoscale 18 (10) (2026) 5371–5388.
[19] A.V. Bychkova, et al., Folate-modified albumin-functionalized iron oxide nanoparticles for theranostics: engineering and in vitro PDT treatment of breast cancer cell lines, Pharmaceutics 17 (8) (2025) 982.
[20] B. Carrese, et al., Hybrid nanoparticle-assisted chemo-photothermal therapy and photoacoustic imaging in a three-dimensional breast cancer cell model, Int. J. Mol. Sci. 24 (24) (2023) 17374.
[21] S. Ghosh, et al., Protein-functionalized and intrinsically radiolabeled [188Re]ReOx nanoparticles: advancing cancer therapy through concurrent radio-photothermal effects, Eur. J. Nucl. Med. Mol. Imaging 52 (7) (2025) 2628–2644.
[22] H. Nosrati, et al., Improved synergic therapeutic effects of chemoradiation therapy with the aid of a co-drug-loaded nano-radiosensitizer under conventional-dose X-ray irradiation, Biomater. Sci. 8 (15) (2020) 4275–4286.
[23] A.N. Traverso, et al., Two-step preparation of protein-decorated biohybrid quantum dot nanoparticles for cellular uptake, Pharmaceutics 15 (6) (2023) 1651.
[24] S. Bozzer, et al., Stealth-engineered albumin-coated nanoparticles for targeted therapy: effective drug delivery and tumor suppression in xenograft-zebrafish model, Int. J. Nanomed. 19 (2024) 13267–13286.
[25] M. Kumar, et al., Biophysical study of DC electric field induced stable formation of albumin-gold nanoparticles corona and curcumin binding, Spectrochim. Acta Part. A: Mol. Biomol. Spectrosc. 305 (2024) 123469.
[26] P.H. Olivieri Jr, et al., Glycocalyx interactions modulate the cellular uptake of albumin-coated nanoparticles, ACS Appl. Bio Mater. 7 (11) (2024) 7365–7377.
[27] H.M. Leung, et al., Targeted brain tumor imaging by using discrete biopolymer-coated nanodiamonds across the blood–brain barrier, Nanoscale 13 (5) (2021) 3184–3193.
[28] Z. Wu, et al., Pre-coating cRGD-modified bovine serum albumin enhanced the anti-tumor angiogenesis of siVEGF-loaded chitosan-based nanoparticles by manipulating the protein corona composition, Int. J. Biol. Macromol. 267 (2024) 131546.
[29] Y. Arezki, et al., Surface charge influences protein corona, cell uptake and biological effects of carbon dots, Nanoscale 14 (39) (2022) 14695–14710.
[30] K. Saha, et al., Regulation of macrophage recognition through the interplay of nanoparticle surface functionality and protein corona, ACS Nano 10 (4) (2016) 4421, 30.
[31] P.H. Olivieri Jr., et al., Cell-surface glycosaminoglycans regulate the cellular uptake of charged polystyrene nanoparticles, Nanoscale 14 (19) (2022) 7350–7363.
[32] G.M. Mortimer, et al., Cryptic epitopes of albumin determine mononuclear phagocyte system clearance of nanomaterials, ACS Nano 8 (4) (2014) 3357–3366.
[33] G. Li, et al., Effective chemotherapy of lung cancer using bovine serum albumin-coated hydroxyapatite nanoparticles, Med. Sci. Monit.: Int. Med. J. Exp. Clin. Res. 27 (2020) e919716, 1.
[34] T. Goel, et al., Fabrication of a multifunctional CoFe2O4@BSA@Ag nanocomposite: a novel biocompatible nanoplatform for lung cancer therapy and antibacterial applications, ACS Omega 11 (24) (2026) 35019–35033.
[35] T. Tan, et al., Chondroitin sulfate-mediated albumin corona nanoparticles for the treatment of breast cancer, Asian J. Pharm. Sci. 16 (4) (2021) 508–518.
[36] H. Iqbal, et al., pH-responsive albumin-coated biopolymeric nanoparticles with lapatinab for targeted breast cancer therapy, Biomater. Adv. 139 (2022) 213039.
[37] B. Carrese, et al., Controlled release of doxorubicin for targeted chemo-photothermal therapy in breast cancer HS578T cells using albumin modified hybrid nanocarriers, Int. J. Mol. Sci. 22 (20) (2021) 11228.
[38] N.N. Mahmoud, et al., The impact of gold nanoparticles conjugated with albumin on prostate and breast cancer cell lines: insights into cytotoxicity, cellular uptake, migration, and adhesion potential, J. Nanopart. Res. 26 (5) (2024) 101.
[39] Y. Zhang, Y. Liu, D. Zheng, Novel Pt@BSA nanoparticles improve radiotherapeutic outcomes in breast cancer, RSC Med. Chem. 17 (2) (2026) 1187–1199.
[40] S. Zhao, et al., BSA-coated gold nanorods for NIR-II photothermal therapy, Nanoscale Res. Lett. 16 (1) (2021) 170.
[41] N. Hashemi, et al., An integrated computational and experimental study of BSA-coated MnFe2O4 nanoparticles as a drug delivery platform for quercetin, Mater. Adv. 6 (9) (2025) 2925–2941.

[42] H. Yang, et al., Protein corona precoating on redox-responsive chitosan-based nano-carriers for improving the therapeutic effect of nucleic acid drugs, Carbohydr. Polym. 265 (2021) 118071.
[43] S. Palazzolo, et al., A carrier free delivery system of a MAGL inhibitor is effective on ovarian cancer, Eur. J. Pharm. Biopharm. 203 (2024) 114397.
[44] I. Afonso, et al., Design of experiments to tailor the potential of BSA-coated peptide nanocomplexes for temozolomide/p53 gene co-delivery, Pharmaceutics 16 (11) (2024) 1389.
[45] L. Li, et al., Albumin-stabilized layered double hydroxide nanoparticles synergized combination chemotherapy for colorectal cancer treatment, Nanomed. Nanotechnol. Biol. Med. 34 (2021) 102369.
[46] D. Kim, et al., BSA-silver nanoparticles: a potential multimodal therapeutics for conventional and photothermal treatment of skin cancer, Pharmaceutics 13 (4) (2021) 575.
[47] R. Amatya, et al., Albumin-coated copper nanoparticles for photothermal cancer therapy: synthesis and in vitro characterization, Heliyon 9 (7) (2023).
[48] D. Li, et al., The effect of using albumin-perfluorohexane/cisplatin-magnetite nanoparticles produced by hydrothermal method against gastric cancer cells through combination therapy, Arab. J. Chem. (2023).
[49] S. ayatollahi, E. Karimi, M.H. Tabrizi, Fabrication of bovine serum albumin coated ZnO nanoparticles loaded disogenin conjugated folate to improve the anti-cancer potential, J. Polym. Environ. 30 (12) (2022) 5049–5056.
[50] L. Zareian Baghdadabad, et al., Improved anticancer properties of silver nanoparticles by albumin coating in prostate cancer cell lines: an in vitro study, Pharmaceutics 18 (3) (2026) 338.
[51] H. Gharibi, et al., A uniform data processing pipeline enables harmonized nanoparticle protein corona analysis across proteomics core facilities, Nat. Commun. 15 (1) (2024) 342.
[52] A.A. Ashkarran, et al., Standardizing protein corona characterization in nanomedicine: a multicenter study to enhance reproducibility and data homogeneity, Nano Lett. 24 (32) (2024) 9874–9881.
[53] A. Suárez Priede, et al., Deciphering the formation of biogenic nanoparticles and their protein corona: state-of-the-art and analytical challenges, Anal. Bioanal. Chem. 418 (2) (2026) 415–435.
[54] S. Sheibani, et al., Nanoscale characterization of the biomolecular corona by cryo-electron microscopy, cryo-electron tomography, and image simulation, Nat. Commun. 12 (1) (2021) 573.
[55] S.A. Sadeghi, et al., Mass spectrometry-based top-down proteomics for proteoform profiling of protein coronas, Nat. Protoc. 21 (3) (2026) 1092–1125.
[56] Q. Wang, et al., High-throughput plasma/serum proteomics by coupling nanoparticle protein corona-based sample preparation and capillary zone electrophoresis-tandem mass spectrometry, Anal. Methods 17 (31) (2025) 6356–6365.
[57] Y. Niu, et al., In situ measurement of nanoparticle-blood protein adsorption and its heterogeneity with single-nanoparticle resolution via dual fluorescence quantification, Nano Lett. 24 (30) (2024) 9202–9211.
[58] W. He, et al., Next generation nanoparticle protein corona characterization methods, Nanomedicine 20 (8) (2025) 769–771.
[59] A. Saorin, et al., Mass spectrometry proteomics of the nanoparticle corona is highly dependent on sample preparation protocol, Proteomics 26 (5) (2026) 98–111.
[60] M.P. Monopoli, et al., Biomolecular coronas provide the biological identity of nanosized materials, Nat. Nanotechnol. 7 (12) (2012) 779–786.
[61] M. Hadjidemetriou, et al., In vivo biomolecule corona around blood-circulating, clinically used and antibody-targeted lipid bilayer nanoscale vesicles, ACS Nano 9 (8) (2015) 8142–8156.
[62] J. Lazarovits, et al., Supervised learning and mass spectrometry predicts the in vivo fate of nanomaterials, ACS Nano 13 (7) (2019) 8023–8034.
[63] B.X. Huang, H.Y. Kim, C. Dass, Probing three-dimensional structure of bovine serum albumin by chemical cross-linking and mass spectrometry, J. Am. Soc. Mass Spectrom. 15 (8) (2004) 1237, 47.
[64] T. Mogues, et al., IgG antibodies against bovine serum albumin in humans—their prevalence and response to exposure to bovine serum albumin, J. Immunol. Methods 300 (1) (2005) 1–11.
[65] J.T. Andersen, et al., Cross-species binding analyses of mouse and human neonatal fc receptor show dramatic differences in immunoglobulin G and albumin binding, J. Biol. Chem. 285 (7) (2010) 4826–4836.
[66] C. Li, et al., A randomized dose-escalation study on the safety, tolerability, immunogenicity, pharmacokinetics and pharmacodynamics of a novel recombinant human albumin in healthy subjects, Eur. J. Pharm. Sci. 165 (2021) 105923.